

Earth and Space Science

REVIEW ARTICLE

10.1029/2021EA001932

This article is a companion to Iacovino et al. (2021), <https://doi.org/10.1029/2020EA001584>.

Key Points:

- The Python3 tool VESIcal allows extensive comparisons to be drawn between different H_2O - CO_2 solubility models
- Solubility models are not interchangeable—for a single magma composition, different models can predict a wide range of solubility relationships
- The P-T-X calibration range of each solubility model must be critically evaluated before application to a specific volcanic system

Supporting Information:

Supporting Information may be found in the online version of this article.

Correspondence to:

P. E. Wieser,
penny.wieser@gmail.com

Citation:

Wieser, P. E., Iacovino, K., Matthews, S., Moore, G., & Allison, C. M. (2022). VESIcal: 2. A critical approach to volatile solubility modeling using an open-source Python3 engine. *Earth and Space Science*, 9, e2021EA001932. <https://doi.org/10.1029/2021EA001932>

Received 25 JUL 2021

Accepted 22 NOV 2021

Author Contributions:

Conceptualization: P. E. Wieser, K. Iacovino, S. Matthews, G. Moore

Data curation: P. E. Wieser, K. Iacovino, S. Matthews

Formal analysis: P. E. Wieser

© 2022 The Authors. *Earth and Space Science* published by Wiley Periodicals LLC on behalf of American Geophysical Union.

This is an open access article under the terms of the [Creative Commons Attribution License](#), which permits use, distribution and reproduction in any medium, provided the original work is properly cited.

VESIcal: 2. A Critical Approach to Volatile Solubility Modeling Using an Open-Source Python3 Engine

P. E. Wieser^{1,2} , K. Iacovino³ , S. Matthews⁴, G. Moore³ , and C. M. Allison⁵

¹Department of Earth Sciences, University of Cambridge, Cambridge, UK, ²College of Earth, Ocean and Atmospheric Sciences, Oregon State University, Corvallis, OR, USA, ³Jacobs, NASA Johnson Space Center, Houston, TX, USA,

⁴Department of Earth and Planetary Sciences, Johns Hopkins University, Baltimore, MD, USA, ⁵Department of Geosciences, Baylor University, Waco, TX, USA

Abstract Accurate models of H_2O and CO_2 solubility in silicate melts are vital for understanding volcanic plumbing systems. These models are used to estimate the depths of magma storage regions from melt inclusion volatile contents, investigate the role of volatile exsolution as a driver of volcanic eruptions, and track the degassing path followed by a magma ascending to the surface. However, despite the large increase in the number of experimental constraints over the last two decades, many recent studies still utilize an earlier generation of models which were calibrated on experimental datasets with restricted compositional ranges. This may be because many of the available tools for more recent models require large numbers of input parameters to be hand-typed (e.g., temperature, concentrations of H_2O , CO_2 , and 8–14 oxides), making them difficult to implement on large datasets. Here, we use a new open-source Python3 tool, VESIcal, to critically evaluate the behaviors and sensitivities of different solubility models for a range of melt compositions. Using literature datasets of andesitic-dacitic experimental products and melt inclusions as case studies, we illustrate the importance of evaluating the calibration dataset of each model. Finally, we highlight the limitations of particular data presentation methods, such as isobar diagrams, and provide suggestions for alternatives, and best practices regarding the presentation and archiving of data. This review will aid the selection of the most applicable solubility model for different melt compositions, and identifies areas where additional experimental constraints on volatile solubility are required.

Plain Language Summary Being able to accurately model the solubility of H_2O and CO_2 in magmas is very important for understanding a wide variety of volcanic processes, such as the depths at which magma is stored in the crust, the driving force behind volcanic eruptions, and the release of volatile elements into the atmosphere. However, there has been no easy way for volcanologists to perform calculations on large datasets, or to compare different models. This review uses a new, open-source tool called VESIcal written in the popular programming language Python3. This allows us to compare different models for a wide variety of melt compositions, temperatures, and pressures, helping researchers to identify the most suitable model for their study. We also suggest areas where further experimental constraints are required. Finally, we highlight the limitations of particular data presentation methods, such as isobar diagrams, provide suggestions for alternative plots, and best practices regarding the presentation and archiving of data.

1. Introduction

The most abundant volatile components found in terrestrial magmatic systems are H_2O and CO_2 . It has been known for nearly a century (Bowen, 1928; Tuttle & Bowen, 1958) that these volatile species have profound effects on the chemical and material properties of magmas (e.g., phase equilibria, melting temperatures, magma viscosity, and density; Burnham, 1979; Burnham & Davis, 1974; Hess & Dingwell, 1996; Husen et al., 2016; Ochs & Lange, 1999), so significantly affect their geochemical and dynamical behavior (e.g., eruption and degassing style, erupted volume; Huppert & Woods, 2002; La Spina et al., 2021; Papale et al., 1999). Thus, it is vital to be able to predict how H_2O and CO_2 solubilities change as a function of intensive variables such as pressure, temperature, melt, and fluid composition in order to understand plutonic and volcanic systems.

The solubility of a volatile species is defined at a given pressure and temperature as the maximum concentration that can be dissolved within a silicate melt of a specified composition. Ignoring disequilibrium effects, if the volatile content of the system exceeds this solubility limit, a separate fluid/vapor phase will exsolve from the magma.

Funding acquisition: K. Iacovino, G. Moore
Investigation: P. E. Wieser, K. Iacovino, S. Matthews
Methodology: P. E. Wieser, K. Iacovino, S. Matthews
Project Administration: P. E. Wieser, K. Iacovino, S. Matthews, G. Moore, C. M. Allison
Resources: P. E. Wieser, K. Iacovino, S. Matthews
Software: P. E. Wieser, K. Iacovino, S. Matthews
Validation: P. E. Wieser, K. Iacovino, S. Matthews, G. Moore
Visualization: P. E. Wieser
Writing – original draft: P. E. Wieser, K. Iacovino
Writing – review & editing: P. E. Wieser, K. Iacovino, S. Matthews, G. Moore, C. M. Allison

In this review, we favor the term fluid because of the supercritical nature of exsolved volatile phases at magmatic temperatures. In general terms, a magma is described as volatile undersaturated when there is no fluid phase, and volatile saturated once a fluid phase is present (also referred to as vapor undersaturated/saturated, or fluid undersaturated/saturated). In detail, different volatile species do not act as independent entities, but influence one another. For this reason, a magma may exsolve a mixed $\text{CO}_2\text{-H}_2\text{O}$ fluid even if the dissolved concentrations of H_2O and CO_2 do not exceed the pure solubility limit of each species.

Despite the obvious importance of accurate volatile solubility modeling, very few studies of volcanic systems have evaluated results using several different solubility models to determine possible sources of systematic error, and assess the suitability of each model for the conditions of interest (e.g., temperature, pressure, and melt composition). This lack of intercomparison likely results from the fact that it was extremely time consuming to perform the large numbers of calculations necessary for thorough comparisons using available tools. For example, many solubility models were released as stand-alone Excel spreadsheets (e.g., Allison et al., 2019; Moore et al., 1998; Newman & Lowenstern, 2002) or web apps (e.g., Ghiorso & Gualda, 2015; Iacono-Marziano et al., 2012), where saturation pressures, dissolved volatile contents, degassing paths, and isobars can only be calculated for one sample and set of conditions at a time. The more recent models which include several terms accounting for the effect of melt composition on volatile solubility require users to hand-type a large number of input parameters. For example, to calculate a saturation pressure in MagmaSat (Ghiorso & Gualda, 2015), users must hand-type 9–14 oxide concentrations in addition to entering H_2O and CO_2 concentrations, and a melt temperature. Similarly, the web app of Iacono-Marziano et al. (2012) requires users to input 8 major element oxide concentrations. Calculating isobars using these web apps is a particularly daunting task, as users must evaluate dissolved volatile contents at multiple fluid compositions, and then use curve fitting to produce a smooth isobar to display on plots. Other models were released with no calculator at all, requiring each user to correctly interpret and combine the relevant equations in the manuscript (Dixon, 1997; Shishkina et al., 2014).

Here, we take advantage of the recent release of Volatile Equilibria and Saturation Identification calculator (VESIcal; Iacovino et al., 2021), an open-source tool written in Python3. VESIcal contains functions to calculate saturation pressures, dissolved volatile contents, isobars, and degassing paths automatically for seven different models. Calculations can be performed based on melt compositions provided in an Excel spreadsheet, and users can take full advantage of Python's extensive flexibility to perform large numbers of calculations automatically (e.g., creating for loops to perform calculations across a range of pressures, temperatures, and fluid compositions). To our knowledge, the only other model with similar functionality to VESIcal is the Linux program Solwcad supplied by Papale et al. (2006), which performs calculations automatically on a user-supplied.txt file containing melt compositions, pressures, and temperatures (<http://www.pi.ingv.it/progetti/eurovolc/>). Solwcad was used alongside VESIcal in this review, through the Windows Subsystem for Linux (WSL2).

The overall aim of this review is to summarize the formulation, strengths, and weaknesses of popular solubility models to inform users who wish to model volatile solubility in silicate melts, whether that be the calculation of melt inclusion saturation pressures, degassing paths, incorporating volatile exsolution in physical model of magma chambers (e.g., Huber et al., 2019), or calculating the dissolved volatile contents of fluid-saturated experimental products where the pressure, temperature and exsolved fluid composition are known (e.g., Waters & Lange, 2015). Specifically, we demonstrate in a number of ways how users investigating a specific subset of compositional space (e.g., melt inclusions from a single volcano) can assess the similarities and differences between models, and evaluate these findings in the context of the calibration dataset and formulation of each model. We start by briefly summarizing the major results from volatile solubility experiments over the last century (Section 2), before describing nine of the most popular solubility models (Section 3). We then compare the solubility of pure H_2O , mixed $\text{H}_2\text{O-}\text{CO}_2$, and pure CO_2 predicted by different models for representative mafic and silicic compositions (Section 4). We also explore the sensitivity of these models to parameters such as temperature and redox state, which are often poorly constrained in igneous systems (Section 5). Finally, we evaluate the suitability of these models for intermediate melt compositions, where experimental constraints are sparse relative to basaltic and rhyolitic melts (Section 6). We conclude by discussing best practices for presenting and archiving data related to volatile components in igneous systems (Section 7). Overall, these discussions demonstrate that there are large differences between model outputs, even in relatively “normal” melt compositions, so the choice of solubility model is a critical part of any study investigating magmatic volatiles (and needs to be justified in all cases). This manuscript will act as a guide to help users assess the suitability of each model for their specific application

(supplemented by the Jupyter Notebooks provided in the Supporting Information, which can be easily adapted to evaluate melt compositions and conditions relevant to a specific study).

2. Major Findings From Experimental Studies Investigating Volatile Solubility in Magmas

One of the earliest volatile studies was that of Goranson (1931), who investigated the effect of pressure on the solubility of water in granitic melts. The classic treatise of Tuttle and Bowen (1958) investigated the impact of H_2O on mineral phase equilibrium. This study led to a wider recognition of the importance of volatiles, and motivated the development of experimental and analytical approaches to determining volatile solubilities as a function of pressure, temperature, and melt composition. Hamilton et al. (1964) was one of the first to compare H_2O solubilities for differing melt compositions (basalt and andesite), while also investigating the effect of dissolved H_2O and oxidation state on the magmatic phase equilibria. These studies were followed by the fundamental experimental measurements of the Burnham group on the dissolution of H_2O in albite melts (e.g., Burnham & Davis, 1971, 1974).

Furthermore, investigation of volatile solubility over the next four decades in natural samples and experimental products was aided significantly by analytical developments, allowing volatile contents in quenched glasses to be measured by techniques, such as Fourier transform infra-red spectroscopy (FTIR; e.g., Fine & Stolper, 1986; Silver et al., 1990; Stolper, 1982) and secondary ion mass spectrometry (SIMS; Hauri, 2002; Hervig & Williams, 1988). In particular, the high spatial resolution of FTIR and SIMS (a few tens of micrometers) meant that volatile concentrations could be measured within quenched pockets of melt trapped within crystals (termed melt inclusions). Unlike subaerially erupted lavas which have degassed almost all their H_2O and CO_2 following their ascent to shallow pressures, melt inclusions remain pressurized during ascent as they are trapped in relatively incompressible crystals, so retain high volatile contents (Anderson, 1974; Roedder, 1979).

Melt inclusion analyses have greatly advanced our understanding of the behavior of volatiles in volcanic systems (Hauri et al., 2002; Lowenstern, 2003; Métrich & Wallace, 2008; Roggensack, 2001; Sides et al., 2014a; Wallace et al., 1995). For example, melt inclusions provide insights into pre-eruptive volatile contents (e.g., Hervig et al., 1989; Saal et al., 2002), and links between melt volatile contents and eruption styles (Lucic et al., 2016; Wieser et al., 2022). The strong pressure-dependence on volatile solubility means that H_2O and CO_2 contents within melt inclusions trapped from a volatile-saturated magma can be used to determine the pressure at which the inclusion was sealed off (termed the saturation pressure or entrapment pressure). In turn, the distribution of saturation pressures in a suite of melt inclusions can reveal the locations of the main regions of magma storage in a volcanic system. This explosion of new information from melt inclusions greatly increased the demand for flexible and accurate solubilities models that could be applied to a broad range of pressures, temperatures, and melt/fluid compositions (Ghiorso & Gualda, 2015; Moore, 2008).

It has become increasingly apparent from solubility experiments that the solubility of H_2O is relatively insensitive to melt composition (e.g., Moore & Carmichael, 1998; Shishkina et al., 2010), while CO_2 solubility is highly sensitive to melt composition, particularly in mafic melts where the carbonate ion is the dominant species (Allison et al., 2019; Brooker et al., 2001a; Dixon, 1997; Iacono-Marziano et al., 2012; Shishkina et al., 2010, 2014). This has led to a great diversity in the way that various models treat the dependence of CO_2 solubility on melt composition. In general, models have become more complex with time as the region of compositional space spanned by solubility experiments has increased to include more alkaline melts. The individual role and relative importance of each cation species in the melt on carbonate ion solubility is still associated with a large degree of uncertainty (Allison et al., 2019), accounting for the larger discrepancies between different model predictions for CO_2 versus H_2O .

Experimental work has also highlighted the complexities of mixing between H_2O and CO_2 in igneous systems. In the simplest case, the addition of one component in a melt-fluid system decreases the activity, and therefore the solubility of the other component in the melt (Lowenstern, 2001). This behavior is referred to as Henrian/ideal behavior, described by Henry's Law. Henry's Law states that the amount of a volatile dissolved in a liquid is proportional to its partial pressure in the gas phase in equilibrium with that liquid. Neglecting the possible entropic effects of speciation, the addition of H_2O to the fluid/gas phase acts to lower the partial pressure of CO_2 ,

and therefore lowers the solubility of CO_2 in the liquid. Similarly, addition of CO_2 to the fluid/gas phase causes the solubility of H_2O in the melt to decrease.

Experimental studies have shown that Henry's law is generally obeyed at low pressures (<1 kbar) in basaltic (Dixon et al., 1995) and rhyolitic melts (Blank et al., 1993). However, at higher pressures, some experimental observations have shown that the mixing behavior of CO_2 and H_2O becomes strongly non-Henrian (Papale, 1999). For example, Eggler (1973), Mysen et al. (1976), and Mysen (1976) show that the solubility of CO_2 in albitic melts increases with the addition of H_2O at higher pressures. This has been attributed to the fact that the addition of small amounts of water as OH^- species decreases melt polymerization, and therefore enhances the solubility of CO_2 relative to an entirely anhydrous melt. After a certain amount of H_2O is added, solubility decreases once more because the addition of H_2O to the fluid phase causes the fugacity of CO_2 to decrease (Dingwell, 1986; King & Holloway, 2002; Mysen, 1976). More recently, this behavior has been demonstrated for dacitic and rhyolitic melts by Behrens et al. (2004) and Liu et al. (2005).

The non-ideal behavior of H_2O and CO_2 in basaltic and andesitic melts at higher pressures is less well constrained. King and Holloway (2002) show that at 1 kbar, andesitic melts ($\text{SiO}_2 = 58.4$ wt%) exhibit a sharp increase in the solubility of CO_3^{2-} species with increasing melt H_2O contents between 0 and 3.39 wt%. In contrast, Jakobsson (1997) show that the solubility of CO_2 in an icelanditic melt (54.6 wt% SiO_2) at 10 kbar is essentially constant as melt water contents vary between ~1 and 9 wt%. Similar behavior to that observed by Jakobsson (1997) was noted for andesitic magmas (57.4 wt% SiO_2) at 5 kbar by Botcharnikov et al. (2006), who suggest that differences between H_2O - CO_2 mixing in their experiments and those of King and Holloway (2002) may result from differences in oxygen fugacity ($\text{Fe}^{3+}/\text{Fe}_\text{T} = 0.2\text{--}0.6$ vs. $\text{Fe}^{3+}/\text{Fe}_\text{T} = 0.09\text{--}0.2$). As we discuss in Section 4.1, the influence of oxygen fugacity on volatile solubility is still poorly constrained. Recent basaltic H_2O - CO_2 experiments generally show a relatively flat plateau for CO_2 solubility with increasing melt H_2O contents between ~0 and 4 wt% (Iacono-Marziano et al., 2012; Shishkina et al., 2010, 2014), although relatively large error bars on analyses of CO_2 in experimental products make it difficult to determine whether this plateau is truly flat, or shows a slight positive or negative gradient at low H_2O contents (see Figure 7a of Iacono-Marziano et al., 2012). The effect of H_2O - CO_2 mixing in the nine solubility models evaluated here is discussed further in Sections 4.2.2 and 4.3.2.

3. Models Discussed in This Review

In this review, we focus on the seven models implemented in VESIcal (Iacovino et al., 2021):

1. The simplified parameterization of the Dixon (1997) model for H_2O and CO_2 , which was implemented in the popular Excel tool VolatileCalc (Newman & Lowenstern, 2002), hereafter VolatileCalc-Basalt.
2. The H_2O model of Moore et al. (1998), hereafter M-1998.
3. The H_2O and CO_2 models of Liu et al. (2005), hereafter L-2005.
4. The H_2O and CO_2 models of Iacono-Marziano et al. (2012), hereafter IM-2012.
5. The H_2O and CO_2 models of Shishkina et al. (2014), hereafter S-2014.
6. The combined H_2O and CO_2 model of Ghiorso and Gualda (2015), hereafter MagmaSat.
7. The CO_2 models of Allison et al. (2019), hereafter A-2019.

We also consider the two additional models, reflecting both their popularity and relative ease of calculation using previously published tools:

8. The combined H_2O and CO_2 model of Papale et al. (2006), hereafter P-2006, accessed using the Linux program solwcad.
9. The Rhyolite functions in the VolatileCalc spreadsheet, hereafter VolatileCalc-Rhyolite.

We do not consider the models of Duan (2014), Eguchi and Dasgupta (2018), or Burgisser et al. (2015) because no tool exists to automate the necessary calculations. We also do not discuss models with more limited pressure (P), temperature (T), or compositional (X) ranges.

A summary of the P , T , and X range covered by the calibration dataset of each of the nine models evaluated, as well as available tools to perform calculations, is provided in Figure 1. The calibration dataset of each model is shown on a total alkali-silica diagram in Figure 2. Detailed descriptions of each model are provided below.

3.1. VolatileCalc-Basalt: A Simplification of Dixon (1997)

The Dixon (1997) model calculates the solubility of H_2O and CO_2 in basaltic silicate melts, combining thermodynamic expressions as a function of pressure and temperature described in Dixon et al. (1995) with empirical parameters accounting for the effect of melt composition in terms of melt SiO_2 content from Dixon (1997). The thermodynamic expressions are originally from Fine and Stolper (1986) for carbon and Silver and Stolper (1989) for water. The Dixon (1997) model considers the solubility of the carbonate ion (CO_3^{2-}) for CO_2 , and both molecular water ($\text{H}_2\text{O}_{\text{mol}}$) and hydroxyl groups (OH^-) for H_2O .

The solubility of molecular H_2O is calculated using an adapted version of Equation 3 of Dixon et al. (1995). In the original 1995 equation the $X_{\text{H}_2\text{O}_{\text{mol}}}^m (P_0, T_0)$ term representing the mole fraction of molecular H_2O in equilibrium with fluid with a fugacity of water specified by $f_{\text{H}_2\text{O}}(P_0, T_0)$ at 1473.15 K and 1 bar was fixed at 3.28×10^{-5} . To account for the effect of melt composition on H_2O solubility, Dixon (1997) parameterize this term as a function of melt SiO_2 content:

$$X_{\text{H}_2\text{O}_{\text{mol}}}^m (P_0, T_0) = 3.04 \times 10^{-5} + 1.29 \times 10^{-6} [\text{SiO}_2]^{\text{wt}\%} \quad (1)$$

This relationship was derived from experimental observations of Cocheo and Holloway (1993), and predicts that there is a $\sim 30\%$ increase in the solubility of H_2O with increasing SiO_2 between nephelinite (~ 40 wt% SiO_2) and tholeiite (~ 49 wt% SiO_2) melt compositions. The concentration of OH^- is then calculated as a function of the mole fraction of molecular H_2O in the melt using the solution model of Silver and Stolper (1989) (see Equation 4 of Dixon, 1997). Interestingly, this is the only model discussed here which considers more than one species for dissolved H_2O in the melt.

For CO_2 solubility, Dixon (1997) adapted the model of Dixon et al. (1995) to account for the effect of melt composition, based on observations from experiments that CO_2 solubility increases from tholeiitic (49 wt% SiO_2) to basanitic (46 wt% SiO_2) to leucitic (44.1 wt% SiO_2) melts at 1200°C, 1 kbar. A linear regression with CO_2 solubility was achieved using a composition parameter (Π) expressed in terms of the cation fractions, X_i (Dixon, 1997):

$$\Pi = -6.50(X_{\text{Si}^{4+}} + X_{\text{Al}^{3+}}) + 20.17(X_{\text{Ca}^{2+}} + 0.8X_{\text{K}^+} + 0.7X_{\text{Na}^+} + 0.4X_{\text{Mg}^{2+}} + 0.4X_{\text{Fe}^{2+}}) \quad (2)$$

However, based on the strong correlation between Π and SiO_2 in a suite of lavas from the North Arch Volcanic Field, Dixon (1997) express the $X_{\text{CO}_3^{2-}}^m (P_0, T_0)$ term from Equation 6 of Dixon et al. (1995) solely as a function of melt SiO_2 content:

$$X_{\text{CO}_3^{2-}}^m (P_0, T_0) = 8.70 \times 10^{-6} - 1.70 \times 10^{-7} [\text{SiO}_2]^{\text{wt}\%} \quad (3)$$

where $X_{\text{CO}_3^{2-}}^m (P_0, T_0)$ is the mole fraction of carbonate in equilibrium with fluid with a fugacity of carbon dioxide specified by $f_{\text{CO}_2}(P_0, T_0)$ at 1473.15 K and 1 bar. Fugacities are calculated using the Redlich-Kwong equation of state (Holloway, 1977), with the correction of Flowers (1979).

This simplified expression was designed to aid the investigations of volatile solubility in the suite of lavas from the North Arch, where it effectively captures the observed 5 \times decrease in CO_2 solubility from 40 to 49 wt% SiO_2 . However, this simplified parameterization became very widely used in a wide variety of tectonic settings following its implementation in the Excel-based tool VolatileCalc (Newman & Lowenstern, 2002). Here, we refer to this model as VolatileCalc-Basalt, to differentiate it from the full Π parameterization of Dixon (1997).

The advantage of the Π - SiO_2 simplification is that users only have to input the concentration of one oxide component (melt SiO_2) in addition to melt temperature and melt volatile contents to calculate saturation pressures or degassing paths. The limited number of inputs required by this model meant that users can

Publication	Volatile	Speciation	P (bar)	T (°C)	Notes
Moore et al., 1998	H ₂ O	N/A	0–3000 ¹	700–1200 ¹	
Newman and Lowenstern (2002) VolatileCalc–Basalt	H ₂ O CO ₂	H ₂ O as OH- and H ₂ O _{mol} CO ₂ as CO ₃ ²⁻	0–5000 ¹ 0–2000 ² 0–1000 ³	600–1500 ¹ 1200 ⁴	¹ Author-suggested calibration range. The calibration dataset spans 190 to 6067 bar, and 800–1200 °C. ² Calibration range suggested by Le Neve et al. (2011). ³ Calibration range suggested by Iacono–Marziano et al. (2012). ⁴ Calibration temperature of Dixon (1997). *if normalized (not recommended), different proportions of FeO and Fe ₂ O ₃ will slightly change the normalized SiO ₂ content
Newman and Lowenstern (2002) VolatileCalc–Rhyolite	H ₂ O CO ₂	H ₂ O as OH- and H ₂ O _{mol}	0–5000 ¹	600–1500 ¹	¹ Calibration range warning implemented in VolatileCalc (Newman and Lowenstern, 2002).
Liu et al. 2005	H ₂ O CO ₂	N/A	0–5000 ¹	700–1200 ¹	¹ Author-suggested calibration range for the mixed fluid model. The calibration dataset covers 750–5510 bar and 800–1150 °C for the carbon model, and 1–5000 bar and 700–1200 °C for the water model
Papale et al. (2006)	H ₂ O CO ₂	N/A	0–10,000 ¹	~630–1630 ¹	¹ Intersection of H ₂ O–CO ₂ fields on Fig. 10 of Papale (1999)
Iacono–Marziano et al., 2012	H ₂ O CO ₂	N/A	100–10000 (mostly <5000) ¹	1100–1400 (preferably 1200–1300) ²	¹ Range of calibration dataset, as authors do not state a preferred range. We note that the vast majority of experiments were conducted at <5000 bar. ² Authors state that most experiments were conducted between 1200–1300 °C (whole range 1100–1400 °C).
Shishkina et al. 2014	H ₂ O ¹ CO ₂ ¹	N/A	0–5000 ² 500–5000 ²	1050–1400 (preferably 1150–1250) ^{2,3} 1200–1250 ^{2,3}	¹ Although their empirical expressions are for pure fluids, they were mostly calibrated on mixed CO ₂ –H ₂ O experiments. ² Author-suggested range ³ Note, this model contains no temperature term.
Magmasat (Ghiurso and Gualda, 2015)	H ₂ O CO ₂ H ₂ O–CO ₂	H ₂ O: as OH- CO ₂ ; as CaCO ₃ and CO ₃ ²⁻ _{mol}	0–20,000 ¹ 0–30,000 ¹ 0–10,000 ¹	550–1420 ¹ 1139–1400 ¹ 800–1400 ¹	¹ Ranges extracted from Fig. 2d of Ghiurso and Gualda, 2015
Allison et al., 2019	CO ₂ ¹	N/A	0–7000 ²	1200 ³ (~1000–1400)	¹ Although this model is for pure CO ₂ , it was calibrated on mixed CO ₂ –H ₂ O experiments. ² Author-suggested range. The calibration dataset spans: (SFVF: 4133–6141 bar, Sunset Crater: 4071–6098 bar, Erebus: 4078–6175 bar, Vesuvius: 269–6175 bar, Etna: 485–6199 bar, Stromboli: 524–6080 bar). ³ Note, all calculations and experiments were performed at 1200 °C. Authors suggest applicable between 1000–1400 °C.

Continued over page...

Figure 1. Summary of the calibration range of each model, as well as available tools to perform calculations. Models are colored using the same palette as comparison figures.

Publication	Compositional range	Formulation	Redox sensitive?	Available Tools
Moore et al., 1998	Broad compositional range: subalkaline basalts to rhyolites, alkaline trachybasalts–andesites, foidites, phonolites	Thermodynamic basis, empirical effect of melt composition	No (input FeO_{T})	<ul style="list-style-type: none"> Macro-enabled Excel spreadsheet supplied by authors Python3 code (VEStcal; Iacovino et al. 2021)
Newman and Lowenstern (2002) VolatileCalc–Basalt	Alkali basalts: 40–49 wt% SiO_2	Thermodynamic basis, empirical effect of melt composition	No (input SiO_2 only)*	<ul style="list-style-type: none"> Macro-enabled Excel spreadsheet (VolatileCalc; Newman and Lowenstern, 2002) Python2 code (Rasmussen et al. 2020) Python3 code and web application (VEStcal; Iacovino et al. 2021)
Newman and Lowenstern (2002) VolatileCalc–Rhyolite	Rhyolites	Thermodynamic basis, no compositional term	No	<ul style="list-style-type: none"> Macro-enabled Excel spreadsheet (VolatileCalc; Newman and Lowenstern, 2002)
Liu et al. 2005	Haplogranites and rhyolites	Empirical basis, no compositional term	No	<ul style="list-style-type: none"> Python3 code (VEStcal; Iacovino et al. 2021)
Papale et al. (2006)	Broad compositional range (SiO_2 =37–85, $\text{Na}_2\text{O}+\text{K}_2\text{O}$ =0–20) for H_2O , more limited for CO_2 and $\text{CO}_2\text{--H}_2\text{O}$ liquids. Poor coverage of intermediate compositions (SiO_2 =55–75 wt%).	Fully thermodynamic (formulation + effect of melt composition)	Yes (input FeO and Fe_{2O_3})	<ul style="list-style-type: none"> Web application, Linux application, and Fortran source code (SOLWCAD, hosted at http://www.pi.ingv.it/progetti/eurovolc/)
Iacono–Marziano et al., 2012	Predominantly mafic compositions: subalkaline and alkaline basalts–andesites	Thermodynamic basis, empirical effect of melt composition	No (input FeO_{T})	<ul style="list-style-type: none"> Web application (http://calcul-isto.cnrs-orleans.fr/apps/h2o-co2-systems/) Python3 code (VEStcal; Iacovino et al. 2021)
Shishkina et al. 2014	H_2O : Mafic and intermediate compositions: Subalkaline basalts–basaltic andesites, alkali basanites–phonolites, SiO_2 <65 wt%. CO_2 : Predominantly mafic compositions: subalkaline basalts, alkaline basanites, trachybasalts	Fully empirical (formulation+ effect of melt composition)	Only for CO_2 (π^* uses Fe^{2+}), Calibrated with $\text{Fe}=\text{Fe}^{2+}$	<ul style="list-style-type: none"> Python3 code (VEStcal; Iacovino et al. 2021), which uses $\text{Fe}=\text{Fe}^{2+}$
Magmasat (Ghiurso and Gualda, 2015)	Very broad compositional range of natural silicate melt compositions: subalkaline picropelites–rhyolites, wide variety of mafic–silicic alkaline compositions	Fully thermodynamic (formulation + effect of melt composition)	Yes (input FeO and Fe_{2O_3})	<ul style="list-style-type: none"> Web application (http://melts.of-research.org/CORBA_CTSserver/CG-H2O-CO2.html) Mac App Store (MagmaSat) Python3 code (VEStcal; Iacovino et al. 2021)
Allison et al., 2019	Alkali-rich mafic magmas from 6 volcanic fields (San Francisco Volcanic Field, Sunset Crater, Erebos, Vesuvius, Etna, Stromboli). Separate model coefficients for each composition.	Thermodynamic basis, separate parameters for each of 6 melt compositions.	No	<ul style="list-style-type: none"> Excel spreadsheet supplied by authors Python3 code (VEStcal; Iacovino et al. 2021)

Figure 1. (Continued)

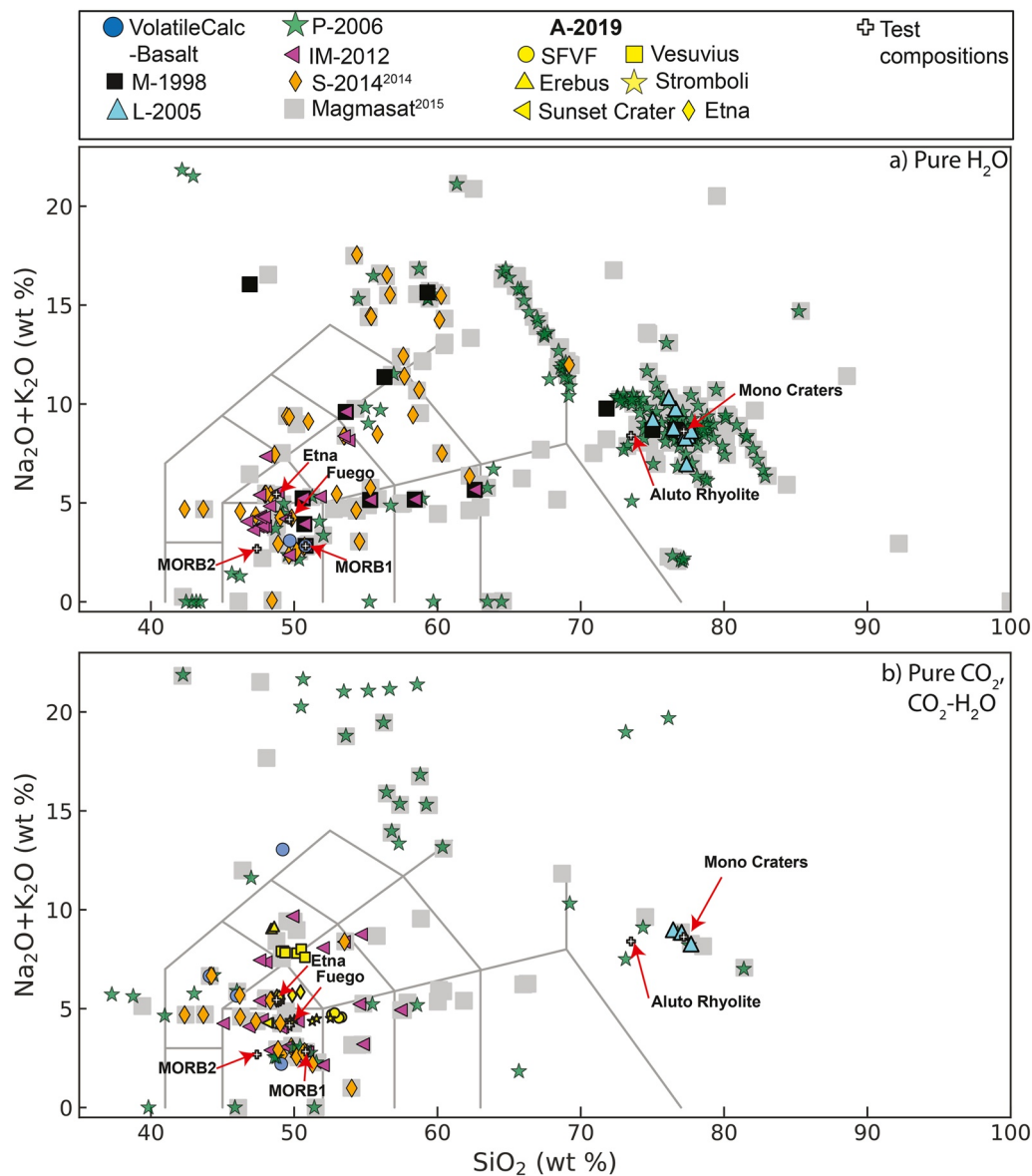


Figure 2. Total alkalis ($\text{Na}_2\text{O} + \text{K}_2\text{O}$) versus SiO_2 (TAS) diagram showing the composition of melts in the calibration dataset of each model for (a) pure H_2O and (b) pure CO_2 and mixed $\text{CO}_2\text{-H}_2\text{O}$. Pure CO_2 and $\text{CO}_2\text{-H}_2\text{O}$ experiments are combined because pure CO_2 experiments are often contaminated by variable amounts of H_2O due to exposure with the Earth's atmosphere, and the high mobility of H^+ through experimental apparatus (Mangan et al., 2021). As dissolved H_2O contents in glasses from pure CO_2 experiments are rarely reported, it is nontrivial to distinguish these from a mixed $\text{H}_2\text{O-}\text{CO}_2$ experiment. For P-2006 and MagmaSat, points were extracted from the TAS diagrams shown in these papers using Web Plot Digitizer (Rohatgi, 2017). For the other models, the calibration dataset is provided in the supplementary information of Iacovino et al. (2021). TAS plot drawn using Python code from Stevenson (2015).

calculate saturation pressures for large numbers of melt inclusions relatively quickly compared to more recent models, such as Iacono-Marziano et al. (2012) and MagmaSat (which require users to input 8–14 oxide concentrations).

However, extreme care must be taken when using this simplified model to calculate CO_2 solubility. First, the North Arch lavas span SiO_2 contents of only 40–49 wt%. Because of the rapid drop in Π with increasing SiO_2 , extrapolation beyond 51.2 wt% SiO_2 yields a negative value for $X_{\text{CO}_3^{2-}}^m (P_0, T_0)$, corresponding to a negative amount of dissolved CO_2 . To avoid this issue, VolatileCalc-Basalt returns an error, and will not perform the

Table 1
Representative Compositions Used for Comparisons

Name	MORB1	MORB2	Etna	Fuego	Mono craters	Aluto pumice
SiO ₂	50.8	47.4	48.77	49.67	77.19	73.51
TiO ₂	1.84	1.01	1.79	1.17	0.06	0.23
Al ₂ O ₃	13.7	17.64	16.98	16.50	12.8	9.18
Fe ₂ O ₃	2.1	0.89	2.51	1.65	0.26	1.41
FeO	10.5	7.18	6.44	8.43	0.71	3.81
MnO	0	0	0.18	0.19	0	0.25
MgO	6.67	7.63	6.33	4.38	0.03	0
CaO	11.5	12.44	11.26	7.90	0.53	0.2
Na ₂ O	2.68	2.65	3.65	3.37	3.98	4.18
K ₂ O	0.15	0.03	1.79	0.79	4.65	4.22
P ₂ O ₅	0.19	0.08	0.53	0.22	0	0

Note. MORB1 is a Mid-Oceanic Ridge Basalt tholeiite from Dixon et al. (1995). MORB2 is the MORB composition given in Table 3 of Ghiorso and Gualda (2015), originally from Allan et al. (1989). Etna is sample ET-8 from the supplementary information of Allison et al. (2019). Fuego is the composition of a melt inclusion from Lloyd et al. (2013). Mono Craters is from Table 1 of Liu et al. (2005). Aluto rhyolite is the composition of a quartz-hosted melt inclusion from the East African Rift (MI70 from sample MER055A; Iddon & Edmonds, 2020).

calculation if users enter a SiO₂ content >49 wt%. Most studies extrapolate beyond this by simply entering SiO₂ = 49 wt% into VolatileCalc-Basalt if their melts have higher silica contents (e.g., Sides et al., 2014a, 2014b; Tucker et al., 2019), and this approach is implemented in VESical for consistency. Newman and Lowenstern (2002) suggest that this extrapolation will be “generally applicable for other basaltic rocks with <52 wt% SiO₂.” However, if a large proportion of a sample suite has SiO₂ contents with >49 wt% SiO₂, the simplified Π -SiO₂ parameterization treats all melts as if they have the same composition, neglecting variations in solubility that may exist within that suite (see Wieser et al., 2021). Additionally, even if samples have SiO₂ contents between 40 and 49 wt%, this simplification can yield spurious results for melts which do not follow the same trend in Π -SiO₂ space to the North Arch lavas (see Section 4.2.3). Thus, we suggest that any users wishing to apply VolatileCalc-Basalt to their system first check whether their melt compositions lie close to the trend defined by the North Arch lavas using the Jupyter Notebook provided in the Supporting Information of Iacovino et al. (2021).

It is also worth noting that, because VolatileCalc-Basalt parameterizes the effect of melt composition in terms of the absolute concentration of SiO₂ (rather than other empirical models which use cation fractions), it is extremely sensitive to normalization. For example, consider the MORB2 composition in Table 1 which has a measured SiO₂ content of 47.4 wt%, and an anhydrous total of 96.95 wt%. For 1,000 ppm CO₂ and $T = 1,200^{\circ}\text{C}$, using raw data (SiO₂ = 47.4 wt%) the calculated saturation pressure is 1,227 bars. However, it is relatively common in the literature that major elements (excluding volatiles) are scaled to sum to 100%, while volatile concentrations are left unchanged. This would cause the melt

SiO₂ content to increase to 48.89 wt% SiO₂, corresponding to a saturation pressure of 1947 bar, respectively (1.6 \times higher!). We encourage users not to normalize their data, as we note that the Π -SiO₂ plot of North Arch Glasses in Dixon (1997) is best recreated using unnormalized data (see Figure S1 in Supporting Information S1). Unnormalized data is used throughout this review for all VolatileCalc-Basalt outputs, which gives results comparable to those produced in the VolatileCalc-Basalt spreadsheet when users enter the SiO₂ contents given in Table 1.

3.2. VolatileCalc-Rhyolite: Newman and Lowenstern (2002)

In addition to the functionality for basalts described above, the VolatileCalc spreadsheet also allows users to calculate saturation pressures, degassing paths, isobars, and isopleths for rhyolitic magmas (hereafter, VolatileCalc-Rhyolite). For CO₂, VolatileCalc-Rhyolite uses the simple thermodynamic model from Stolper et al. (1987) that was later applied to rhyolitic melts by Fogel and Rutherford (1990). The molar enthalpy change for CO₂ dissolution in the melt is from Fogel and Rutherford (1990), the single-O melt mass from Silver et al. (1990), and the CO₂ molar volume and solubility at standard state from Blank et al. (1993). The thermodynamic basis for the H₂O model is the same as that used in VolatileCalc-Basalt. The fitted parameters for H₂O solubility in the standard state is from Silver (1988), and the single-O melt mass and molar enthalpy change for H₂O dissolution in the melt from Silver et al. (1990). The partial molar volume of H₂O was adjusted to 5 cm³/mol to provide a better fit to experimental data. There are two main differences of the rhyolite model relative to the basaltic model. First, while both the models use a temperature-dependent equation of state, VolatileCalc-Rhyolite model also contains a term for the heat of solution of volatile solubility, so is far more sensitive to temperature (see Section 5). Second, unlike VolatileCalc-Basalt which require users to enter melt SiO₂ contents, VolatileCalc-Rhyolite is independent of melt composition. Thus, Newman and Lowenstern (2002) caution that this model may not be applicable for strongly peralkaline or peraluminous rhyolites.

3.3. M-1998 (Moore et al., 1998)

The Moore et al. (1998) model calculates the solubility of H_2O for a wide range of silicate melt compositions using an empirical expression valid between 700°C–1,200°C and 0–3,000 bars:

$$2 \ln(X_{\text{H}_2\text{O}}^{\text{melt}}) = \frac{a}{T} + \sum_i b_i X_i \frac{P}{T} + c \ln(f_{\text{H}_2\text{O}}^{\text{fluid}}) + d \quad (4)$$

where $X_{\text{H}_2\text{O}}^{\text{melt}}$ is the mole fraction of H_2O dissolved in the melt, T is the temperature in Kelvin, P is the pressure in bars, and X_i is the anhydrous molar fraction of each oxide component. $f_{\text{H}_2\text{O}}^{\text{fluid}}$ is the fugacity of H_2O in the fluid, calculated using the modified version of the Redlich-Kwong equation of state provided in the appendix of Holloway and Blank (1994). Equation 4 is associated with the following fit parameters (\pm standard error):

Coefficient	a	$b_{\text{Al}_2\text{O}_3}$	b_{FeO_T}	$b_{\text{Na}_2\text{O}}$	c	d
Value ($\pm 1\sigma$)	2565 (± 362)	-1.997 (± 0.706)	-0.9275 (± 0.394)	2.736 (± 0.871)	1.171 (± 0.069)	-14.21 (± 0.54)

As Equation 4 includes a term for the fugacity of H_2O in the fluid, this model can be integrated with CO_2 models implemented in VESIcal (e.g., the $\text{H}_2\text{O}-\text{SiO}_2$ simplification of Allison et al., 2019; Dixon, 1997; Iacono-Marziano et al., 2012; Liu et al., 2005; Shishkina et al., 2014) to investigate mixed $\text{H}_2\text{O}-\text{CO}_2$ fluids.

The model calibration dataset combines the authors' pure H_2O experiments with literature data, spanning sub-alkaline basaltic to rhyolitic compositions, as well as some alkaline compositions (Figure 2). As with other fully empirical models implemented in VESIcal, or those including empirical expressions, extreme care must be taken when extrapolating this model outside of the calibration range. In particular, the authors warn against extrapolating this model to pressures exceeding 3 kbar, in part due to the complexities of the critical behavior of fluids at higher pressures.

3.4. L-2005 (Liu et al., 2005)

The Liu et al. (2005) model calculates the solubility of H_2O and CO_2 in metaluminous, high-silica rhyolitic melts using empirical expressions, valid between 700°C–1,200°C and 0–5,000 bars. The following expression is used to calculate CO_2 solubility:

$$[\text{CO}_2]^{\text{ppm}} = \frac{P_{\text{CO}_2}(b_1 + b_4 P_w)}{T} + P_{\text{CO}_2}(b_2 P_w^{0.5} + b_3 P_w^{1.5}) \quad (5)$$

T is temperature in Kelvin, b_1 – b_4 are fit parameters, and the P_w and P_{CO_2} terms account for the partial pressures of each volatile species in the co-existing fluid, with:

$$P_{\text{CO}_2} = X_{\text{CO}_2}^f P \quad (6)$$

$$P_w = X_w^f P \quad (7)$$

where P is pressure in MPa, $X_{\text{CO}_2}^f$ is the mole fraction of CO_2 in the fluid, and X_w^f is the mole fraction of H_2O in the fluid. These empirical terms mean that no equation of state is used (unlike M-1998 and VolatileCalc-Basalt). The fit parameters associated with Equation 5 are shown below (\pm error):

Coefficient	b_1	b_2	b_3	b_4
Value (Error)	5668 (± 127)	0.4133 (± 0.0491)	2.041×10^{-3} ($\pm 0.285 \times 10^{-3}$)	-55.99 (± 8.36)

Similarly, they provide the following expression for H_2O :

$$[\text{H}_2\text{O}_t]^{\text{wt}\%} = \frac{a_1 P_w^{0.5} + a_2 P_w + a_3 P_w^{1.5}}{T} + a_4 P_w^{1.5} + P_{\text{CO}_2}(a_5 P_w^{0.5} + a_6 P_w) \quad (8)$$

Using the following fit parameters:

Coefficient	a_1	a_2	a_3	a_4	a_5	a_6
Value (Error)	354.94 (± 4.55)	9.623 (± 0.923)	-1.5223 (± 0.0722)	1.2439×10^{-3} ($\pm 0.0499 \times 10^{-3}$)	-1.084×10^{-4} ($\pm 0.406 \times 10^{-4}$)	-1.362×10^{-5} ($\pm 0.352 \times 10^{-5}$)

The model calibration dataset combines pure H_2O solubility experiments by the authors between ~ 1 and 250 bars with literature experiments investigating the solubility of pure H_2O , $\text{H}_2\text{O}-\text{H}_2$, CO_2 , and $\text{CO}_2-\text{H}_2\text{O}$ fluids, spanning significantly higher pressures (up to 5,000 bars). Unlike the M-1998 model, their empirical expressions do not incorporate a term for melt composition, so care is needed when applying this model to melts with different major element compositions to the calibration dataset (Figure 2).

3.5. P-2006 (Papale et al., 2006)

Papale et al. (2006) present a fully non-ideal thermodynamic model for H_2O and CO_2 solubility, which is a recalibration of the earlier models of Papale (1997, 1999). This updated model capitalizes on the large amount of volatile solubility experiments performed between 1997 and 2005, which nearly doubled the size of the calibration dataset, and allowed experimental data on CO_2 solubility collected prior to 1980 to be discarded (removing systematic errors associated with different analytical techniques, see Papale, 1999). Unlike the models discussed above which are calibrated on a specific subregion of compositional space and use empirical parameterizations to account for the effect of melt composition, the models of Papale et al. (2006) and Papale (1999) treat the composition of the silicate liquid using a thermodynamic approach based on Ghiorso et al. (1983). Papale et al. (2006) note that this thermodynamic approach means that for any specific region of composition space (e.g., comparing model results to a specific experiment), the fit may not be as good as an empirical model tuned to that composition. However, carefully calibrated thermodynamic models will be significantly more successful than empirical models when applied to melts which are not represented in the calibration dataset.

P-2006 considers a silicate liquid in mechanical, thermal, and chemical equilibrium with a fluid phase containing H_2O and CO_2 . The model uses the modified Redlich-Kwong equation of state of Kerrick and Jacobs (1981) to describe the fluid phase, and considers only the dissolution of CO_2 and H_2O in the melt (while natural silicate melts contain molecular CO_2 and CO_3^{2-} species, and molecular H_2O and OH^- species). The model calculates the Gibbs free energy of mixing, considering 10 major oxide components in addition to CO_2 and H_2O . Binary interaction coefficients, denoted by w_{ij} , account for the attractive-repulsive behavior between an oxide and volatile component. For example, $w_{\text{CO}_2,\text{MgO}}$ describes the interaction of MgO with CO_2 . Interaction coefficients for CO_2 are expressed as a function of pressure (relative to a reference pressure of 0.1 MPa) requiring two coefficients, while those for H_2O are invariant of pressure (requiring 1 coefficient):

$$w_{\text{CO}_2,i} = w_{\text{CO}_2,i}^0 + w_{\text{CO}_2,i}^1 \ln \frac{P}{P_0} \quad (9)$$

$$w_{\text{H}_2\text{O},i} = w_{\text{H}_2\text{O},i}^0 \quad (10)$$

P-2006 uses interaction terms for SiO_2 , Al_2O_3 , MgO , CaO , Na_2O , K_2O , FeO , and Fe_2O_3 . The presence of two Fe terms means that the model is sensitive to melt redox. Papale et al. (2006) show that the inclusion of w terms for MnO and TiO_2 lead to overfitting, so the effect of these oxides on model outputs is only through the dilution of the concentration of components allocated w terms. The values of the 24 w terms, as well as 5 terms accounting for molar volumes and fugacities, are calculated from a calibration dataset comprising $\sim 1,100$ solubility experiments with pure CO_2 , pure H_2O and mixed $\text{CO}_2-\text{H}_2\text{O}$ fluids. While the calibration dataset contains well populated clusters for basaltic and rhyolitic compositions, intermediate compositions, and basaltic melts with high alkali contents are poorly represented, particularly for CO_2 (Figure 2).

Papale et al. (2006) demonstrate that despite the addition of hundreds of new experimental datapoints for H_2O , there are no significant changes in coefficients compared to those which were published with their 1999 model. The percent errors on the H_2O coefficients in the 2006 model are $< 10\%$ for all species (defined as $100 \times \sigma/\text{co}$ -

P-2006

Element	CO ₂				H ₂ O	
	w ₀	% error (1 σ)	w ₁	% error	w ₀	% error
SiO ₂	-59,962	18	6049	19	-34,093	1.85
Al ₂ O ₃	-590,957	32	41,395	47	-189,117	2.54
Fe ₂ O ₃	4,469,623	9	-529,301	9	135,935	9.32
FeO	21,666	806	1214	1500	-195,751	3.13
MgO	52,866	189	-13,446	78	-86,418	7.06
CaO	-328,792	23	12,789	63	-209,997	1.67
Na ₂ O	140,034	146	-35,213	60	-322,253	1.42
K ₂ O	309,070	48	-58,010	27	-349,798	1.79

MagmaSat

Element	CO ₂ -CO ₃ ²⁻				H ₂ O	
	W (CO ₂)	% error (1 σ)	W (CaCO ₃)	% error	W	% error
SiO ₂			63.281	2.52	27.557	0.065
TiO ₂	-19.266	1.34	-79.203	0.46	88.199	2.87
Al ₂ O ₃			46.716	2.52	11.768	21.8
Fe ₂ O ₃	-3.187	4.3	65.509	0.26	50.105	17.0
Fe ₂ SiO ₄	-32.465	0.95	-72.997	0.40	30.936	18.8
Mg ₂ SiO ₄	-40.854	1.6	-24.873	4.17	20.910	21.5
CaSiO ₃	30.012	4.8	37.534	2.70	9.715	27.5
Na ₂ SiO ₃			-311.011	0.24	-82.460	2.9
KAlSiO ₄			-27.865	8.21	1.057	112
Ca ₃ (PO ₄) ₂	-3.473	0.86	2.012	2.49	44.133	0.76

Figure 3. Interaction coefficients for P-2006 and MagmaSat. Percentage errors calculated as $100 \times 1\sigma/\text{coefficient}$. Error are colored green if they are $<10\%$, light pink if $10\%-25\%$, and red if $>25\%$.

efficient). In contrast, the addition of new CO₂ data to the calibration dataset resulted in significant changes in coefficients, and the percentage errors on these coefficients in the 2006 model remained large ($\sim 800\%$ for FeO, $\sim 150\%$ for Na₂O, and $\sim 190\%$ for MgO; Figure 3). Based on these large errors, these coefficients would likely change again if this model was recalibrated to include new CO₂ experiments published since 2006.

The pressure-dependence of the CO₂ melt interaction terms, combined with the fact that the w₀ and w₁ terms have different signs for all oxides except FeO, means that a given change in melt chemistry may cause an increase in CO₂ solubility at one pressure, but a decrease at another pressure (see Section 4.1). Ghiorso and Gualda (2015) note that the coefficient for the compressibility of CO₂ in the P-2006 model is negative, which is physically impossible (implying the volume of the CO₂ fluid increases when pressure is increased), which they suggest may arise from the inclusion of pressure-dependent w-terms.

3.6. IM-2012 (Iacono-Marziano et al., 2012)

The Iacono-Marziano et al. (2012) model expresses the solubility of H₂O and CO₂ in mafic melts by combining simplified thermodynamic expressions for melt-fluid thermodynamics with empirical formulations accounting for melt composition. For CO₂, they present the following expression:

$$\ln[\text{CO}_2]^{\text{ppm}} = X_{\text{H}_2\text{O}} d_{\text{H}_2\text{O}} + X_{\text{Al}} d_{\text{Al}} + X_{\text{FeO}+\text{MgO}} d_{\text{FeO}+\text{MgO}} + X_{\text{Na}_2\text{O}+\text{K}_2\text{O}} d_{\text{Na}_2\text{O}+\text{K}_2\text{O}} + a_{\text{CO}_2} \ln[\text{P}_{\text{CO}_2}] + b_{\text{CO}_2} \left[\frac{NBO}{O} \right] + B_{\text{CO}_2} + C_{\text{CO}_2} \frac{P}{T} \quad (11)$$

where P is the pressure in bars, T is the temperature in Kelvin, X_{H₂O} is the molar fraction of H₂O in the melt, and P_{CO₂} is the partial pressure of CO₂ in bars. The partial pressure of CO₂ is calculated from the pressure multiplied by the mole fraction of CO₂ in the fluid. This means that this model does not rely on an equation of state (as with the L-2005 model). The other terms account for the effect of melt composition using molar fractions calculated on a hydrous basis; X_{FeO + MgO} is the sum of molar fractions of FeO_t and MgO, X_{Na₂O} + K₂O is the sum of the molar fractions of Na₂O and K₂O, and X_{Al} is the agpaitic index (AI):

$$X_{\text{Al}} = \frac{X_{\text{Al}_2\text{O}_3}}{X_{\text{CaO}} + X_{\text{K}_2\text{O}} + X_{\text{Na}_2\text{O}}} \quad (12)$$

The NBO/O term represents the number of non-bridging oxygens divided by oxygen, expressing the availability of oxygen to form carbonate groups within the melt. NBO/O can be calculated from mole fraction of different oxides, X_i , on an anhydrous or hydrous basis:

$$\frac{\text{NBO}}{\text{O}}^{\text{Anhyd}} = \frac{2(X_{\text{K}_2\text{O}} + X_{\text{Na}_2\text{O}} + X_{\text{CaO}} + X_{\text{MgO}} + X_{\text{FeO}} - X_{\text{Al}_2\text{O}_3})}{2X_{\text{SiO}_2} + 2X_{\text{TiO}_2} + 3X_{\text{Al}_2\text{O}_3} + X_{\text{MgO}} + X_{\text{FeO}} + X_{\text{CaO}} + X_{\text{Na}_2\text{O}} + X_{\text{K}_2\text{O}}} \quad (13)$$

$$\frac{\text{NBO}}{\text{O}}^{\text{Hyd}} = \frac{2(X_{\text{H}_2\text{O}} + X_{\text{K}_2\text{O}} + X_{\text{Na}_2\text{O}} + X_{\text{CaO}} + X_{\text{MgO}} + X_{\text{FeO}} - X_{\text{Al}_2\text{O}_3})}{2X_{\text{SiO}_2} + 2X_{\text{TiO}_2} + 3X_{\text{Al}_2\text{O}_3} + X_{\text{MgO}} + X_{\text{FeO}} + X_{\text{CaO}} + X_{\text{Na}_2\text{O}} + X_{\text{K}_2\text{O}} + X_{\text{H}_2\text{O}}} \quad (14)$$

In both cases, mole fractions are calculated on a hydrous basis (Iacono-Marziano, Written Communication). Iacono-Marziano give coefficients for Equation 11 for both cases ($\pm 2\sigma$), leading to two forms of this model: IM-2012-A (anhydrous) and IM-2012-H (hydrous):

Coefficient	$d_{\text{H}_2\text{O}}$	d_{Al}	$d_{\text{FeO}+\text{MgO}}$	$d_{\text{Na}_2\text{O}+\text{K}_2\text{O}}$	a_{CO_2}	b_{CO_2}	C_{CO_2}	B_{CO_2}
Hydrous Value ($\pm 2\sigma$)	-16.4 (± 1.2)	4.4 (± 0.4)	-17.1 (± 0.9)	22.8 (± 1.1)	1 (± 0.03)	17.3 (± 0.9)	0.12 (± 0.02)	-6 (± 0.4)
Anhydrous Value ($\pm 2\sigma$)	2.3 (± 0.5)	3.8 (± 0.4)	-16.3 (± 0.9)	20.1 (± 1.1)	1 (± 0.03)	15.8 (± 0.9)	0.14 (± 0.02)	-5.3 (± 0.4)

We note for completeness that in the original publication, Equation 11 was incorrectly expressed in terms of $\ln[\text{CO}_3^{2-}]$ (Iacono-Marziano, Written Communication).

For H_2O , the authors state that it is statistically unjustified to include d_i terms similar to those in the CO_2 expression, due to the relatively small effect of melt composition on H_2O solubility. The effect of melt composition is incorporated only through the NBO/O term:

$$\ln [\text{H}_2\text{O}]^{\text{wt}\%} = a_{\text{H}_2\text{O}} \ln[\text{P}_{\text{H}_2\text{O}}] + b_{\text{H}_2\text{O}} \left[\frac{\text{NBO}}{\text{O}} \right] + B_{\text{H}_2\text{O}} + C_{\text{H}_2\text{O}} \frac{P}{T} \quad (15)$$

where $\text{P}_{\text{H}_2\text{O}}$ is the partial pressure of H_2O in bars. As for CO_2 , coefficients are provided for NBO/O calculated on a hydrous and anhydrous basis. The hydrous coefficients in the published paper differ from those used in the web app over the last decade (although a new web app using the published coefficients appeared briefly in 2021). VESical uses the web app hydrous coefficients by default, as recommended by Iacono-Marziano (Written Communication). The coefficients in the published paper were from an older version of the model, and predict extremely high H_2O solubility at ~ 10 kbar (> 100 wt%).

The authors state that the differences between calculations performed with NBO/O calculated on a hydrous and anhydrous basis are relatively small, but that a slightly better fit to experimental data is obtained using the hydrous model (particularly for H_2O -rich, and CO_2 -poor melts). For completeness, we perform calculations using both versions (referred to as IM-2012-H and IM-2012-A). Interestingly, we show that the anhydrous version is more similar to other models for MORB-like compositions than the hydrous version.

The calibration dataset for CO_2 combines the authors experiments with those from a variety of literature studies for mixed $\text{H}_2\text{O}-\text{CO}_2$ fluids, spanning temperatures between 1,100°C and 1,400°C, and pressures between 100 and

Coefficient	$a_{\text{H}_2\text{O}}$	$b_{\text{H}_2\text{O}}$	$B_{\text{H}_2\text{O}}$	$C_{\text{H}_2\text{O}}$
Hydrous Value ($\pm 2\sigma$)	0.53 (± 0.02)	2.35 (± 0.28)	-3.37 (± 0.13)	-0.02 (± 0.02)
Anhydrous Value ($\pm 2\sigma$)	0.54 (± 0.02)	1.24 (± 0.28)	-2.95 (± 0.17)	0.02 (± 0.02)
Web App Value	0.52096846	2.11575907	-3.24443335	0.02238884

10,000 bars (but mostly <5,000 bars). The calibration dataset for H_2O incorporates pure H_2O experiments from the literature (spanning 163–6,067 bars and 1,000°C–1,250°C), as well as the experiments on $\text{H}_2\text{O}-\text{CO}_2$ fluids used to calibrate the CO_2 expression. Melt compositions are predominantly mafic, spanning subalkaline-alkaline basalts to basaltic andesites (45–57 wt% SiO_2 for mixed $\text{H}_2\text{O}-\text{CO}_2$ experiments, and 46–63 wt% SiO_2 for pure H_2O ; Figure 2).

The empirical nature of the fitting terms incorporating melt composition, pressure and temperature means that users should be cautious when extrapolating this model to conditions lying outside the P - T - X range of the calibration dataset. In particular, Iacono-Marziano et al. (2012) highlight five limitations of their model:

1. The effect of melt MgO and FeO contents on CO_2 solubility is poorly constrained, because of the small variation in the concentrations of these oxides in the calibration database.
2. While their compositional terms for the effect of melt composition on CO_2 solubility gives equal weight to Na_2O and K_2O , the calibration dataset only includes K_2O -rich melts with a range of pressures, so the effect of substituting Na and K is poorly constrained.
3. The effect of temperature on the solubility of mixed $\text{H}_2\text{O}-\text{CO}_2$ is poorly constrained because the majority of experiments in the calibration dataset were performed at 1,200°C–1,300°C.
4. The relative role of molecular H_2O versus OH^- on melt structure, which in turn influences CO_2 solubility, needs to be evaluated further.
5. The model was calibrated assuming that all Fe was Fe^{2+} , so calculated solubilities are not sensitive to melt redox (unlike the model of P-2006).

These limitations are explored in more detail in Sections 5 and 6.

3.7. S-2014 (Shishkina et al., 2014)

The Shishkina et al. (2014) model calculates the solubility of H_2O and CO_2 using fully empirical expressions. Their expression for CO_2 solubility was calibrated on a dataset of mixed $\text{H}_2\text{O}-\text{CO}_2$ experiments on predominantly mafic compositions between 1,200°C–1,300°C and 500–5,000 bars:

$$\ln[\text{CO}_2]^{\text{ppm}} = 1.150 \ln(P) + 6.71 \Pi^* - 1.345 \quad (16)$$

where P is the pressure in MPa, and Π^* is a compositional parameter expressed in terms of the cation fractions of seven species:

$$\Pi^* = \frac{X_{\text{Ca}^{2+}} + 0.8 X_{\text{K}^+} + 0.7 X_{\text{Na}^+} + 0.4 X_{\text{Mg}^{2+}} + 0.4 X_{\text{Fe}^{2+}}}{X_{\text{Si}^{4+}} + X_{\text{Al}^{3+}}} \quad (17)$$

We note for completeness that the expression provided in Shishkina et al. (2014) incorrectly states that CO_2 in Equation 16 was in wt%, rather than ppm.

Their expression for H_2O solubility was calibrated on a dataset of pure H_2O experiments with mafic to intermediate compositions between 1,200°C–1,250°C and 485–5,009 bars. It incorporates a composition parameter expressed in terms of the anhydrous cation fractions of Na and K:

$$\begin{aligned} [\text{H}_2\text{O}]^{\text{wt\%}} = & (3.36 \times 10^{-7} P^3 - 2.33 \times 10^{-4} P^2 - 0.0711 P - 1.1309)(X_{\text{Na}} + X_{\text{K}}) \\ & - 1.2 \times 10^{-5} P^2 + 0.0196 P + 1.1297 \end{aligned} \quad (18)$$

In general, the compositional range of the Shishkina et al. (2014) dataset includes a larger variety of mafic compositions than that of Iacono-Marziano et al. (2012), particularly with respect to alkali-rich, or highly depolymerized melts (Figure 2). However, as was true for IM-2012, the empirical nature of the compositional term means that extreme care is needed when extrapolating this model beyond the compositional range of the calibration dataset (see Section 6).

One caveat of the implementation of this model in VESIcal is the treatment of mixing between CO_2 and H_2O . Shishkina et al. (2014) note that their experimental data shows evidence for significant non-ideality, with

isobars remaining almost horizontal between 0 and 4 wt% H_2O (see their Figure 6). However, the isobars shown on their plots are fitted to experimental data, rather than derived from their equations for CO_2 and H_2O solubility. These fits cannot be applied to melts with different compositions, and the authors give no guidance as to how to combine their equations for pure CO_2 and pure H_2O to reproduce this non-ideal behavior for any given melt composition. Thus, due to an absence of other information, VESIcal treats mixing between H_2O and CO_2 as ideal in this model. To emphasize this assumption, the $\text{H}_2\text{O}-\text{CO}_2$ model called ShishkinaIdealMixing in VESIcal.

3.8. MagmaSat: Ghiorso and Gualda (2015)

Ghiorso and Gualda (2015) present a comprehensive thermodynamic model (MagmaSat) for mixed $\text{H}_2\text{O}-\text{CO}_2$ solubility, calibrated on the most chemically diverse set of natural silicate melt compositions of all the models discussed thus far (Figure 2). For this reason, it is the default model in VESIcal. MagmaSat uses the equation of state of Duan and Zhang (2006) for the $\text{CO}_2-\text{H}_2\text{O}$ fluid, and is the volatile solubility model implemented in rhyolite-MELTS v.1.2 (Gualda et al., 2012). Thus, it is currently the only model which can be directly integrated with phase equilibrium calculations (e.g., to track microlite growth during degassing upon ascent, or post-entrapment modification to melt inclusions). Like P-2006, the model considers the Gibbs free energy of solution using interaction parameters (denoted with a capital W in this model), although, unlike in P-2006, these terms are independent of pressure (as well as temperature). The exact choice of components differs from that of P-2006, as MagmaSat adapts the formulation from Rhyolite-MELTS (e.g., Mg is considered as Mg_2SiO_4 ; Ghiorso & Sack, 1995). Unlike P-2006, MagmaSat considers the dissolution of CO_2 as both molecular CO_2 and carbonate species (as CaCO_3), with a set of W coefficients for each. MagmaSat assumes that water dissolves entirely as a hydroxyl species, rather than considering both hydroxyl and molecular species. This helps to reduce the number of interaction parameters for volatile-melt species, and seems to be a justified simplification based on available experimental data (see Ghiorso & Gualda, 2015 for a more detailed discussion).

The calibration dataset for H_2O spans 550°C–1420°C, and pressures of 0–20,000 bars, and for CO_2 spans 1,140°C–1,400°C and 0–30,000 bars. However, as discussed in detail later, care is required when interpreting H_2O solubility at pressures >10 kbar. Importantly, unlike P-2006, MagmaSat is not calibrated for synthetic liquids (e.g., compositions only containing a small number of oxide species like albite), so should only be applied to natural silicate liquid compositions.

3.9. A-2019: Allison et al. (2019)

Allison et al. (2019) present thermodynamic models to calculate CO_2 solubility for six different basaltic compositions from Stromboli (alkali basalt), Etna (trachybasalt), Vesuvius (phonotephrite), Erebus (phonotephrite), Sunset Crater (alkali basalt), and the San Francisco Volcanic Field (basaltic andesite, Figure 2). Specifically, they performed experiments at 1,200°C and ~4,000–6,000 bars to address the paucity of experiments examining CO_2 solubility in alkali systems at mid crustal pressures. In addition to these experiments, their models for Vesuvius, Etna, and Stromboli incorporate experiments from the literature, extending the calibration range of these three models to upper crustal pressures (see Figure 1). Unlike models which incorporate the effect of changing melt composition empirically (e.g., Iacono-Marziano et al., 2012; Newman & Lowenstern, 2002; Shishkina et al., 2014), Allison et al. (2019) determine the parameters $\Delta V_r^{0,m}$ (the molar volume change of the condensed components of the reaction) and $K_0(P_0, T_0)$; the equilibrium constant at the reference pressure and temperature) within their thermodynamic equation empirically for each of the six compositions they examine, and create six separate models (each of which contains no compositional dependence). The A-2019 models incorporate the modified Redlich-Kwong equation of state provided in the appendix of Holloway and Blank (1994).

Interestingly, Allison et al. (2019) show that CO_2 solubility does not simply scale with total alkali contents. Erebus melts have $\text{Na}_2\text{O} + \text{K}_2\text{O} = 8.8$ wt%, but dissolve less CO_2 than Etna and Vesuvius melts ($\text{Na}_2\text{O} + \text{K}_2\text{O} = 5.2$ and 7.8 wt%, respectively). They suggest that CaO , MgO , and Al_2O_3 may play a role in the lower solubility of Erebus compared to Etna, but the fact that five of the seven major elements they examine show notable differences between these melt compositions make it difficult to conclusively determine the origin of solubility variations.

Ideally, users would apply the A-2019 Etna model to lavas erupted at Etna, the Stromboli model to lavas erupted at Stromboli and so on. The absence of an empirical term for melt composition means that extreme care should be taken when applying these equations to alkaline lavas with different major element contents to those used in the experiments of Allison et al. (2019), even if the lavas originated from one of the six volcanoes they examine.

Allison et al. (2019) only present equations for CO_2 solubility, as their experiments were not designed to have a wide range of H_2O contents at different pressures, and their high $X_{\text{CO}_2}^f$ values mean that errors in their fluid fraction measurements propagate into large errors for H_2O fugacity (relative to the insignificant errors for CO_2 fugacity). In their supplementary spreadsheet, they integrate their CO_2 solubility models with a power law fit for water solubility developed specifically for Etna (Equation 2 of Lesne, Scaillet, Pichavant, Iacono-Marziano, & Beny, 2011). In VESIcal, users can combine any of the A-2019 carbon models with H_2O models from M-1998, IM-2012, and S-2014, or write their own.

4. Model Comparisons

To aid comparisons between models, we use a number of silicate melt compositions spanning a range of typical end-member compositions found in nature (Figure 2; Table 1) to examine the relationship between volatile solubility and pressure, the treatment of mixing between H_2O and CO_2 (manifested in the shapes of isobars), as well as sensitivity to parameters, such as temperature and oxygen fugacity. For basalts, we consider two mid-ocean ridge basalts (MORB1, 50.8 wt% SiO_2 , Dixon et al., 1995; MORB2, 47.4 wt% SiO_2 , Allan et al., 1989), one alkali basalt from Etna (48.8 wt% SiO_2 , Allison et al., 2019) and one arc basalt from Fuego (49.7 wt% SiO_2 , Lloyd et al., 2013). Calculations for the MORB and Etna compositions were performed at 1,200°C, while those for Fuego were performed at 1000°C to reflect the lower temperatures typical of more H_2O -rich basalts.

For rhyolitic magmas, we perform calculations at 800°C for a high-Si rhyolite from Mono Craters (Eastern California) with 77.19 wt% SiO_2 from Liu et al. (2005), and a peralkaline rhyolitic melt inclusion from Aluto Volcano with 73.5 wt% SiO_2 measured by Iddon and Edmonds (2020). The Aluto rhyolite has much lower Al_2O_3 and higher FeO contents than the Mono Craters Rhyolite (Table 1).

4.1. Redox Sensitivity

Before proceeding with these comparisons, it is worth noting that the vast majority of studies report whole-rock, melt inclusion and matrix glass compositions in terms of FeO_t , because the proportions of FeO versus Fe_2O_3 are difficult to determine precisely using common analytical techniques such as electron probe microanalysis (EPMA) and X-ray fluorescence (XRF). VolatileCalc-Rhyolite and L-2005 have no compositional terms, and VolatileCalc-Basalt is only parametrized in terms of the melt SiO_2 content, so these three models are not sensitive to the choice of FeO versus Fe_2O_3 for the representative compositions in Table 1. Similarly, IM-2012 and M-1998 are parameterized using an FeO_t term, so also show no sensitivity to melt redox. S-2014 is technically slightly redox-sensitive for CO_2 , because the Π^* term is expressed in terms of Fe^{2+} species (Equation 17). However, as the model was calibrated assuming $\text{Fe}^{2+} = \text{Fe}_T$, any sensitivity to redox is likely spurious. Thus, VESIcal calculates Π with Fe_T by default for consistency with the calibration. In Figure 4, we perform calculations for different Fe^{3+} ratios for completeness, but the rest of the figures in the manuscript for S-2014 are calculated using Fe_T . H_2O solubility in S-2014 is not redox sensitive, because the effect of melt composition is only parametrized in terms of cation fractions of Na and K (Equation 18). Both P-2006 and MagmaSat have interaction parameters for Fe^{2+} and Fe^{3+} -bearing species, so are redox sensitive for both CO_2 and H_2O solubility.

We examine the sensitivity of calculations using S-2014, MagmaSat and P-2006 to melt redox by performing calculations for 0% and 20% Fe^{3+} for MORB2, and 0% and 60% Fe^{3+} for Etna (the higher redox accounting for the highly oxidising conditions of experiments on Etna melts, e.g., Lesne, Scaillet, Pichavant, & Beny, 2011).

For Etna, pure H_2O solubility in MagmaSat is relatively insensitive to redox, predicting variations in dissolved H_2O which are well within model error (Figure 4a). Pure CO_2 solubility in MagmaSat is more redox sensitive than H_2O , predicting ~ 1.2 to $1.3 \times$ more CO_2 for 0% Fe^{3+} versus 60% Fe^{3+} (Figure 4b). Pure H_2O solubility in P-2006 shows the same directionality as MagmaSat, but is more sensitive to redox ($1.8 \times$ more H_2O dissolves at 0.1 kbar for 0% Fe^{3+} vs. 60% Fe^{3+} , dropping to $1.2 \times$ at > 2 kbar). Pure CO_2 solubility in P-2006 is extremely redox-sensitive, with melts with 0% Fe^{3+} versus 60% Fe^{3+} dissolving $25 \times$ more CO_2 at 0.5 kbar, but $0.5 \times$ less CO_2 at 5 kbar. S-2014 is slightly less redox sensitive than MagmaSat for CO_2 .

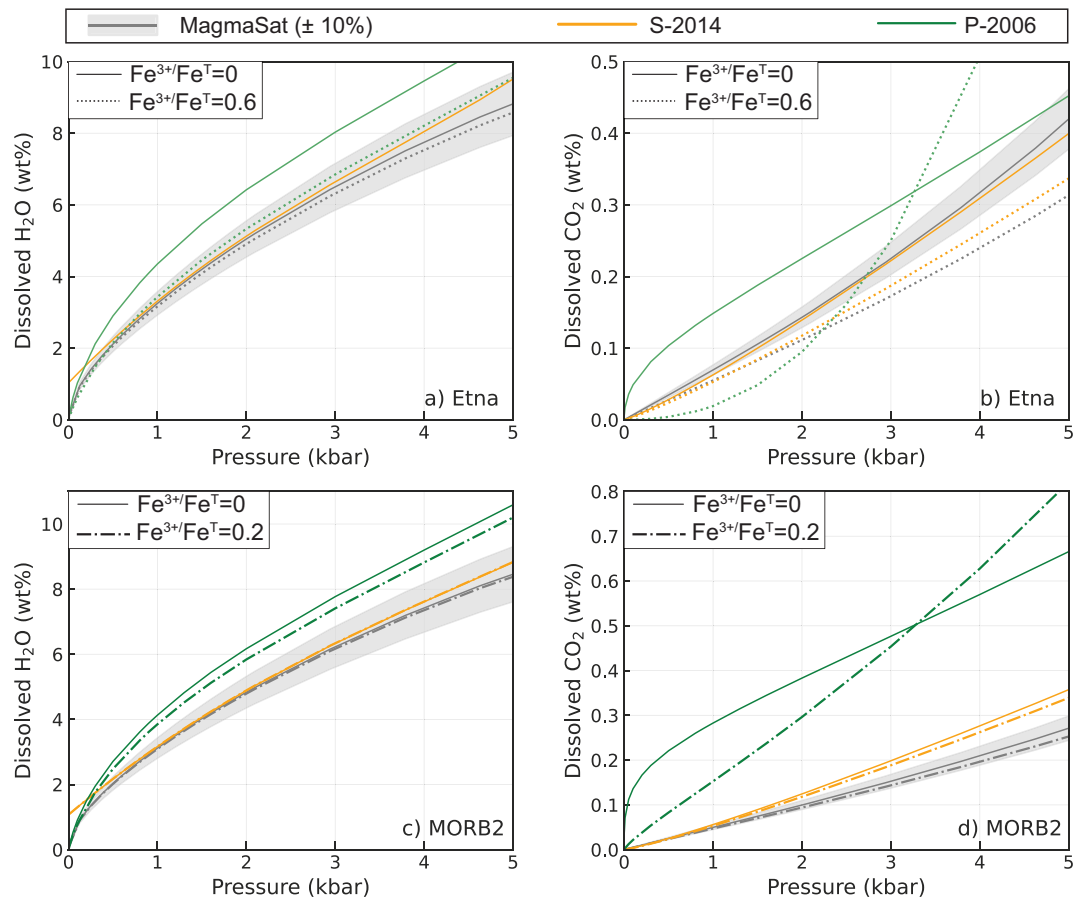


Figure 4. Relationship between volatile solubility and the proportion of Fe^{3+} for: (a) and (b) the Etna composition at $1,200^\circ\text{C}$; (c) and (d) the MORB2 composition at $1,200^\circ\text{C}$. VESIcal uses FeO_t in S-2014 to calculate Π^* for consistency with the calibration of this model. Here, dashed and dotted lines show the results from calculations where FeO_t is multiplied by $\text{Fe}^{2+}/\text{Fe}_T$, to show the results that would be obtained if VESIcal calculated Π^* using only Fe^{2+} . Isobars for MORB2 and lines for intermediate Fe^{3+} ratios for each composition are shown in Figure S2 in Supporting Information S1.

Varying Fe^{3+} proportions between 0% and 20% for MORB2 produces similar patterns as Etna, with changes lying within model error for MagmaSat and S-2014, but showing significant differences for P-2006 (Figures 4c and 4d). Isobars for different redox states for MORB2 can be found in Figure S2 in Supporting Information S1.

The cause of the extreme sensitivity of CO_2 in P-2006 to redox relative to MagmaSat is apparent from examining the interaction coefficients in Figure 3. In MagmaSat, the $W_{\text{Fe}_2\text{O}_3, \text{H}_2\text{O}}$ coefficient is only $1.6\times$ bigger than $W_{\text{Fe}_2\text{SiO}_4, \text{H}_2\text{O}}$ (~ 50 vs. 31), and these two coefficients overlap within $\pm 1.5\sigma$ of the uncertainty of these coefficients. This accounts for the relatively weak effect of redox on calculated H_2O solubility. For the CaCO_3 component representing the carbonate ion, the coefficients have similar magnitudes, but opposite signs ($W_{\text{Fe}_2\text{O}_3, \text{CaCO}_3} \sim 66$, $W_{\text{Fe}_2\text{SiO}_4, \text{CaCO}_3} \sim -73$), and this difference is much larger than the error on the coefficients (accounting for the stronger effect of melt redox on CO_2 solubility compared with H_2O). The Fe_2O_3 and Fe_2SiO_4 coefficients for the CO_2 component (which becomes more dominant in more evolved compositions) are also significantly different outside the quoted error but have the same sign ($W_{\text{Fe}_2\text{O}_3, \text{CO}_2} \sim -32$, $W_{\text{Fe}_2\text{SiO}_4, \text{CO}_2} \sim -3$).

In P-2006, the $w_{\text{H}_2\text{O}-\text{FeO}}^0$ coefficient is of similar magnitude, but opposite sign to $w_{\text{H}_2\text{O}-\text{Fe}_2\text{O}_3}^0$ (1.4×10^5 vs. -2×10^5), and clearly distinct outside the error on each coefficient. This accounts for the slightly stronger sensitivity of H_2O in P-2006 to redox compared with MagmaSat. In stark contrast to all the comparisons thus far, the $w_{\text{CO}_2-\text{Fe}_2\text{O}_3}^0$ coefficient is $> 200\times$ larger than $w_{\text{CO}_2-\text{FeO}}^0$ for P-2006. In fact, $w_{\text{CO}_2-\text{Fe}_2\text{O}_3}^0$ is $\sim 8\times$ higher than the next largest coefficient, suggesting that for a given mole fraction in the melt, it has the largest effect on carbonate ion solubility. The $w_{\text{CO}_2-\text{Fe}_2\text{O}_3}^1$ coefficient in P-2006 model, which becomes more dominant at higher pressures, has the opposite sign to that for w_0 . This accounts for the fact that at low pressures (< 3 kbar), increasing proportions

of Fe^{3+} cause CO_2 solubility to decrease, while at higher pressures, increasing proportions of Fe^{3+} cause CO_2 solubility to increase.

It is difficult to trust the extreme sensitivity of CO_2 in P-2006 to redox given the large uncertainty associated with the proportions of Fe^{3+} in volatile solubility experiments. For example, S-2014 note that only 7 of the 48 experiments in their calibration dataset contain non-zero values of Fe_2O_3 , which is why they choose to calibrate the model using FeO_t . In the P-2006 dataset, only six studies used in the calibration directly determined the proportion of Fe^{3+} , and a further nine reported the experimental oxygen fugacity. Thus, for the vast majority of their experimental calibration dataset, Papale et al. (2006) calculate the proportion of Fe^{3+} assuming the oxygen fugacity is controlled by the $\text{H}_2\text{O}-\text{H}_2$ equilibrium at the stated experimental conditions. However, this method requires accurate measurements of fluid composition, is affected by Fe and H^+ -loss during experiments, and it is unclear how applicable this method is for mixed $\text{H}_2\text{O}-\text{CO}_2$ experiments (Botcharnikov et al., 2006). The P-2006 calibration dataset contains some very surprising values: in the calibration dataset for pure CO_2 experiments, the experiments of Fogel and Rutherford (1990) have been allocated $\text{Fe}^{3+}/\text{Fe}_T$ ratios of $\sim 0.9-1$, despite the authors debating whether their experiments were actually reducing enough to stabilize a CO species. Overall, when evaluating P-2006, it is worth noting that the coefficients for CO_2 are relatively underconstrained. While there are 10 coefficients for H_2O calibrated using 865 datapoints of pure- H_2O solubility, there are 20 coefficients for CO_2 , and only 173 datapoints for pure- CO_2 solubility and 84 for mixed fluids. In particular, the highly oxidising $\text{Fe}^{3+}/\text{Fe}_T$ ratios calculated assuming $\text{H}_2\text{O}-\text{H}_2$ equilibrium are more concentrated in experiments with low CO_2 contents and pressures, making it difficult to deconvolve the differential effects of these parameters in a model with a large number of coefficients being calibrated on a relatively small calibration dataset.

In Sections 4.2–5, we show calculations using the $\text{Fe}^{3+}/\text{Fe}_T$ proportions in Table 1, as these best-estimates for each composition are representative of what a user would select when calculating melt inclusion saturation pressures, or dissolved volatile contents etc. For MORB1, MORB2, and Fuego, these proportions are from the original publications. For Etna, Fe_2O_3 was calculated from FeO_t assuming $\text{Fe}^{3+}/\text{Fe}_T = 0.26$ after Gaborieau et al. (2020). For Mono Craters and the Aluto pumice, $\text{Fe}^{3+}/\text{Fe}_T$ was set at 0.25 based on available data on other rhyolites (e.g., Ghiorso & Gualda, 2015), and modeling studies of the fractional crystallization path at Aluto (Gleeson et al., 2017).

4.2. Mafic Compositions

4.2.1. Pure H_2O

The seven models applicable to H_2O in basaltic systems predict a sharp rise in pure H_2O solubility with increasing pressure (Figure 5). For all three melt compositions, S-2014, IM-2012-A, VolatileCalc-Basalt, and M-1998 predict H_2O concentrations within $\pm 10\%$ of MagmaSat (gray envelope) between ~ 1 and 5 kbar. For MORB1 and MORB2, IM-2012-H begins to deviate to higher H_2O contents than MagmaSat at > 1 kbar. For Etna, IM-2012-H follows a similar trajectory between 0 and 3 kbar to the solubility model of Lesne, Scaillet, Pichavant, Iacono-Marziano, and Beny (2011) developed specifically for Etna melts (yellow line, Figure 5d). In contrast, P-2006 plots to substantially higher H_2O solubilities compared to all other models at > 0.5 kbar (although P-2006 and IM-2012-H intercept at higher pressures).

The fact that IM-2012-H predicts higher H_2O solubility relative to the cluster of other models lying within the error window of MagmaSat is an interesting observation. Iacono-Marziano et al. (2012) favor their hydrous model, particularly for CO_2 -poor, H_2O -rich melts, based on regressions between predicted and measured H_2O contents, and by comparing the two models to experiments conducted between 1 and 4 kbar on Etna melts (their Figure 7a). However, their Figure 8c, which compares dissolved volatile contents calculated by the model for the entire calibration dataset, shows that predicted H_2O contents using the hydrous version are overestimates for experimental products with $> 6-7$ wt% H_2O (although these predictions still lie within the $\sim 17\%$ error associated with their H_2O model). Our comparisons suggest that the anhydrous model is most similar to other models, so should not automatically be discounted in favor of the hydrous model.

Another notable oddity is the nearly linear trajectory of H_2O versus P in S-2014 at < 0.5 kbar, causing this model to predict a non-zero solubility of H_2O at 0 bar (Figure 5c). This contrasts with the power-law shapes followed by the other models which intercept very close to the origin. This anomalous behavior is because the S-2014 equation for H_2O solubility (Equation 18) simplifies at $P = 0$ to:

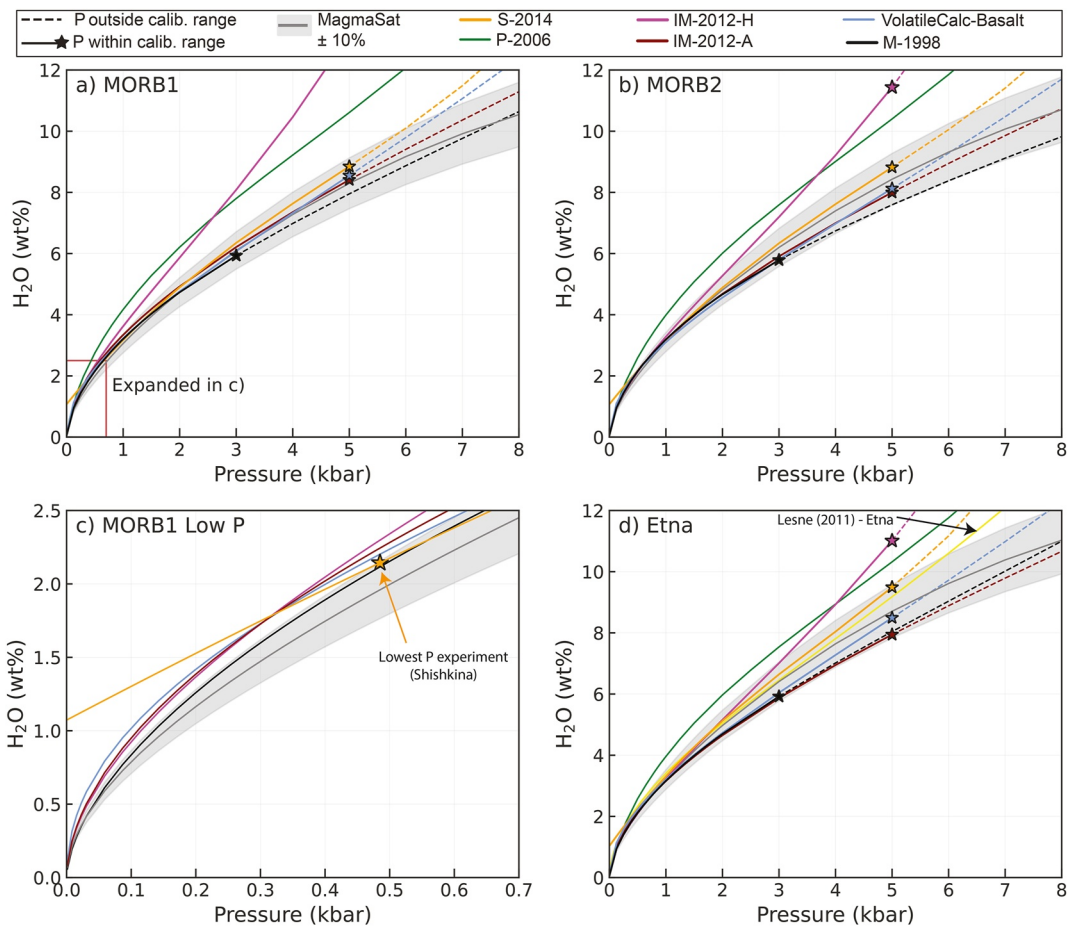


Figure 5. Relationship between pure H_2O solubility and pressure for MORB1 (a), MORB2 (b), and Etna (d) melts at 1,200°C. The gray field shows a $\pm 10\%$ error window around MagmaSat. Model lines are dashed when extrapolated above the recommended pressure range. The low pressure region of (a) is expanded in (c), emphasizing the non-zero solubility of H_2O at $P = 0$ bar in the S-2014 model.

$$[\text{H}_2\text{O}]^{\text{wt}\%} = -1.1309(\text{X}_{\text{Na}} + \text{X}_{\text{K}}) + 1.1297 \quad (19)$$

In the S-2014 calibration dataset, $\text{X}_{\text{Na}} + \text{X}_{\text{K}}$ varies from 0.05 to 0.25, which corresponds to solubilities of 0.85–1.07 wt% H_2O at 0 bar. This demonstrates the issue with extrapolating empirical expressions beyond the calibration range (the lowest pressure experiment in the calibration dataset of S-2014 was conducted at 485 bar). When combined with the assumption of ideal mixing used in VESical, this non-zero solubility of H_2O at 0 bar results in S-2014 predicting unusual degassing paths and isobar shapes relative to other models. For example, if a melt has <1 wt% H_2O , S-2014 predicts that the co-existing fluid contains no H_2O , despite abundant evidence that volcanic plumes in low H_2O systems, such as Hawai‘i are dominated by H_2O at low pressures (Gerlach, 1986). It also causes isobars to be entirely flat at low H_2O contents (see Section 4.2.2, Figure 6).

Overall, excluding P-2006 and IM-2012-H based on their higher predictions of H_2O solubility, and S-2014 based on anomalous behavior at low H_2O contents, the remaining four solubility models predict dissolved H_2O concentrations within error of one another at pressures lower than the upper calibration limit. This likely reflects the relatively small effect of melt composition on H_2O solubility, meaning that more recent models calibrated on a wider compositional range display similar behavior to older models (Moore & Carmichael, 1998; Papale et al., 2006). The larger deviation between models at higher pressures reflect the fact that very few pure- H_2O solubility experiments have been performed at > 5 kbar (Table 1). One reason for this paucity of higher pressure experimental data results from the fact that it is very difficult to quench silicate melts with >9 wt% H_2O to a glass phase which can be analyzed by FTIR or SIMS (Gavrilenko et al., 2019; Mitchell et al., 2017).

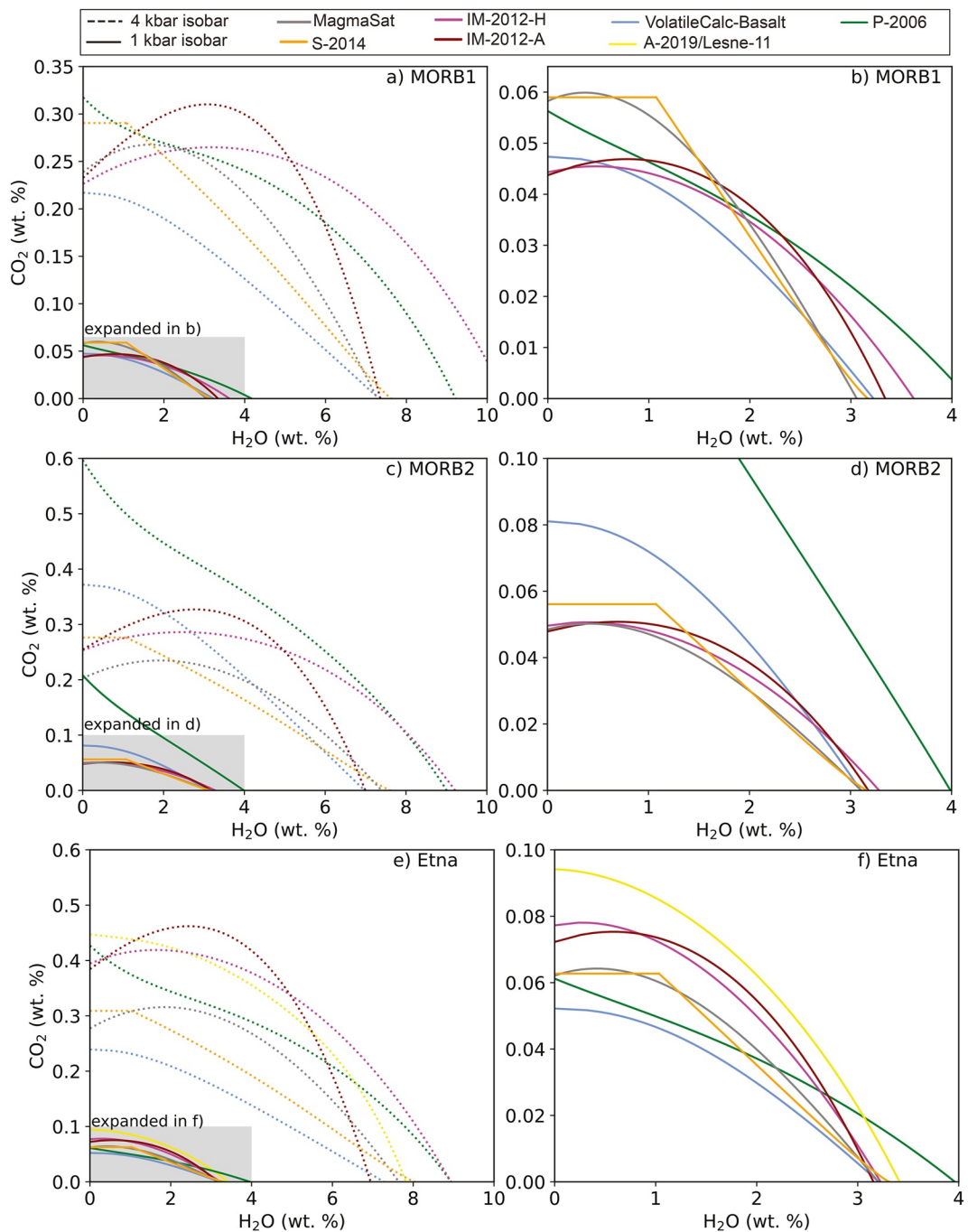


Figure 6. 1 and 4 kbar isobars for MORB1 (a) and (b) and MORB2 (c) and (d) and Etna (e) and (f) at 1,200°C. The 1 kbar isobar is expanded in (b), (d), and (e). The distinctive shapes of isobars from different models reflects treatment of $\text{H}_2\text{O}-\text{CO}_2$ mixing. These differences are most apparent at higher pressures.

4.2.2. Mixed $\text{H}_2\text{O}-\text{CO}_2$

The majority of experiments used to calibrate expressions for pure- CO_2 solubility contained dissolved H_2O and CO_2 (e.g., Allison et al., 2019; Iacono-Marziano et al., 2012; Shishkina et al., 2014), requiring authors to assess $\text{H}_2\text{O}-\text{CO}_2$ mixing behavior to determine the solubility of pure- CO_2 fluids. Thus, it makes sense to consider the treatment of mixing between CO_2 and H_2O in each model before considering predictions of pure CO_2 solubility which are affected by these assumptions. The treatment of $\text{H}_2\text{O}-\text{CO}_2$ mixing is best demonstrated using isobar

diagrams, which show the solubility of H_2O and CO_2 in a given silicate melt composition at a given pressure for proportions of $X_{\text{H}_2\text{O}}^f$ in the co-existing fluid ranging from 0 (interception with the y -axis) to 1 (interception with the x -axis). The treatment of mixed fluids differs quite considerably in each model.

VolatileCalc-Basalt models mixed fluids under the assumption of Henrian (ideal) mixing in the fluid and melt phase. Thus, the addition of H_2O always causes the solubility of CO_2 to decrease (and vice versa), and isobars possess a negative gradient, with a slightly sloping plateau at low H_2O contents merging into a concave-down shape (Figure 6).

S-2014 does not provide an equation for the treatment of non-ideal mixing, despite their experiments showing that increasing H_2O contents at high pressure cause almost no change in CO_2 solubility. Using the assumption of ideal mixing in VESIcal, S-2014 isobars exhibit a flat plateau at low H_2O contents, merging into a negative slope at higher H_2O contents. This flat plateau results from the fact that there are no partial pressures at which S-2014 yields $\text{H}_2\text{O} < 1$ wt%, so the y co-ordinate for lower H_2O contents is equal to the solubility of pure CO_2 .

P-2006 is fully non-ideal, which causes isobars to have complex shapes, exhibiting both positive and negative gradients. In detail, the shape of isobars calculated using P-2006 differ as a function of both melt composition and temperature (see Figure 12 of Papale, 1999). For the basaltic compositions considered here, isobars show a sharp decrease to lower CO_2 contents as a small amount of H_2O is added (Figures 6a and 6c).

IM-2012-A and IM-2012-H incorporate empirical representations of non-ideality through the inclusion of a term for the molar fraction of H_2O in the melt in their expression for CO_2 solubility (Equation 11). This means that these models predict that maximum CO_2 solubility occurs at non-zero H_2O concentrations, causing isobars to display prominent domed shapes (Figure 6). Isobars calculated using IM-2012-A show a more extreme peak than IM-2012-H, because of the difference in the sign and magnitude of the $d_{\text{H}_2\text{O}}$ coefficient combined with the differences between NBO/O calculated on a hydrous and anhydrous basis (see Supporting Information for further detail).

Like P-2006, MagmaSat is fully non-ideal. However, unlike P-2006, the treatment of non-ideality in MagmaSat predicts that the addition of small amounts of H_2O causes the solubility of CO_2 to increase (so isobars peak at non-zero H_2O concentrations; Figure 6c). This peak becomes more pronounced at higher pressures, but is generally smaller than that predicted by IM-2012.

These different mixing assumptions result in large discrepancies between the predicted volatile solubilities for melts in equilibrium with H_2O - CO_2 fluids, particularly at higher pressures where non-ideal behavior is more pronounced. For example, while IM-2012-A predicts similar pure CO_2 and pure H_2O solubilities to VolatileCalc-Basalt and MagmaSat for MORB1 at 4 kbar (interception with x - and y -axis on Figure 6a), IM-2012-A predicts that melts with ~ 4 wt% H_2O can dissolve more than twice as much CO_2 as that predicted by VolatileCalc-Basalt.

4.2.3. Pure CO_2

All basaltic compositions and models show a large increase in the solubility of pure CO_2 with increasing pressure (Figure 7). The solubility of pure CO_2 is approximately an order of magnitude lower than for H_2O (compare Figure 7 with Figure 5). This solubility difference accounts for the fact that Mid Oceanic Ridge (MOR) magmas, which have similar concentrations of H_2O and CO_2 (~ 0.07 wt% H_2O , 0.1–0.2 wt% CO_2 ; Le Voyer et al., 2019), are almost always CO_2 saturated during crustal storage (Saal et al., 2002) but only exsolve measurable quantities of H_2O if erupted at very low pressures (Le Voyer et al., 2019).

For MORB1, IM-2012-A and H, and VolatileCalc-Basalt lie within, or close to the $\pm 10\%$ error window on MagmaSat at < 5 kbar, and S-2014 lies within $\pm 20\%$ (Figure 7a). The deviation at higher pressures is expected, because only P-2006 and MagmaSat are calibrated on large numbers of experiments performed at > 5 kbar (Figure 1). For example, the relationship between Π and CO_2 solubility of Dixon (1997) used in VolatileCalc-Basalt was based on experiments at 1 kbar, and Newman and Lowenstern (2002) suggest that it should not be extrapolated above 5 kbar. Similarly, only the experiments of Jakobsson (1997) in the IM-2012 database were conducted at > 5 kbar, and there are no experiments in the calibration dataset of S-2014 performed at > 5 kbar. Unlike for pure H_2O , IM-2012-A and H predict very similar pure CO_2 solubilities to one another. This reflects the fact the coefficients for CO_2 between these two model versions are very similar apart from the $d_{\text{H}_2\text{O}}$ term, which is multiplied by a zero when calculating pure CO_2 solubility. Notably, P-2006 plots to significantly higher pressures than the other models ($\sim 2\times$ higher at ~ 8 kbar).

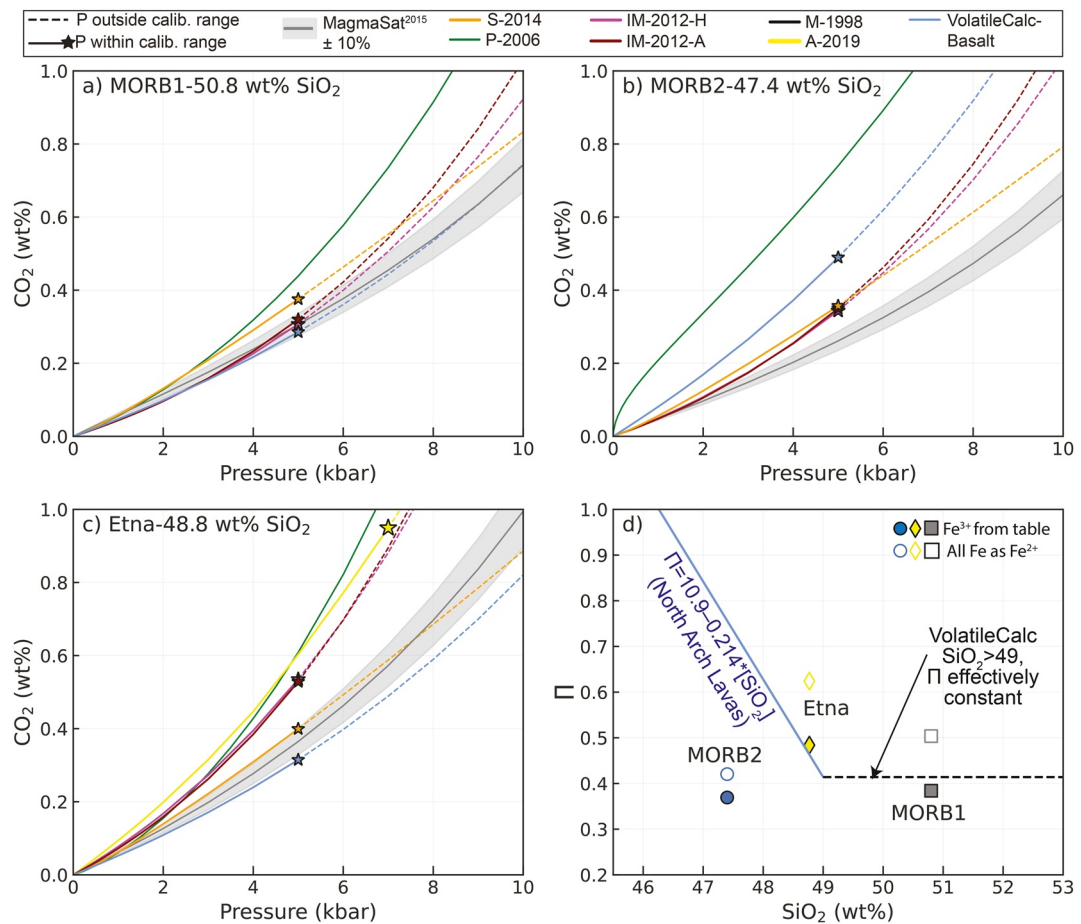


Figure 7. Relationship between pure CO₂ solubility and pressure for three mafic melts at 1,200°C: (a) MORB1 from Dixon et al. (1995), (b) MORB2 from Ghiorso and Gualda (2015), and (c) Etna from Allison et al. (2019). Models extrapolated beyond their calibrated pressure range are shown as dashed lines, with the colored star marking the recommended upper calibration limit. (d) The relationship between Π and SiO₂ defined by the North Arch lavas is shown in blue (Dixon, 1997). Generally, VolatileCalc-Basalt is applied to melts with >49 wt% SiO₂ by setting SiO₂ = 49 wt%; the black dashed line represents this extrapolation. These simplified relationships incorporated into VolatileCalc-Basalt (blue and black lines) underestimate the true Π value for Etna, and overestimate it for MORB2.

MORB2 shows a significantly larger discrepancy between models than MORB1 (Figure 7b). While S-2014, IM-2012-H, and IM-A follow very similar trajectories at <5 kbar, P-2006 predicts that MORB2 dissolves ~3,370 ppm CO₂ at 2 kbar while MagmaSat predicts only ~950 ppm (factor of 3.5×). VolatileCalc-Basalt also predicts higher CO₂ solubility relative to MagmaSat by a factor of 1.8× at 2 kbar.

The high CO₂ solubility predictions by P-2006 relative to other models and experimental measurements has also been noted by Shishkina et al. (2010), Shishkina et al. (2014), and Mangan et al. (2021). This may result from the fact that the P-2006 uses a negative compressibility for the CO₂ fluid (Ghiorso & Gualda, 2015). Alternatively, it may reflect the large errors on the CO₂ *w* coefficients, meaning that the effect of melt composition is uncertain, accounting for the larger discrepancy compared to other models for MORB1 versus MORB2. Finally, Shishkina et al. (2010) suggest that the overprediction of CO₂ solubility by P-2006 may result from the inclusion of anomalously high CO₂ contents from the experiments of Freise (2004) in the calibration dataset of P-2006 (these values have subsequently been revised to lower numbers, as the original FTIR thickness correction factor is thought to have been incorrect).

The fact that VolatileCalc-Basalt plots close to other models for MORB1 but not MORB2 is a good example of the main caveat of the Π -SiO₂ simplification used to account for the effect of melt composition on CO₂ solubility. For melts with 40–49 wt% SiO₂, VolatileCalc-Basalt assumes that the relationship between CO₂ solubility and

SiO_2 is identical to that defined by the North Arch lavas, shown in Π versus SiO_2 space as a blue line in Figure 7d. This is a reasonable approximation for the MORB1 composition, which has a Π value similar to North Arch Lavas with 49 wt% SiO_2 . However, the MORB2 composition lies significantly below the line defined by North Arch lavas, so has a lower Π value, and therefore a lower CO_2 solubility at a given SiO_2 content compared to the North Arch Lavas. Thus, by relying on the Π - SiO_2 relationship defined by the North Arch Lavas, Volatile-Calc-Basalt likely overpredicts the solubility of CO_2 in MORB2.

Furthermore, VolatileCalc-Basalt predicts that MORB2 dissolves ~ 1.7 times more CO_2 at a given pressure than MORB1. This is because MORB2 has 3.4 wt% less SiO_2 than MORB1, and VolatileCalc-Basalt predicts that CO_2 solubility increases drastically with decreasing SiO_2 . However, if the full Π expression of Dixon (1997) were used, MORB1 and MORB2 would have very similar CO_2 solubility, as they have similar Π values despite different SiO_2 contents. P-2006 also predicts that MORB2 dissolves 5–6 \times more CO_2 at 0.4 kbar, and 1.9 \times more at 4 kbar than MORB1. In contrast, the models of S-2014, IM-2012, and MagmaSat predict that MORB1 and MORB2 dissolve similar amounts of CO_2 (MORB2/MORB1 = $\sim 0.99\times$, $\sim 1.125\times$, and ~ 0.81 to $0.89\times$, respectively). These three more recent models utilize significantly larger basaltic calibration datasets to parametrize the effect of multiple oxide species melt on CO_2 solubility (Figure 2), so likely predict more realistic solubility relationships than VolatileCalc-Basalt and P-2006. In summary, CO_2 solubility in melt compositions that do not follow a similar trajectory in Π - SiO_2 space as the North Arch Lavas (Figure 7d) is unlikely to be accurately predicted by VolatileCalc-Basalt.

There is also significant deviation between different CO_2 models for Etna melts (Figure 7c), which is far greater than that observed for H_2O (Figure 5). The A-2019 model, developed specifically for the composition of Etna magmas, predicts much higher CO_2 solubility at a given pressure than VolatileCalc-Basalt, S-2014, and MagmaSat, while P-2006 and IM-2012-H and -A follow similar trajectories to A-2019. The success of both IM-2012 models likely reflects the large number of alkaline compositions in their calibration dataset, including some from Etna. VolatileCalc-Basalt predicts the lowest CO_2 solubility (factor of 0.5–0.6 \times that of A-2019). The calculated Π value for Etna lies significantly above the line defined by North Arch lavas (so VolatileCalc-Basalt predicts lower CO_2 solubility using the SiO_2 simplification; Figure 7d). However, even the full Π expression of Dixon (1997) is unlikely to be successful, because alkaline magmas show considerable variation in CO_2 solubility at a given Π value (Allison et al., 2019). As S-2014's expression for CO_2 solubility incorporates a Π^* term very similar to the Π term of Dixon (1997), the deviation of this model from that of A-2019 (0.6–0.7 \times) may also result from variations in CO_2 solubility that are not incorporated by this simplified melt composition parameter (Allison et al., 2019).

Interestingly, MagmaSat also underpredicts CO_2 concentrations at a given pressure relative to A-2019 by a factor of 0.6–0.7 \times , despite incorporating CO_2 experiments on Etna basalts from Lesne, Scaillet, Pichavant, and Beny (2011) and Iacono-Marziano et al. (2012) in its calibration dataset. This is a good example of the main pitfall of comprehensive models, such as MagmaSat and P-2006 which aim to predict volatile solubility across the entire range of natural silicate melt compositions (Papale et al., 2006). For any specific melt composition, comprehensive models are highly unlikely to be as well tuned as models calibrated on melts from a specific volcanic center (e.g., Allison et al., 2019) or heavily weighted toward a specific region of compositional space (e.g., Iacono-Marziano et al., 2012, for alkaline basalts). Tuning MagmaSat to provide a better fit to Etna would almost certainly cause this model to show larger discrepancies for experiments conducted on different melt compositions.

4.3. Silicic Compositions

4.3.1. Pure H_2O

All five H_2O models calibrated for silicic magmas (MagmaSat, P-2006, L-2005, VolatileCalc-Rhyolite and M-1998) predict very similar H_2O concentrations at <1 –1.5 kbar for the Mono Craters rhyolite composition (Figures 8a and Table 1). At higher pressures, P-2006, and to a much lesser extent L-2015, show a smaller increase in H_2O solubility with pressure compared to MagmaSat, M-1998 and VolatileCalc-Rhyolite (the difference in H_2O solubility between models reaches ~ 4 wt% at 5 kbar). As discussed for basalt, the large discrepancies at higher pressures and H_2O contents likely results from an absence of experimental constraints because of challenges related to quenching melts with >6 –9 wt% H_2O (Gavrilenko et al., 2019). The trajectories of models with compositional terms (M-1998, P-2006, and MagmaSat) are relatively similar for Aluto vs. Mono Craters.

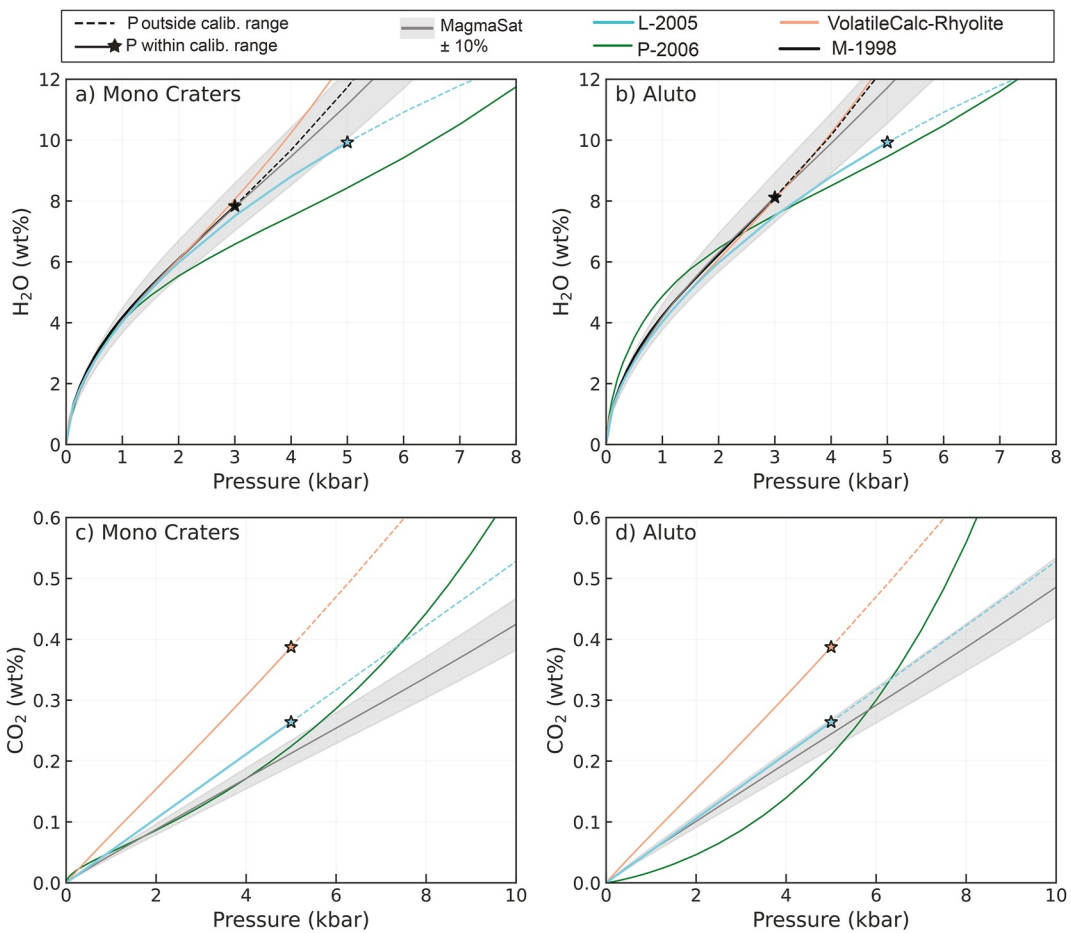


Figure 8. Relationship between pure H_2O (a) and (b) and pure CO_2 (c) and (d) solubility and pressure at 800°C for the Mono Lake rhyolite from Liu et al. (2005), and a peralkaline rhyolite from Aluto in the East African Rift (Iddon & Edmonds, 2020). Models extrapolated beyond their calibrated pressure range are shown as dashed lines, with the colored star marking the recommended upper calibration limit.

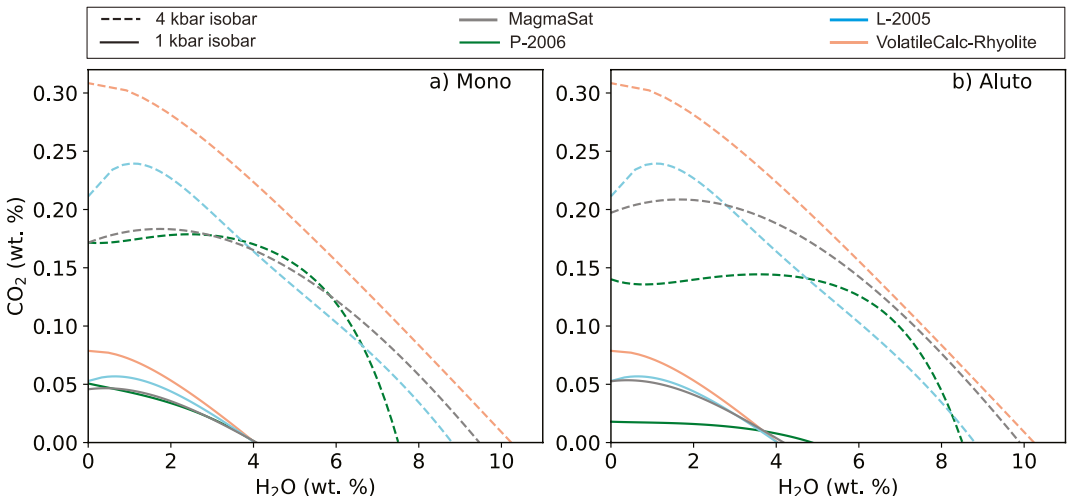


Figure 9. 1 and 4 kbar isobars for Mono Craters (a) and the Aluto rhyolite (b) at 800°C.

4.3.2. Mixed H₂O-CO₂

Differences in the treatment of H₂O-CO₂ mixing for rhyolitic melts are more subtle than for basaltic compositions (Figure 9). Unlike for basalts, the differences in isobar positions mostly result from large differences between the pure CO₂ solubility predicted by different models rather than different formulations of mixing. Only Volatile-Calc-Rhyolite assumes ideal mixing of H₂O-CO₂, causing isobars to have a negative gradient at all pressures. L-2005 accounts for non-ideal mixing through the inclusion of a term for the mole fraction of H₂O in the fluid in their expression for CO₂ solubility (Equation 5). This empirical representation of non-ideality causes isobars to exhibit a prominent peak at low H₂O contents (Figure 9). MagmaSat and P-2006, which include a fully non-ideal treatment of mixing, show a far less prominent peak than L-2005. The slight up-tick in the P-2006 isobars at very low H₂O contents is much smaller than for basaltic compositions (e.g., Figure 6).

4.3.3. Pure CO₂

Unlike the relatively good correspondence between rhyolite H₂O models (particularly at low pressures), there is substantial divergence between CO₂ models at all pressures (Figures 8c and 8d). For the Mono Craters rhyolite, VolatileCalc-Rhyolite predicts $\sim 1.8\times$ more dissolved CO₂ than MagmaSat at 2 kbar, while Liu, P-2006, and MagmaSat plot relatively close to each other at < 5 kbar. As VolatileCalc-Rhyolite and L-2005 have no compositional dependence, the model lines are identical for Mono Craters and Aluto. MagmaSat predicts that the Aluto composition has slightly higher CO₂ solubility at a given pressure compared to the Mono Lake composition (factor of $\sim 1.2\times$), so the discrepancy between MagmaSat, VolatileCalc-Rhyolite and L-2005 is smaller for Aluto than Mono Craters.

The P-2006 model shows a substantially different trajectory for CO₂ versus pressure compared to the other three solubility models for both rhyolite compositions, showing a strongly concave-up shape compared to the near linear trajectory of L-2005 and VolatileCalc-Rhyolite, and the slightly concave-up shape of MagmaSat (Figures 8c and 8d). For Mono Craters, P-2006 predicts similar CO₂ solubility to MagmaSat at < 4 kbar, but rapidly rises to higher CO₂ contents at higher pressures, predicting almost as much dissolved CO₂ as VolatileCalc-Rhyolite at ~ 12 kbar (Figure 8c). For Aluto, the curvature of the P-2006 model is even more prominent, predicting drastically lower CO₂ contents than all other models at < 6 kbar, and then rapidly rising, predicting higher CO₂ solubility than even VolatileCalc-Rhyolite at > 9 kbar (Figure 8d). These large deviations between models indicate that solubility calculations on rhyolites with non-negligible quantities of CO₂ are strongly affected by model choice. Given the large differences between models, more work is likely required to determine the effect of melt composition on CO₂ solubility at a range of pressures and temperatures.

4.4. Comparisons Between Basalts and Rhyolites

In this section, we briefly discuss the differences in solubility between basalts and rhyolites (comparing the MORB1 and Mono Craters composition). To differentiate the effect of melt composition from temperature (because basaltic melts tend to be hotter), we perform calculations at 800°C and 1,000°C for Mono Craters, and 1,000°C and 1,200°C for MORB1.

When all solubility models are compared (4 applicable to rhyolites, 6 to basalts), there is substantial overlap between curves calculated for MORB1 at 1,200°C and Mono Craters at 800°C (compare Figure 11a vs. Figure 8a). For simplicity, we compare the predictions from the three models which can be applied to both Rhyolites and Basalts: MagmaSat (Figures 10a and 10b), P-2006 (Figures 10c and 10d) and VolatileCalc-Basalt and -Rhyolite (Figures 10e and 10f).

MagmaSat and VolatileCalc (Rhyolite vs. Basalt) predict that Mono Craters dissolves more H₂O than MORB1 at realistic temperatures (800°C vs. 1,200°C) and at a fixed temperature (1,000°C). In contrast, P-2006 predicts that MORB1 dissolves more H₂O than Mono at realistic temperatures (although their solubilities are nearly identical when compared at 1,000°C). For CO₂, MagmaSat and P-2006 predict higher solubilities in MORB1, with the difference becoming more pronounced at higher pressures, while VolatileCalc predicts that at realistic temperature, Mono Craters has higher CO₂ solubility. When compared at the same temperature, VolatileCalc predicts very similar CO₂ solubility for Mono Craters and MORB1. These comparisons demonstrate that at < 5 kbar, the

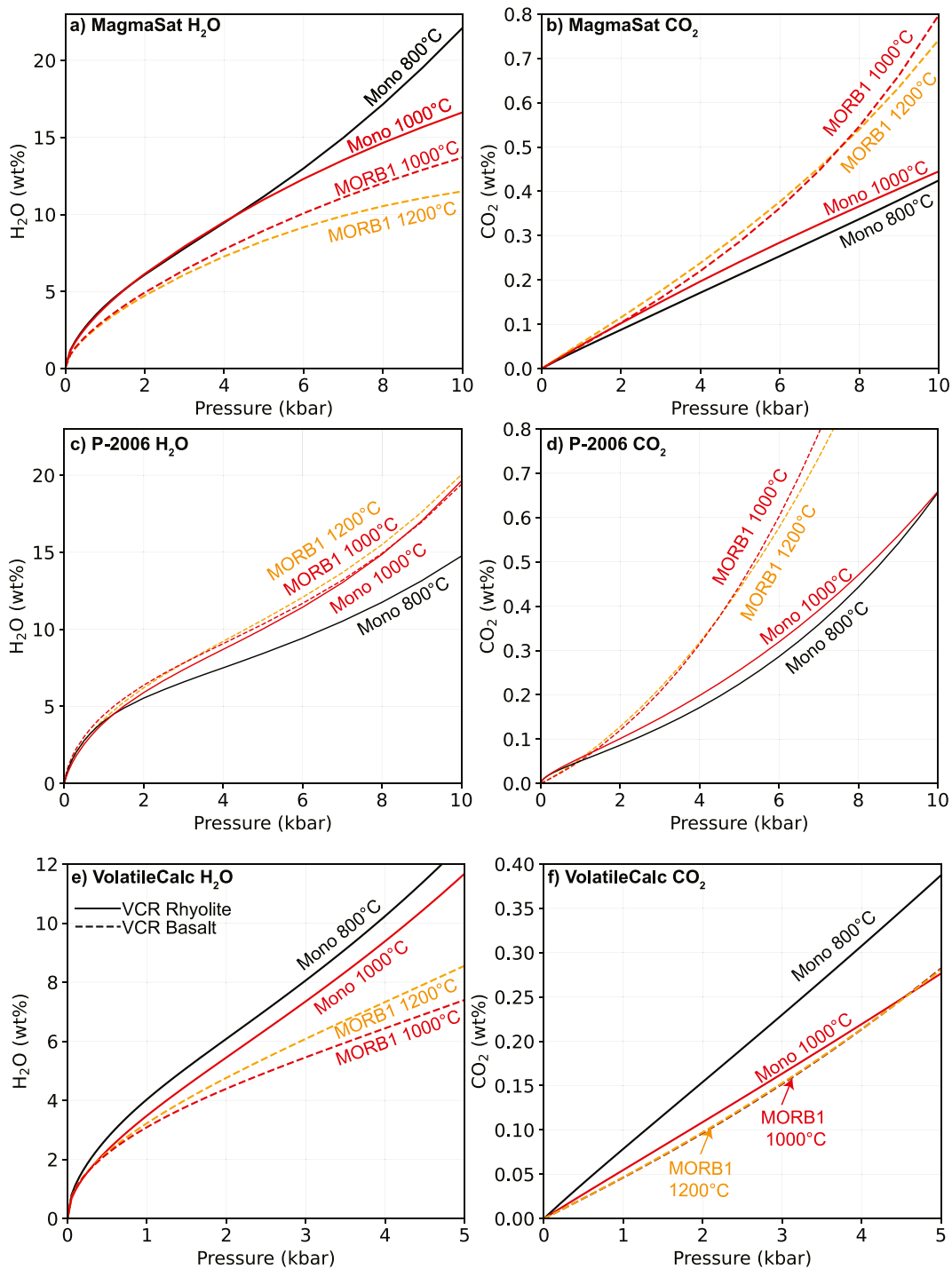


Figure 10. Comparison of solubility of basalt (represented by MORB1) to rhyolite (represented by Mono Craters) using MagmaSat (a) and (b), P-2006 (c) and (d), and VolatileCalc-Basalt and Rhyolite (e) and (f). Solubility curves are calculated for 1,200°C and 1,000°C for basalt, and 1,000°C and 800°C for rhyolite.

difference in solubility between basalts and rhyolites in each model are easily overwhelmed by differences in predictions from different solubility models. These discrepancies are enhanced by the different sensitivities of these models to temperature (see Section 5.3). Thus, careful selection of a suitable model is vital to quantify changes in solubility during magmatic differentiation.

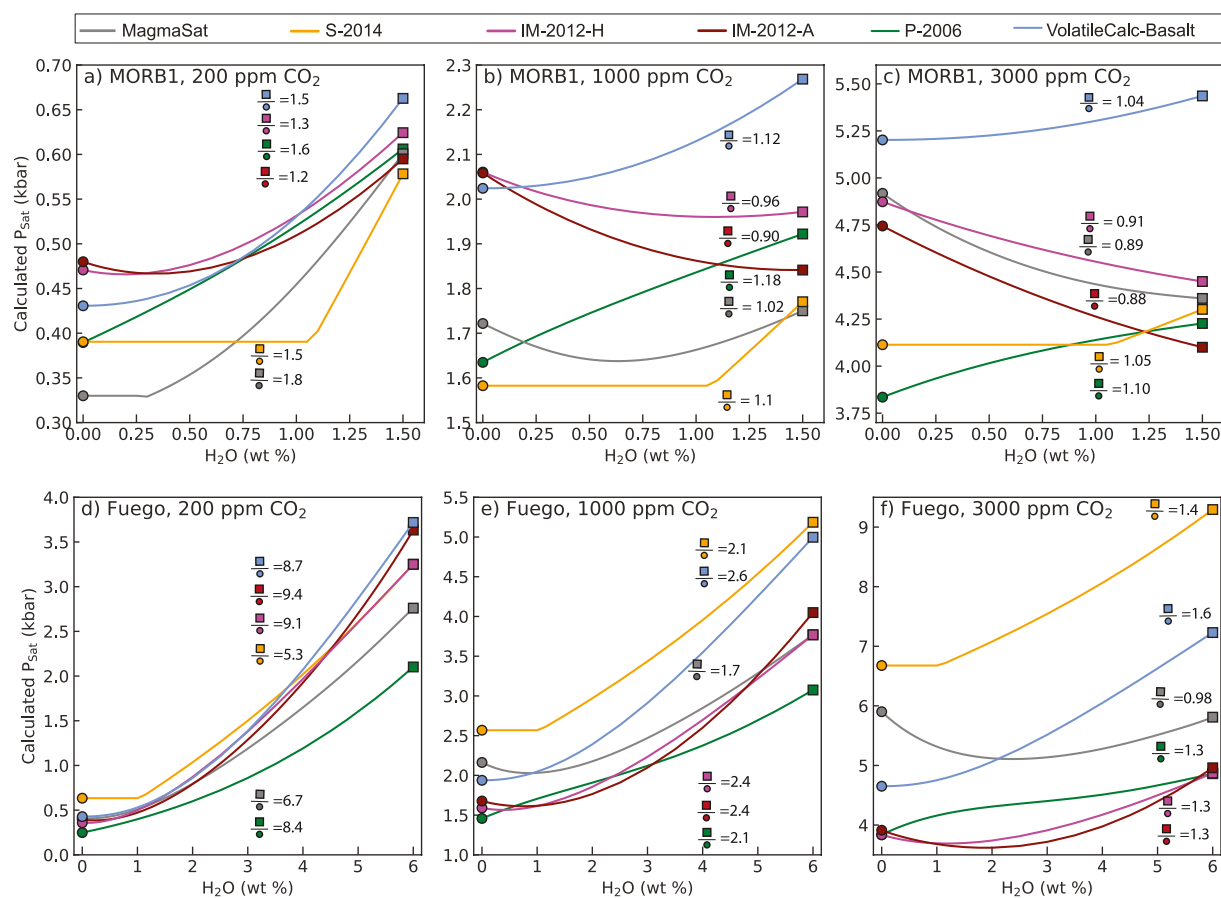


Figure 11. (a–c) Relationship between saturation pressure and melt H_2O content for H_2O -poor melts (using the MORB1 composition at 1,200°C). Three different melt CO_2 contents (200, 1,000, and 3,000 ppm) are shown in part (a–c), respectively. The numbers on the graphs show the saturation pressure at 1.5 wt% H_2O (square symbol) divided by the saturation pressure at 0 wt% H_2O for each model. (d–f) Sensitivity tests using the composition of a Fuego melt inclusion (Table 1) at 1,000°C, and H_2O contents between 0 and 6 wt%. Note that the y scale for (a–c) is significantly smaller than (d–f).

5. Model Sensitivities

In this section, we explore the sensitivity of the different models to parameters such as temperature and variable proportions of H_2O and CO_2 . Specifically, we consider how these inputs affect calculations of the pressure at which a melt inclusion was trapped (termed the saturation pressure). To calculate saturation pressures, the initial concentration of major and volatile elements as well as the temperature must be estimated at the time of melt inclusion entrapment. However, a number of processes, such as crystallization of the host mineral on the wall of the inclusion (termed post-entrapment crystallization or PEC), growth of a vapor bubble or daughter phases within the inclusion, and diffusive re-equilibration with a changing carrier liquid composition can make it difficult to reconstruct initial major element and volatile contents (Lowenstern, 1995). Similarly, diffusive re-equilibration of the major elements in the melt inclusion and host mineral, as well as the errors associated with mineral–melt and melt-only thermometers, can lead to uncertainties in the entrapment temperature, which propagates into the saturation pressure. By investigating the effect of varying these parameters within realistic limits, insight can be gained into the uncertainties associated with estimating magma storage depths using melt inclusions.

5.1. Relationship Between Saturation Pressure and Dissolved H_2O Content

Melt inclusion H_2O contents are vulnerable to diffusional re-equilibration with the melt surrounding the crystal (here termed the carrier melt), because of the fast diffusion rate of H^+ through silicate minerals (Portnyagin et al., 2008). H^+ diffusion is particularly fast in olivine (Gaetani et al., 2012), with melt inclusions losing signif-

icant amounts of water in hours to days (Bucholz et al., 2013). Thus, this discussion focuses on mafic compositions, where olivine-hosted melt inclusions are frequently analyzed.

In relatively H_2O -poor mafic systems such as MORs and ocean islands (e.g., Hawai'i, Iceland), diffusive re-equilibration can increase melt inclusion H_2O contents if crystals are mixed into more H_2O -rich carrier melts (Hartley et al., 2015), or, more commonly, cause melt inclusion H_2O contents to drop if the crystal is in contact with a carrier melt that has degassed its H_2O upon eruption (Bucholz et al., 2013; Gaetani et al., 2012). To assess how uncertainty in initial H_2O contents translates into errors on saturation pressures, we calculate saturation pressures for the MORB1 melt composition with 200, 1,000, and 3,000 ppm CO_2 (representing melt inclusions trapped at low, medium, and high pressures) for H_2O contents between 0 and 1.5 wt% (Figures 11a–11c). CO_2 contents are held constant while H_2O contents are varied, simulating the changes undergone by melt inclusions during diffusive re-equilibration (which strongly affects H_2O contents in the inclusion, but does not change the total CO_2 budget of the inclusion).

The relationship between saturation pressure and dissolved H_2O predicted by each solubility model is strongly dependent on the amount of CO_2 in the melt, and therefore the pressure. To quantify model sensitivity to H_2O , saturation pressures calculated at $\text{H}_2\text{O} = 1.5$ wt% are divided by the saturation pressure calculated at $\text{H}_2\text{O} = 0$ wt%, representing the possible discrepancy between the calculated saturation pressure and the real saturation pressure for melt inclusions which have undergone complete H^+ re-equilibration with a fully degassed erupted melt at 0 bar. At low pressures (200 ppm CO_2), all models show a decrease in calculated saturation pressure with decreasing H_2O contents, with entrapment pressures being 1.2–1.8× higher before complete H_2O -loss (Figure 11a). MagmaSat shows the strongest sensitivity to H_2O content, and both IM-2012 models the weakest.

At moderate pressures (1,000 ppm CO_2), loss of H_2O causes a significantly smaller decrease in saturation pressure for VolatileCalc-Basalt, P-2006 and S-2014 compared to the 200 ppm CO_2 scenario (Figure 11b; 1.1–1.2×). Saturation pressures for 1,000 ppm CO_2 calculated using MagmaSat and IM-2012-H first decrease, then increase with H_2O loss. This is because these models predict that the maximum CO_2 solubility occurs at H_2O contents at ~0.5 to 1.25 wt% (see Figure 6).

At higher pressures (3,000 ppm CO_2), saturation pressures from VolatileCalc-Basalt, P-2006 and S-2014 only drop by ~5% to 10% with progressive H_2O -loss, while saturation pressures continually increase with progressive H_2O -loss for IM-2012-H and -A and MagmaSat (because these models predict that maximum CO_2 solubility is found at H_2O contents >1.5 wt% at these pressures; Figure 6).

Within a given suite of MORB or OIB melt inclusions, the range of measured H_2O contents, and the uncertainty involved in reconstructing initial H_2O contents following diffusional re-equilibration, is likely significantly smaller than the 1.5 wt% H_2O considered here (Koleszar et al., 2009; Sides et al., 2014a; Wieser et al., 2021). Thus, except at low pressures (<1 kbar), uncertainties in saturation pressures due to diffusive re-equilibration of H_2O in relatively anhydrous systems are likely comparable to the analytical errors associated with the measurements of volatile species by FTIR or SIMS (±5%–10%), errors on each solubility model (~10% to 20%), and significantly smaller than the systematic differences between solubility models.

The higher H_2O contents of melt inclusions from subduction zones (~2 to 6 wt%; Plank et al., 2013) mean that substantially more H_2O can be lost following diffusive re-equilibration with a degassed carrier melt upon eruption. Additionally, arc melt inclusions are vulnerable to diffusive re-equilibration during crustal storage. This is because these relatively hydrous magmas saturate in a H_2O -rich fluid at high pressures in the crust. Thus, as a melt and its crystal cargo ascends from a deeper storage reservoir to a shallower storage reservoir, significant quantities of H_2O will be degassed and the H_2O contents of melt inclusions will rapidly diffusively re-equilibrate with the new carrier melt composition (Gaetani et al., 2012). Even if samples are rapidly quenched upon eruption (preventing syn-eruptive H_2O diffusion), only the volatile contents of melt inclusions trapped in the shallowest storage reservoir can be reliably converted into saturation pressures (Gaetani et al., 2012). This contrasts with more H_2O -poor systems such as mid-oceanic ridges and oceanic islands, where H_2O only degasses in the upper few 100 m of the crust, so ascent to a shallower reservoir is not accompanied by a drop in melt H_2O contents (although diffusive re-equilibration could occur if the resident melts in the shallower reservoir have different H_2O contents; Hartley et al., 2015).

To investigate the effect of H_2O re-equilibration on melt inclusion saturation pressures in arcs, we repeat the sensitivity test described above, using the major element composition of a Fuego melt inclusion with 49.7 wt% SiO_2

from Lloyd et al. (2013; Table 1) and H_2O contents between 0 and 6 wt% (Figures 11d–11f). For melt inclusions with 200 ppm CO_2 , complete diffusive loss of H_2O may result in saturation pressures being underestimated by a factor of ~ 5 to 10 \times . Even for melts with 3,000 ppm CO_2 (the highest pressure regime examined, and thus the best case scenario), diffusive loss can affect saturation pressures by factors of 0.98–1.6 \times (similar in magnitude to the sensitivity displayed by H_2O -poor melts at the lowest pressures; Figure 11a vs. Figure 11f). Only saturation pressures calculated in MagmaSat for the most CO_2 -rich melts display variations with variable H_2O -loss similar in magnitude to analytical errors. Thus, it is extremely important to determine whether melt inclusions have undergone H_2O -loss during ascent to a shallower reservoir or syn-eruptive degassing before using saturation pressures to deduce magma storage depths in H_2O -rich volcanic systems. If the initial H_2O content is uncertain, sensitivity tests like those performed here can be used to determine the possible range of saturation pressures.

5.2. Relationship Between Saturation Pressure and Dissolved CO_2 Content

Estimating the initial CO_2 contents of melt inclusions is also challenging. While the total CO_2 content of the inclusion is not affected by diffusive re-equilibration, CO_2 may be partitioned from the melt phase into a vapor bubble. Cooling following melt inclusion entrapment is accompanied by the formation of a denser mineral phase from a less dense silicate melt, and differential thermal contraction of the melt and crystal. These processes cause the internal pressure of the inclusion to drop (MacLennan, 2017; Steele-Macinnis et al., 2011), driving the nucleation and growth of a vapor bubble. This may be enhanced by the diffusive loss of H_2O , which also causes a pressure drop in the melt inclusion because of the high molar volume but low molecular weight of H_2O (Aster et al., 2016; Gaetani et al., 2012). A drop in pressure, combined with a decrease in the solubility of CO_2 in the melt phase because of changes to the major element composition accompanying PEC, causes CO_2 to partition strongly into the vapor bubble (MacLennan, 2017; Moore et al., 2015; Steele-Macinnis et al., 2011; Wieser et al., 2021). A number of recent studies have quantified the amount of CO_2 in vapor bubbles using Raman Spectroscopy, and demonstrated that between 15% and 99% of the total CO_2 budget of the inclusion may be held within the vapor bubble (Allison et al., 2021; Hartley et al., 2014; Moore et al., 2015; Wieser et al., 2021). This means that a large proportion of literature melt inclusion data, which only measured the CO_2 content of the glass phase, may have significantly underestimated initial CO_2 contents (and therefore saturation pressures).

In relatively H_2O -poor systems such as Hawai‘i and Iceland, where melt inclusion CO_2 contents have the dominant control on saturation pressures (shown by the near horizontal slopes of most model isobars at low H_2O contents; Figure 6), it is readily apparent that saturation pressures will be significantly underestimated if a CO_2 -rich vapor bubble is not measured. In arcs, H_2O contents inferred from melt inclusions or mineral hygrometers are sometimes used to place first order constraints on saturation pressures (e.g., Blundy & Cashman, 2005; Goltz et al., 2020; Plank et al., 2013). However, even in very H_2O -rich melts, the non-vertical orientation of isobars at high H_2O contents indicates that CO_2 contents still have an important role in determining the saturation pressure (Figure 6). Additionally, only a very small number of studies have measured CO_2 in melt inclusion vapor bubbles from arc systems (Aster et al., 2016; Mironov et al., 2020; Moore et al., 2015; Venugopal et al., 2020). Thus, it is vital to determine the effect of CO_2 on saturation pressures in H_2O -rich systems.

Using a similar method to that for H_2O discussed above, we calculate saturation pressures for the composition of a Fuego melt inclusion from Lloyd et al. (2013) with varying CO_2 and H_2O contents. The mean melt inclusion glass CO_2 content from this melt inclusion suite was 340 ppm (range of 59–786 ppm). However, Raman analyses of vapor bubbles in the same sample set by Moore et al. (2015) reveals that 993–4,776 ppm of CO_2 has migrated from the glass phase into the vapor bubble following melt inclusion entrapment. Thus, we calculate saturation pressures for CO_2 contents between 0 and 5,000 ppm at 1,000°C for 2, 4, and 6 wt% H_2O , respectively (after Plank et al., 2013).

S-2014 is most sensitive to CO_2 content, and IM-2012-H and -A the least sensitive. With increasing H_2O , the change in saturation pressure with increasing CO_2 becomes smaller, but is still significant (Figure 12). For example, calculating a H_2O -only saturation pressure for a melt inclusion with $\text{H}_2\text{O} = 6$ wt% in MagmaSat would underestimate magma storage depths by a factor of 1.5 if the melt inclusion had 1,000 ppm CO_2 , and a factor of 3 if the inclusion had 5,000 ppm CO_2 . For a melt inclusion with 4 wt% H_2O , H_2O -only saturation pressures underestimate by a factor of ~ 2.2 for 1,000 ppm CO_2 , and 5.4 for 5,000 ppm CO_2 . These variations in saturation pressure overwhelm the other errors associated with melt inclusion barometry (e.g., uncertainty in crustal den-

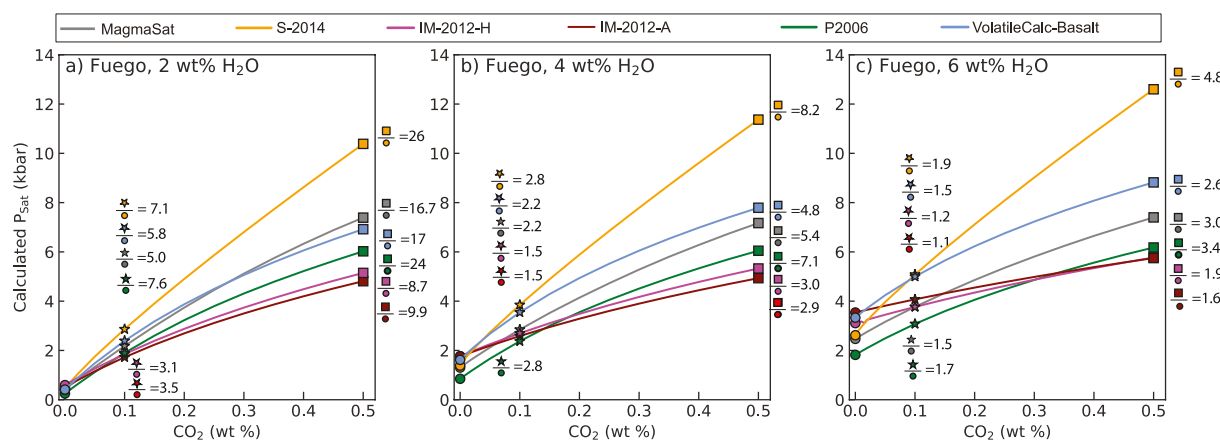


Figure 12. Relationship between saturation pressures and melt CO_2 contents for H_2O -rich melts (using the composition of a Fuego melt inclusion at 1000°C ; Table 1). Three different melt H_2O contents (2, 4 and 6 wt%) are shown in part a, b and c respectively. The numbers on the graphs show the saturation pressure at 5000 ppm CO_2 (square symbol) divided by the saturation pressure at 0 ppm CO_2 (circle), and the saturation pressure at 1000 ppm (star symbol) divided by the saturation pressure at 0 ppm CO_2 (circle) for each model.

sity profiles, analytical errors associated with volatile measurements by FTIR or SIMS, and differences between solubility models). Furthermore, investigation of the prevalence of CO_2 -rich vapor bubbles in arc lavas is clearly required to have confidence in published barometric estimates in studies which used mineral hygrometers, or did not measure melt inclusion vapor bubbles.

Saturation pressures in rhyolitic magmas are also very sensitive to melt CO_2 contents (Figure 13). For example, saturation pressures calculated for 1,000 ppm CO_2 versus 0 ppm CO_2 differ by factors of 5.7–8.8× for 2 wt% H_2O , and 1.6–2× for 6 wt% H_2O . Even saturation pressures calculated for 300 ppm CO_2 (0.03 wt%) versus 0 ppm CO_2 are a factor of ~2 to 3× higher for 2 wt% H_2O , and 1.2–1.3× higher for 6 wt% H_2O . The strong effect of CO_2 on saturation pressure is important to recognize when calculating saturation pressures using only melt H_2O contents, such as studies using mineral-melt hygrometers (Waters & Lange, 2013), or volatiles-by-difference methods to estimate H_2O contents of melt inclusions. It is also interesting to note that, to our knowledge, there are no published Raman measurements of CO_2 in vapor bubbles which grew after melt inclusion entrapment in dacitic-rhyolitic melt compositions. While the extremely low CO_2 contents of many rhyolitic melt inclusions are commonly interpreted to result from shallow crustal storage, it is becoming increasingly recognised that mafic melt inclusions with CO_2 below detection limit contain large quantities of CO_2 in the vapor bubble (Wieser et al., 2021). Thus, examination of vapor bubbles in melt inclusions from more silicic systems (e.g., Figure 1 of

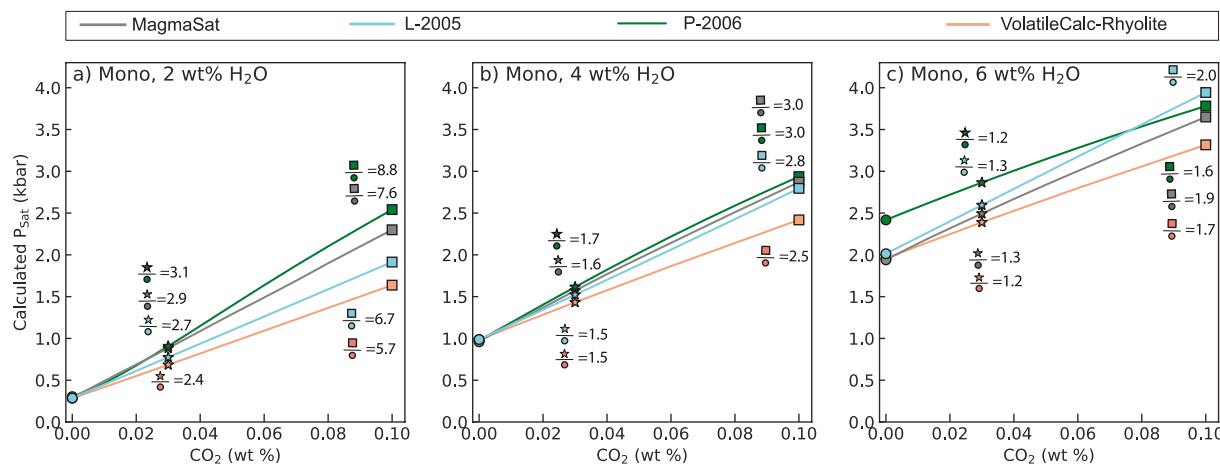


Figure 13. Sensitivity of saturation pressures to melt CO_2 contents at three different H_2O contents (2, 4, and 6 wt%) for the Mono Craters rhyolite. Ratios of saturation pressures at 0.03 wt% CO_2 (300 ppm; star symbol) versus 0 wt% (circle), and 0.1 wt% (1000 ppm; square symbol) versus 0 wt% CO_2 are shown on the figure.

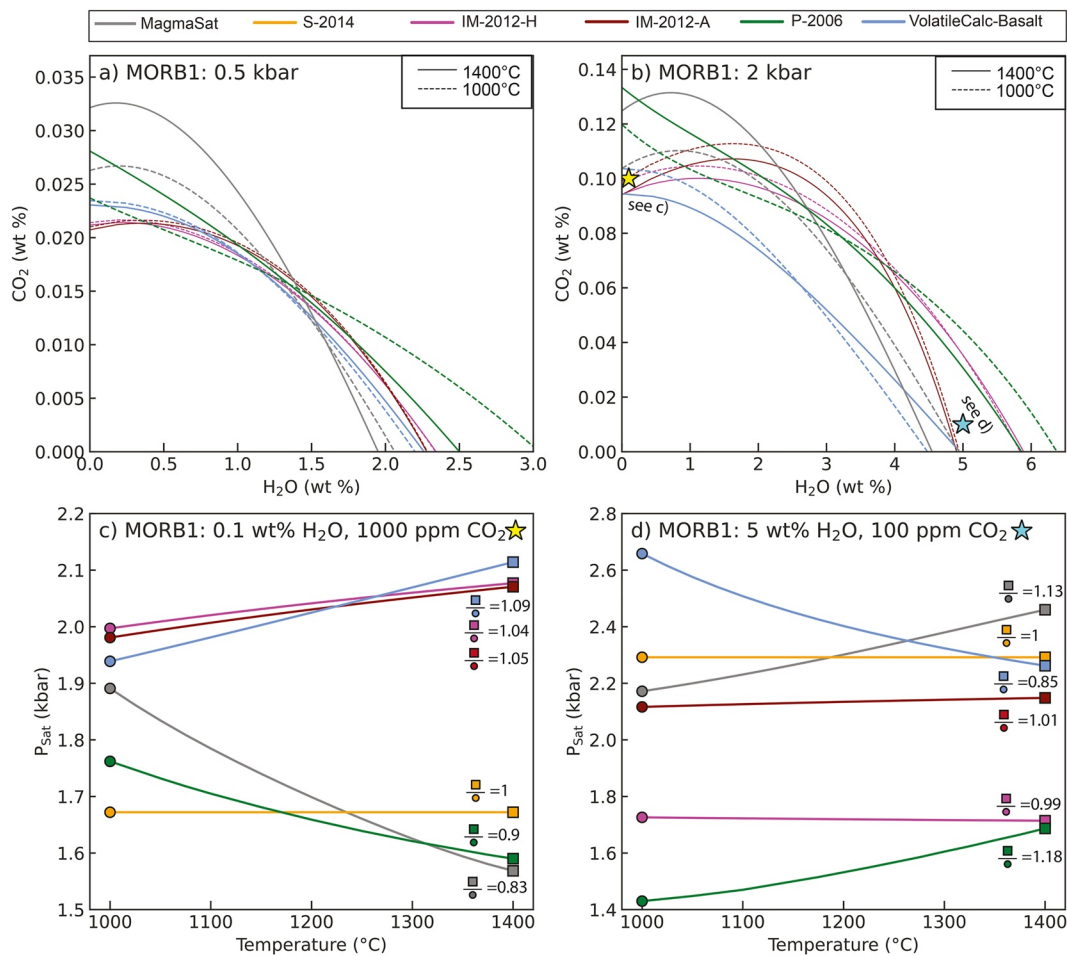


Figure 14. Evaluating model sensitivity to temperature (using the MORB1 composition). (a–b) Isobars evaluated at 1000 and 1400°C and 0.5 and 2 kbar. (c) Relationship between saturation pressure and temperature for a melt with 1000 ppm CO₂, 0.1 wt% H₂O (yellow star on a), (d) 100 ppm CO₂, 5 wt% H₂O (cyan star on b). Ratios of saturation pressures at 1400°C (square symbol) to 1000°C (circle symbol) are shown on the figure.

Lowenstern, 2001) is likely warranted, to rule out the possibility that these melts crystallized at greater depths than calculated using measurements of CO₂ hosted in just the glass phase.

5.3. Sensitivity to Temperature

The temperature of the melt at the time of entrapment is another source of uncertainty when calculating saturation pressures, as melt or mineral-melt thermometers are relatively imprecise. For example, the liquid MgO thermometer presented in Equation 13 of Putirka (2008) has a standard error of $\pm 71^\circ\text{C}$, while their clinopyroxene-liquid thermometer (Equation 28b) has a standard error of $\pm 48^\circ\text{C}$. Changes in the major element compositions of the melt inclusion during PEC and diffusive H₂O-loss can also introduce errors when estimating entrapment temperatures (as most thermometers are highly sensitive to the MgO and H₂O content of the melt). Additionally, almost all solubility experiments are performed at supra-liquidus conditions, while melt inclusion formation must take place at sub-liquidus conditions, so extrapolation to lower temperatures is an unfortunate necessity.

To investigate the sensitivity of different models to temperature, we calculate the 0.5 and 2 kbar isobars for the MORB1 composition at 1,000°C and 1400°C. Only S-2014 shows no temperature dependency, because there is neither a temperature or fugacity term in their equations. Interestingly, there is considerable disagreement between the other models as to whether a hotter magma dissolves more or less volatiles. MagmaSat and P-2006 predict an increase in pure CO₂ solubility with increasing temperature, while VolatileCalc-Basalt and IM-2012-A

and -H predict a much smaller decrease (Figures 14a–14c). In all models but IM-2012-A, isobars calculated for lower temperatures intercept the x -axis ($\text{CO}_2 = 0$ wt%) at higher H_2O contents, so the temperature dependency of H_2O solubility is opposite to that for CO_2 solubility. To visualize the effect of these trends on calculated saturation pressures for the MORB1 composition, the calculated saturation pressures for melts with volatile contents represented by the yellow and cyan stars on Figure 14b are plotted against temperature (between 1,000 and 1,400°C; Figures 14c and 14d). MagmaSat and P-2006 show the strongest temperature sensitivity, with a slope opposite to that of the more subtle changes predicted by VolatileCalc-Basalt and IM-2012.

The lack of consensus as to whether increasing temperature increases or decreases the solubility of H_2O and CO_2 indicates that this effect is relatively subtle, and overwhelmed by analytical errors associated with measuring experimental products (and other sources of experimental scatter; e.g., Figures 16a and 16b). This makes it very difficult for empirical models to fully constrain the temperature sensitivity, particularly given that the experiments conducted by any given study are usually performed at a single temperature. For example, all the experiments used to calibrate the VolatileCalc-Basalt model were conducted at 1,200°C, so the temperature dependency of this model results from the fugacity function, and $1/T$ terms from Dixon et al. (1995), rather than experimental observations.

IM-2012 is calibrated on experiments mostly performed at 1,200–1300°C (with a few spanning 1,100–1400°C). Their empirical expressions contain $\text{C}_{\text{H}_2\text{O}} \times \frac{P}{T}$ and $\text{C}_{\text{CO}_2} \times \frac{P}{T}$ terms in their expressions for H_2O and CO_2 solubility, respectively (Equations 11 and 15), where $\text{C}_{\text{H}_2\text{O}}$ and C_{CO_2} are empirically derived constants, and P and T are pressure and temperature. In the hydrous model, $\text{C}_{\text{H}_2\text{O}}$ is negative (-0.02 ± 0.02), so H_2O solubility increases with increasing temperature, while in the anhydrous model $\text{C}_{\text{H}_2\text{O}}$ is positive (0.02 ± 0.02), so H_2O solubility decreases with increasing temperature (Figure 14). As the absolute values of these coefficients are small, the temperature effect on H_2O solubility is small, and only visible at higher pressures (because of the P part of these terms; Figure 14a vs. Figure 14c). It is also worth noting that these coefficients in both models are within error of zero, showing that the experimental dataset used to calibrate this model showed very little evidence for a change in H_2O solubility with temperature. In both the hydrous and anhydrous models, C_{CO_2} is positive (0.12 ± 0.02 and 0.14 ± 0.02 , respectively), and larger in magnitude than $\text{C}_{\text{H}_2\text{O}}$, so CO_2 solubility decreases with increasing temperature (see Figure 14c).

The approach taken by S-2014 and A-2019 is an interesting alternative when constructing solubility models. While S-2014 is calibrated on experiments conducted between 1,200°C–1,300°C for CO_2 , and 1,200°C–1,250°C for H_2O , their solubility equations contain no temperature or fugacity term. Instead, these authors suggest that the H_2O model should ideally be used between 1,150 and 1,250°C. They perform additional tests on experiments between 1050°C and 1,400°C not used in the calibration, and show that their model predicts H_2O solubility within $\pm 10\%$ for 78% of experiments for this wider temperature range. The S-2014 testing dataset for CO_2 only has a slightly different temperature range than the calibration dataset (1,170°C–1,250°C vs. 1,200°C–1,250°C), so they do not suggest an expanded temperature range for CO_2 . Similarly, the spreadsheet for A-2019 (and the implementation of this model in VESIcal) performs all calculations at 1,200°C, regardless of the user-input temperature. Allison et al. (2019) suggest that this approach is likely valid between 1,000°C and 1,400°C.

Unlike empirical models, the temperature sensitivity of P-2006 and MagmaSat arises from the entropy differences between melt and fluid components. Given the limited experimental evidence for changes in solubility with temperature, the directionality inferred by thermodynamical models is more likely to be correct, as the relative entropy differences between components are easier to constrain than deconvoluting subtle differences between the solubility of CO_2 and H_2O in experiments run at different temperatures, and because all empirical models are being extrapolated to lower temperatures than the supra-liquidus experiments used to calibrate them. However, the fact that P-2006 does not account for volatile speciation for either H_2O or CO_2 , and MagmaSat does not account for the two H_2O species in the melt means that these thermodynamic temperature sensitivities may also need further interrogation.

Overall, although the differences between models is interesting, and important to recognize when extrapolating beyond the range of the calibration dataset, the uncertainty that temperature variations introduce to saturation pressure calculations are relatively small for mafic melts. For example, an uncertainty in the initial entrapment temperature of $\pm 100^\circ\text{C}$ introduces an uncertainty similar to that associated with in-situ measurements of melt inclusion volatile contents ($\pm 5\%–10\%$; Figure 14).

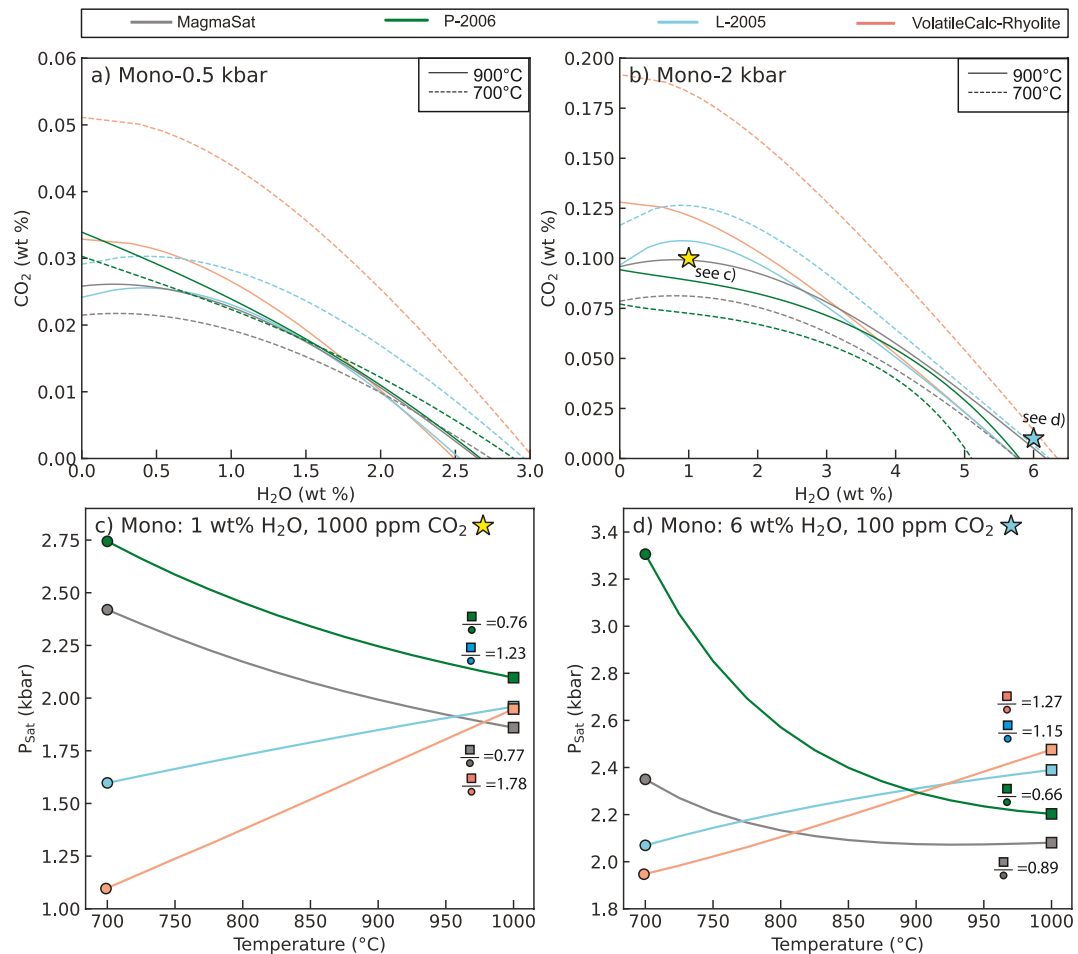


Figure 15. Sensitivity of saturation pressures for the Mono Craters rhyolite to temperature. (a) and (b) Isobars calculated for different solubility models at 700°C and 900°C and 0.5 and 2 kbar. (c) Relationship between saturation pressure and temperature for a melt with 1,000 ppm CO₂, 1 wt% H₂O [yellow star in (b)]. (d) 100 ppm CO₂, 6 wt% H₂O [cyan star in (b)]. Ratios of saturation pressures at 1000°C (square symbol) to 700°C (circle symbol) are shown on the figure.

Temperature sensitivity in rhyolitic melts was evaluated by calculating isobars at 0.5 and 2 kbar for 700°C and 900°C using the Mono Craters rhyolite composition. As for the basaltic example, the directionality and magnitude of effect of temperature on saturation pressures for melts with volatile contents indicated by the colored stars is shown in Figures 15c and 15d for temperatures between 700°C and 1,000°C. VolatileCalc-Rhyolite shows the strongest temperature sensitivity, predicting that the solubility of CO₂ decreases with increasing temperature. L-2005 also predicts decreasing CO₂ solubility with increasing temperature, although this effect is smaller than for VolatileCalc-Rhyolite. Decreasing solubility of molecular CO₂ with increasing temperature was demonstrated experimentally by Fogel and Rutherford (1990). In contrast, the two thermodynamic models, P-2006 and MagmaSat, predict that pure CO₂ solubility increases with increasing temperature. VolatileCalc-Rhyolite also predicts that H₂O solubility decreases with increasing temperature, but the effect is smaller than for CO₂.

It is noteworthy that the temperature sensitivity of CO₂ solubility predicted by L-2005 and VolatileCalc-Rhyolite is much greater than that shown by any of the basaltic models (Figures 14d and 14e vs. Figures 15d and 15e), and significant considering other sources of error associated with saturation pressure calculations. MagmaSat and P-2006 also show a far greater sensitivity to H₂O solubility between 700–850°C in rhyolites than any of the basaltic models between 1,000–1400°C (Figure 14f vs. Figure 15f), although the sensitivity decreases between 800–900°C.

Given the contrasting behavior of empirical and thermodynamic models, and the relatively strong effect of temperature in rhyolitic melts, we suggest that users proceed with caution when extrapolating empirical models to

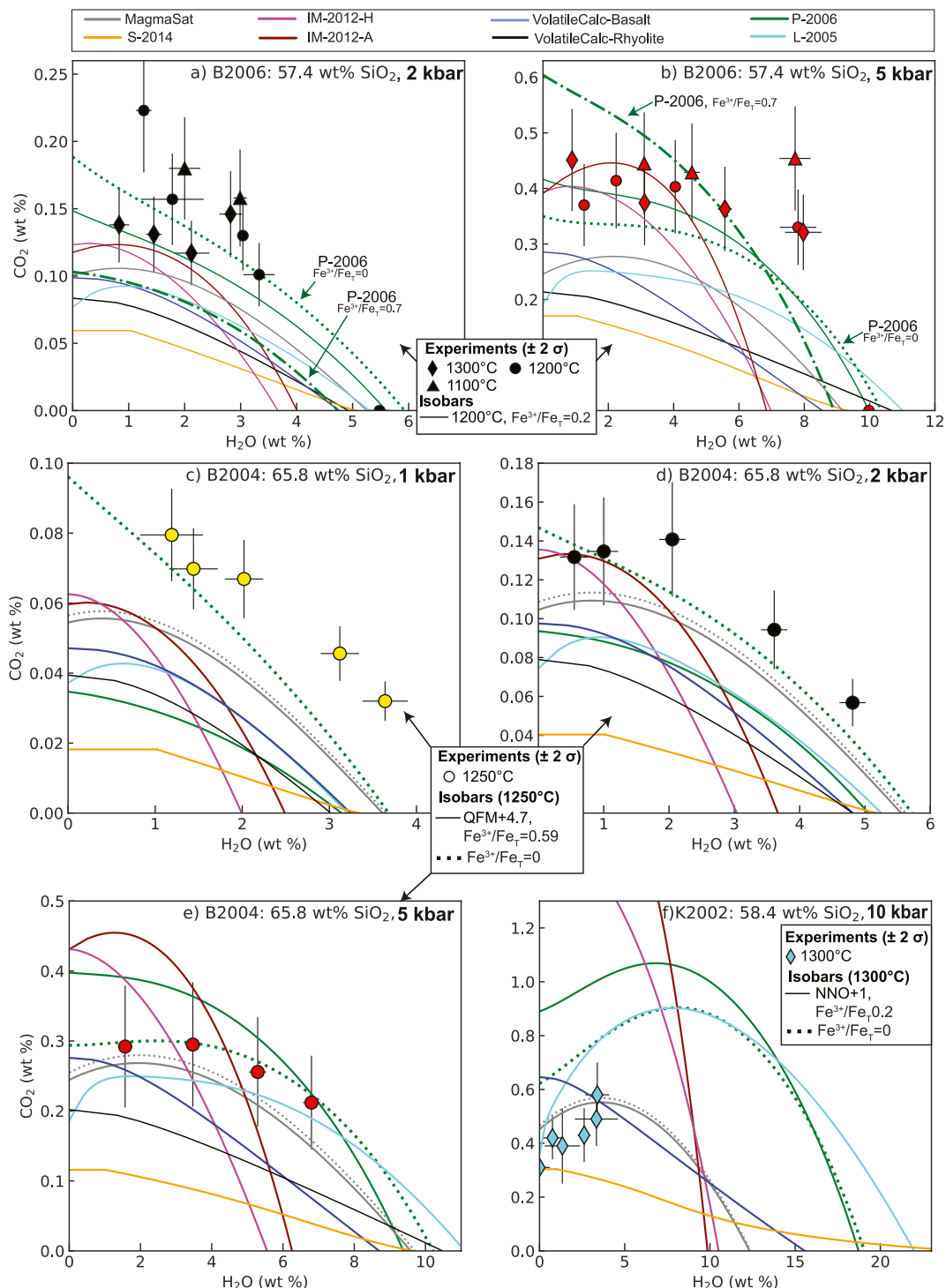


Figure 16. Assessing model fits to experimental data for andesitic and dacitic compositions (a) and (b) Experiments from Botcharnikov et al. (2006). Isobars were calculated for $1,200^\circ\text{C}$ and $\text{Fe}^{3+}/\text{Fe}_T = 0.2$ ($\sim \text{QFM} + 1.5$). P-2006 isobars are also shown for $\text{Fe}^{3+}/\text{Fe}_T = 0.7$ (the upper estimate of $\text{Fe}^{3+}/\text{Fe}_T$ in experimental products; dash-dotted line), and $\text{Fe}^{3+}/\text{Fe}_T = 0$ (dotted line) (c)–(e) Experiments from Behrens et al. (2004). Isobars are shown for $\text{Fe}^{3+}/\text{Fe}_T = 0.59$ (fO_2 of QFM + 4.7). For P-2006 and MagmaSat, isobars are also shown for $\text{Fe}^{3+}/\text{Fe}_T = 0$. (f) Experiments from King and Holloway (2002). Isobars are shown for $\text{Fe}^{3+}/\text{Fe}_T = 0.2$. For P-2006 and MagmaSat, isobars are also shown for $\text{Fe}^{3+}/\text{Fe}_T = 0$. VolatileCalc-Rhyolite isobars are not shown, as the spreadsheet does not calculate isobars above 5 kbar. Error bars on all plots shows the 2σ uncertainties from measurements of volatile contents in experimental products. $\text{Fe}^{3+}/\text{Fe}_T$ ratios were calculated from author-stated buffers using MELTS for Excel (Gualda & Ghiorso, 2015).

temperatures significantly lower or higher than the calibration temperature of each model. It may be best to use empirical models at the calibration temperature (e.g., 1,200°C for VolatileCalc-Basalt and 850°C for Volatile-Calc-Rhyolite), which is the approach used by in the models of S-2014 and A-2019, rather than introduce a temperature sensitivity with the wrong sign. This is discussed in further detail for VolatileCalc-Rhyolite in Section 6.

6. Intermediate Compositions

In this section, we compare the predictions of different solubility models for intermediate melt compositions (andesites to dacites). Lavas with these compositions are dominant within subduction zones, and volcanoes erupting these compositions are extremely hazardous. Yet, there is a notable paucity of solubility experiments for andesitic and dacitic compositions relative to basalts and rhyolites (Figure 2; Botcharnikov et al., 2006; King & Holloway, 2002). This section builds on the sensitivity tests performed in Section 5 to evaluate possible discrepancies between model outputs and experimental constraints.

The calibration dataset of MagmaSat has the broadest coverage of andesitic-dacitic compositions of all the models described here (although it is far from extensive). While there are a number of pure H₂O experiments, MagmaSat only includes one pure CO₂ experiment on an andesitic melt (conducted at 1 GPa; King & Holloway, 2002), and no pure CO₂ experiments on dacitic melts. Similarly for mixed H₂O-CO₂, the calibration dataset for andesitic melts includes only 4 experiments from King and Holloway (2002), 21 from Botcharnikov et al. (2006), and 3 from Botcharnikov et al. (2007). Dacitic liquids are represented by the 12 experiments on mixed H₂O-CO₂ solubility by Behrens et al. (2004). As the P-2006 model had a decade fewer experimental constraints available for calibration, it only includes the one pure CO₂ and four mixed H₂O-CO₂ andesitic experiments of King and Holloway (2002). The IM-2012 model includes two pure H₂O experiments that lie within the andesite field on a TAS diagram, but no H₂O-CO₂ experiments, and no experiments in the dacitic field. None of the other models contain any andesitic or dacitic melts in their calibration datasets.

6.1. Comparing Solubility Models to Experimental Products

The suitability of different solubility models for andesitic-dacitic compositions can be evaluated by calculating isobars using the melt compositions, pressures, and temperatures of different experimental studies, and comparing these isobars to measurements of dissolved volatile contents in experimental products (similar to the method used in the supplementary material of Ghiorso & Gualda, 2015). The 2 and 5 kbar andesitic experiments of Botcharnikov et al. (2006) are shown in Figures 16a and 16b, the 1, 2, and 5 kbar dacitic experiments of Behrens et al. (2004) are shown in Figures 16c–16e, and the 10 kbar andesite experiments of King and Holloway (2002) are shown in Figure 16f. Additional isobar diagrams for the 3–12 kbar basaltic-andesite experiments of Mangan et al. (2021) are shown in the Supporting Information.

These isobar diagrams show that S-2014 significantly underpredicts CO₂ solubility for all experiments except the most H₂O-poor composition of King and Holloway (2002). L-2005, VolatileCalc-Basalt, and -Rhyolite also mostly plot to lower CO₂ contents than experimental products (Figure 16). IM-2012-H and -A do a reasonable job of recreating the most H₂O-poor experiments at <5 kbar, but curve rapidly down to intercept the x-axis at lower H₂O contents than experimental products and other models. MagmaSat is a good match to experimental data in Figures 16d–16f, but plots to lower CO₂ contents than experiments in Figures 16a–16c. Using Fe³⁺ proportions best representing the experimental conditions, P-2006 only passes through experimental data on Figures 16a, 16b, and 16e, and plots to significantly lower CO₂ contents than experiments (lower than MagmaSat) on Figures 16c and 16d. P-2006 is a better match to most experiments if Fe³⁺/Fe_T = 0, but overpredicts CO₂ solubility at 10 kbar for all redox states. Interestingly, none of the available models recreate the near-flat trajectory of dissolved CO₂ contents with increasing H₂O from Botcharnikov et al. (2006).

The underprediction of CO₂ solubility by S-2014 is a good example of the dangers of extrapolating models accounting for the effect of melt composition using empirical expressions beyond the compositional range of the calibration dataset. The S-2014 model expresses CO₂ solubility as a function of the composition parameter, Π^* , with CO₂ solubility increasing as an exponential function of Π^* at a given pressure (Equation 16). The melt compositions for the three sets of experimental studies shown in Figure 16 all plot to much lower Π^* values than any of the melts in the calibration dataset (orange diamonds; Figure 17a). These low Π^* values mean that the S-2014

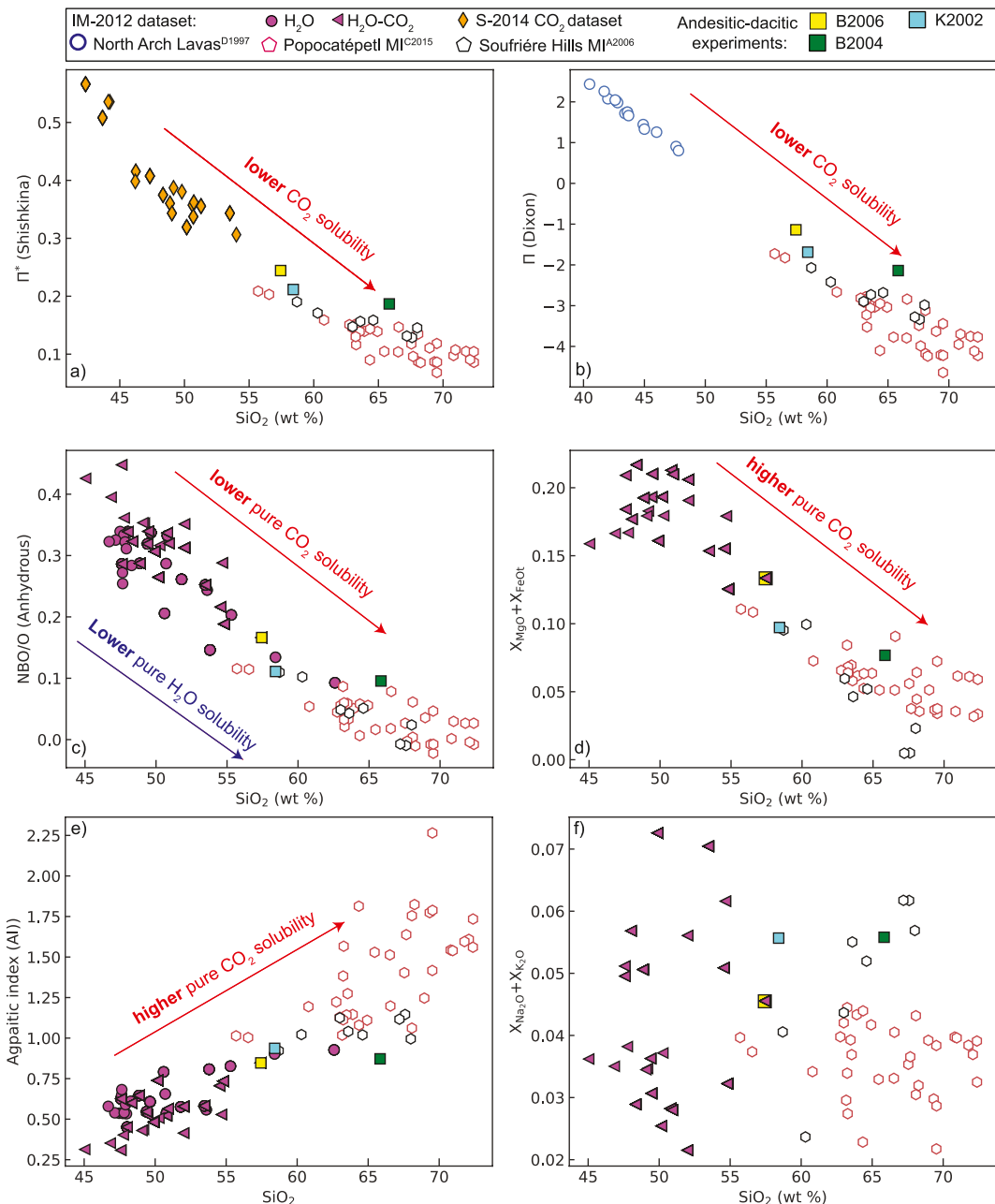


Figure 17. Comparing the calibration datasets of S-2014 and IM-2012 to the andesitic experiments of Botcharnikov et al. (2006; B2006), Behrens et al. (2004; B2004), and King and Holloway (2002; K2002) shown in Figure 16, and the melt inclusions from Popocatépetl (Atlas et al., 2006) and Soufrière Hills (Cassidy et al., 2015) shown in Figure 18. Anhydrous molar fractions are used to calculate compositional parameters in (c)–(f), because when accounting for discrepancies between isobars (e.g., on Figure 18, the H_2O content and therefore hydrous cation fractions vary as a function of the pressure).

model predicts very low CO_2 solubilities. However, CO_2 solubility for melts with Π^* values outside the range of the calibration dataset may not follow the same exponential function of this parameter as melt compositions within the calibration range. Additionally, the exponential dependency of CO_2 solubility on Π^* incorporated by S-2014 likely breaks down in more evolved melts, because Π^* represents the ability of the melt to form carbonate-bearing species, while more evolved melts contain increasing proportions of molecular CO_2 (Shishkina et al., 2014). For example, the proportion of molecular CO_2 to carbonate species varies between 0 and 4 wt% in the experiments of Botcharnikov et al. (2006) and 3–30 wt% in the dacitic experiments of Behrens et al. (2004).

VolatileCalc-Basalt and VolatileCalc-Rhyolite underpredict CO_2 solubility for all intermediate experiments, with VolatileCalc-Rhyolite predicting lower pure CO_2 solubility than VolatileCalc-Basalt. This underprediction is noteworthy, because many publications have calculated saturation pressures for andesitic and dacitic melts using VolatileCalc-Rhyolite (e.g., Atlas et al., 2006; Blundy et al., 2006; Cassidy et al., 2015; Koleszar et al., 2012). In the original publication, Newman and Lowenstern (2002) state: “because many andesites contain rhyolitic interstitial melt, VolatileCalc may also be applicable to these intermediate compositions.” However, this should not be taken to suggest that VolatileCalc-Rhyolite is safely extrapolated to andesitic-dacitic melts. Instead, this statement is referring to the fact that many lavas with andesitic bulk compositions have rhyolitic groundmass/melt inclusion compositions (e.g., Reubi & Blundy, 2009; Tamura & Tatsumi, 2002), where VolatileCalc-Rhyolite may be applicable. Interestingly, VolatileCalc-Rhyolite isobars calculated for the reference temperature of this model (850°C) rather than the experimental temperature are a good match to experimental data at <5 kbar (see Figure S3 in Supporting Information S1). Thus, the main failure of this model in intermediate compositions appears to result from the fact that this model is extremely sensitive to temperature, and these melts have much higher temperatures than the experiments used to calibrate this model. This supports our suggestion in Section 4.2.1 that it may be better run models at their reference temperature, rather than extrapolate beyond the calibration range.

It is also worth noting that all these experimental products have negative values of the Dixon Π parameter (Equation 2). As highlighted by Moore (2008), the full Π expression of Dixon (1997) cannot be used to calculate CO_2 solubility in calc-alkaline lavas, because Π is negative (yielding a negative solubility of CO_2 ; Figure 17).

Differences between experimental data and isobars from IM-2012-H and -A are more complicated, because the discrepancies between models and experiments are very dependent on the pressure. For example, at 1 kbar, IM-2012-H and -A underpredict H_2O and CO_2 solubility relative to the experiments of Behrens et al. (2004), while at 5 kbar, they overpredict CO_2 solubility, but underpredict H_2O solubility (Figure 16c vs. Figure 16e). These discrepancies likely reflect this model being extrapolated toward the limits of its calibration dataset in terms of both pressure (most experiments were conducted at <5 kbar) and melt composition (Figure 17, see the next section for more discussion).

The fact that no model passes through all available experiments demonstrates that further investigation of solubility in andesitic to dacitic melts is warranted. Using representative experimental $\text{Fe}^{3+}/\text{Fe}_T$ ratios, MagmaSat is the most accurate model, predicting dissolved volatile contents within ~20% of experimental products (considering reported error bars on dissolved volatile contents).

The extreme sensitivity to the $\text{Fe}^{3+}/\text{Fe}_T$ ratio makes it very difficult to assess the accuracy of the P-2006 model (particularly given the relatively large uncertainties in the oxygen fugacity of experimental run products; Botcharnikov et al., 2006; King & Holloway, 2002). In all of the examples shown, P-2006 isobars calculated for $\text{Fe}^{3+}/\text{Fe}_T = 0$ are a better fit to the experimental data than isobars calculated using estimates of the $\text{Fe}^{3+}/\text{Fe}_T$ ratio of experiments. This suggests that, in relatively oxidising intermediate melts, P-2006 is overestimating the effect of Fe^{3+} species on volatile solubility. It is noteworthy that P-2006 is a particularly poor match to the high pressure andesitic experiments of King and Holloway (2002), despite the fact that these are the only intermediate experiments in the calibration dataset of this model.

As all the experiments shown were used to calibrate MagmaSat, similar analysis applied to new experimental data on andesitic compositions when it becomes available will provide further constraints on the accuracy of this model. Isobars for recent solubility experiments on a basaltic-andesite at 4–12 kbar by Mangan et al. (2021) are shown in Figures S4 and S5 in Supporting Information S1. MagmaSat is a much better fit to this new data than P-2006, with experiments performed 400–815 MPa plotting within error of calculated MagmaSat isobars. In contrast, P-2006 overpredicts CO_2 solubility (regardless of $\text{Fe}^{3+}/\text{Fe}_T$) at <600 MPa.

6.2. Case Study: Intermediate Melt Inclusions

To assess the impact of these model differences on the depths of magma storage reservoirs inferred from melt inclusions in volcanic arcs, we calculate saturation pressures using a variety of models for two suites of melt inclusions with andesitic-dacitic liquid compositions: (a) 34 melt inclusions from Volcán Popocatépetl, Mexico with 55.7–73.4 wt% SiO_2 (Figures 2 and 18a; Atlas et al., 2006). (b) 8 melt inclusions from Soufrière Hills Volcano,

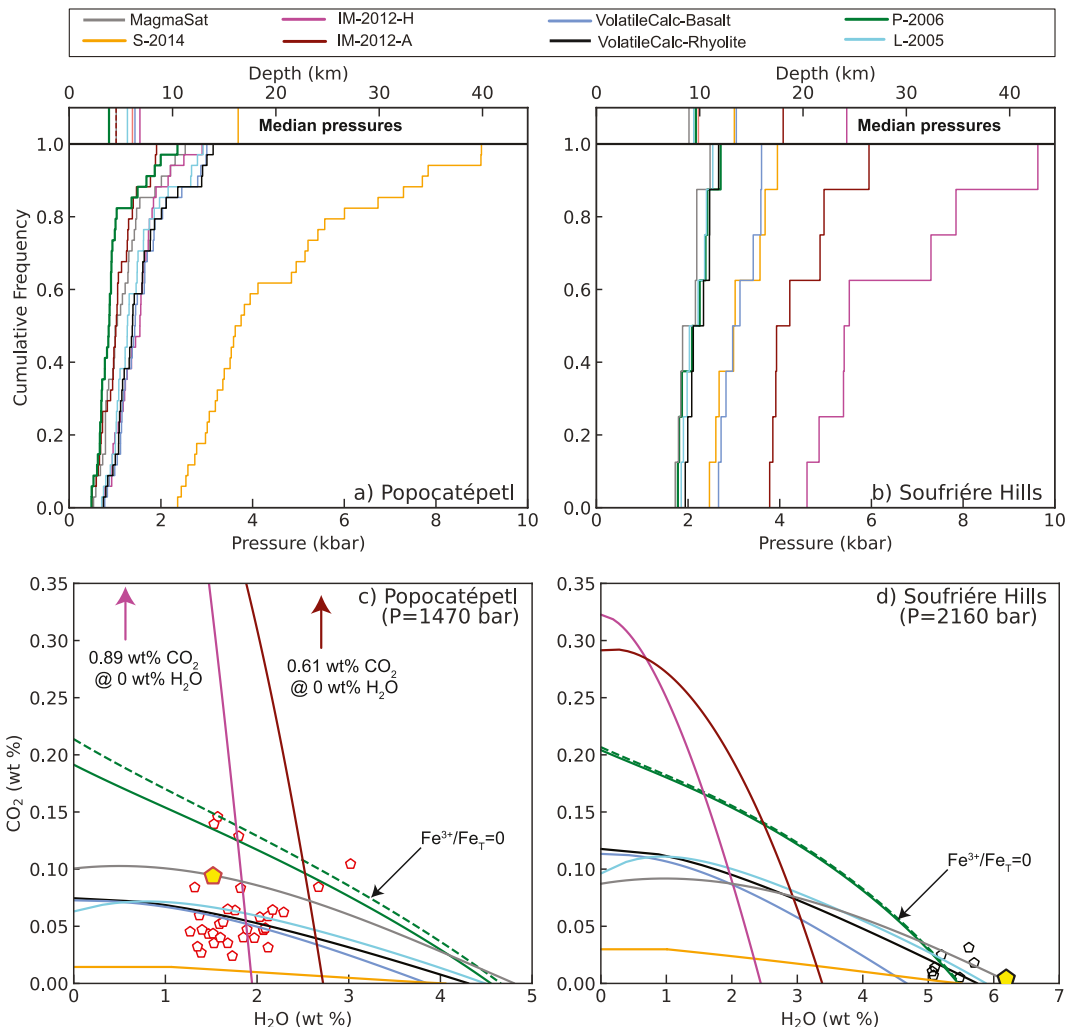


Figure 18. (a) and (b) Cumulative distribution functions of saturation pressures from different models for melt inclusions from (a) Popocatépetl (Atlas et al., 2006) and (b) Soufrière Hills (Cassidy et al., 2015). Fe^{3+}/Fe_T was set to 0.15. (c) Isobars from different models calculated at the saturation pressure from MagmaSat (1,470 bar) for the Popocatépetl melt inclusion shown with a yellow pentagon (at 1,050°C following Atlas et al., 2006). The scale is trimmed to emphasize the differences between models at lower CO₂ contents, with the interception of the IM-2012 isobars with the y-axis labeled on the plot. (d) Isobars from different models calculated at the saturation pressure from MagmaSat (2,160 bar) for the Soufrière Hills melt inclusion shown with a yellow pentagon (at 1,000°C following Cassidy et al., 2015). Isobars are also shown for P-2006 with Fe^{3+}/Fe_T = 0 (dotted line).

Montserrat with 58.7–68.0 wt% SiO₂ (Figures 2 and 18b; Cassidy et al., 2015). Both studies calculated saturation pressures (and therefore magma storage depths) using VolatileCalc-Rhyolite.

Cumulative frequency distributions for the Popocatépetl melt inclusions (Figure 18a) shows that P-2006 predicts the lowest saturation pressures, and S-2014 the highest, with MagmaSat, IM-2012-A, VolatileCalc-Basalt, VolatileCalc-Rhyolite, and IM-2012-H lying in-between these model extremes. Based on our analysis in the previous section suggesting that MagmaSat is the best calibrated model for intermediate melt compositions, we ratio saturation pressures from each model to those determined using MagmaSat (allowing model differences to be quantified). Additionally, because MagmaSat is a thermodynamic model that has been shown to work well for basaltic and rhyolitic compositions, it is effectively being interpolated to andesitic-dacitic compositions which are not represented in its calibration dataset (i.e., these melt inclusion compositions), rather than extrapolated (as for empirical models such as S-2014, VolatileCalc-Basalt, and IM-2012 which are primarily calibrated on more mafic melt compositions; Figure 2).

The median saturation pressure for Popocatépetl melt inclusions calculated for VolatileCalc-Rhyolite is 1.26× higher than for MagmaSat. The median for MagmaSat is ~1.2× higher than for P-2006. The deviation relative to MagmaSat increases with SiO_2 content for VolatileCalc-Rhyolite (~1.1 to 1.5×), VolatileCalc-Basalt (~1 to 1.35×), and L-2005 (~1 to 1.4×). The deviation between S-2014 and MagmaSat is very large, increasing from a factor of 2 at ~55 wt% SiO_2 to ~5.5× at 72.5 wt% SiO_2 . The presence of discrepancies which correlate with melt composition is particularly concerning, because it means that choice of an inappropriate solubility model may introduce systematic error into a dataset as a function of melt inclusion composition. In contrast, the deviation between IM-2012-H and -A and P-2006 versus MagmaSat shows no clear correlation with SiO_2 content (Figure S6 in Supporting Information [S1](#)).

MagmaSat predicts the lowest saturation pressures for the Soufrière Hills melt inclusions, with L-2005, P-2006, and VolatileCalc-Rhyolite predicting reasonably similar pressures (Figure [18b](#)). VolatileCalc-Basalt, S-2014, and IM-2012-A and -H are offset to higher pressures. Similar to the results for Popocatépetl, the ratio of saturation pressures for Soufrière Hills melt inclusions relative to MagmaSat for L-2005 (~1 to 1.1×), VolatileCalc-Basalt (~1.25 to 1.35×), and VolatileCalc-Rhyolite (~1.05 to 1.17×) increase with increasing SiO_2 (Figure S7 in Supporting Information [S1](#)). Unlike Popocatépetl melt inclusions, the discrepancy between IM-2012 and MagmaSat increases dramatically with increasing SiO_2 (from ~1.5 to 2.5× for anhydrous, and 2 to 4.5× for hydrous), while that for S-2014 shows a weak negative correlation with SiO_2 (from ~1.7 to 1.35×).

The large discrepancies shown by IM-2012 (for Soufrière Hills) and S-2014 (for Popocatépetl) are best understood by examining an isobar calculated for the inclusion showing the largest deviation relative to MagmaSat in each dataset ($\text{SiO}_2 = 72.4$ wt% for Popocatépetl and 67.6 wt% for Soufrière Hills; yellow pentagon on Figures [18c](#) and [18d](#)) at the saturation pressure obtained from MagmaSat. For both sets of inclusions, S-2014 isobars intercept the x -axis at similar H_2O contents to other models, but intercept the y axis at drastically lower CO_2 contents. This underestimation of CO_2 solubility likely results from the fact that the Π^* values of these inclusions lie well below that of the calibration dataset (as discussed for andesitic experiments; Figure [17b](#)).

In contrast, IM-2012 predicts very high pure CO_2 solubility, and low pure H_2O solubility relative to the other models. Both IM-2012 models express the compositional dependence of H_2O solubility in terms of the parameter NBO/O, with melts with higher NBO/O values having higher H_2O solubility (Equation [15](#)). Both sets of melt inclusions possess much lower NBO/O values than the calibration dataset of IM-2012 (Figures [17c](#) and [17d](#)). This is problematic, because the empirical relationship between NBO/O and pure H_2O solubility incorporated by IM-2012 has not been validated for these melt compositions. For example, Shishkina et al. (2014) show that IM-2012 drastically overestimates H_2O solubility in their basanite and nephelinite melt compositions. They point out that while IM-2012 conclude that there is only a small effect of melt composition on H_2O solubility, the IM-2012 model ends up showing a strong sensitivity to melt composition when extrapolated to the high NBO/O ratio in their basanite and nephelinite melts (and we invoke a similar explanation for the lower NBO/O ratios in melt inclusions discussed here).

The IM-2012 expression for CO_2 solubility is more complicated, containing terms for AI, NBO/O, $X_{\text{Na}_2\text{O}+\text{K}_2\text{O}}$, $X_{\text{FeO}+\text{MgO}}$, and $X_{\text{H}_2\text{O}}$ (Equation [11](#)). These two sets of melt inclusions have higher AI, lower NBO/O ratios, similar values of $X_{\text{Na}_2\text{O}+\text{K}_2\text{O}}$, and lower $X_{\text{FeO}+\text{MgO}}$ values than the calibration dataset (Figures [17d](#)–[17f](#)). While the effect of NBO/O is more convoluted because it also affects the solubility of H_2O (which feeds back into the expression for CO_2), it is readily apparent that the positive coefficient attached to the AI term combined with the negative coefficient attached to the $\text{MgO} + \text{FeO}$ term causes this model to predict higher CO_2 solubilities than the calibration dataset for the andesitic-dacitic melt inclusions considered here.

The discrepancy between isobars for S-2014 and IM-2012 relative to MagmaSat are relatively similar for the Popocatépetl and Soufrière Hills melt compositions, while discrepancies for saturation pressures differ markedly (Figures [18a](#) and [18b](#) vs. Figures [18c](#) and [18d](#)). This is because the volatile contents of Popocatépetl melt inclusions are significantly more CO_2 -rich (~0.02 to 0.15 wt% and higher), and H_2O -poor (~1–3 wt%) than Soufrière Hills melt inclusions (<0.04 wt% CO_2 and 5–6 wt% H_2O). For this reason, calculated saturation pressures for Popocatépetl melt inclusions are sensitive to the treatment of both CO_2 and H_2O in solubility models (Figure [18b](#)), while those for Soufrière Hills melt inclusions are mostly sensitive to pure H_2O solubility. Thus, S-2014 overestimates saturation pressures for Popocatépetl melt inclusions because this model drastically underestimates the solubility of pure CO_2 . In contrast, S-2014 only slightly underestimates H_2O solubility relative to MagmaSat, so only

slightly overpredicts saturation pressures for H_2O -rich Soufrière Hills melt inclusions. The discrepancy between IM-2012 and MagmaSat is much smaller for Popocatépetl relative to Soufrière Hills because, fortuitously, the IM-2012-H isobar intercepts the MagmaSat isobar at H_2O contents similar to these Popocatépetl melt inclusions. IM-2012-H and -A drastically underestimates the solubility of pure H_2O , so overestimates saturation pressures for the H_2O -rich Soufrière Hills melt inclusions relative to other models.

It is worth noting that Iacono-Marziano never intended their model to be applied to andesites, and when discussing the limitations of their model, they explicitly warn that their empirical expressions poorly incorporates the effect of MgO and FeO on CO_2 solubility because of the restricted range of these oxides in the calibration dataset. We have included this discussion as an extreme example of the danger of extrapolating empirical models beyond their calibration range. However, the sensitivity of this model to the FeO and MgO content of the melt also presents issues when applied to high MgO basaltic liquids. For example, Wieser et al. (2021) showed that IM-2012 predicts higher saturation pressures for highly primitive (high MgO) melt inclusions from Kīlauea Volcano relative to S-2014 and MagmaSat. This likely reflects the higher values of $X_{\text{FeO} + \text{MgO}}$ in these melt inclusions relative to the calibration dataset, which causes IM-2012 to predict lower CO_2 solubility (the opposite directionality to that seen for the intermediate melt inclusions discussed here).

The H_2O -rich nature of Soufrière Hills melt inclusions means that VolatileCalc-Rhyolite predicts much more similar saturation pressures to MagmaSat (1.07–1.15×; Figure S6 in Supporting Information S1) than for Popocatépetl (1.1–1.5× higher; Figure S5 in Supporting Information S1), because the main failure of VolatileCalc-Rhyolite for intermediate compositions at moderate to high temperatures ($>850^\circ\text{C}$) is its prediction of pure CO_2 solubility (Figures 16, 18c, and 18d). The discrepancy for both VolatileCalc models and L-2005 relative to MagmaSat is significantly smaller than for S-2014 and IM-2012. This is because the solubility differences during evolution for basaltic to rhyolitic compositions are relatively small (30%–40%) compared to the error associated with the extrapolating an empirical model far beyond its compositional range. Overall, this case study shows the importance of checking that the calibration dataset of a model contains melts similar to those in the sample set of interest, particularly if the effect of melt composition is parameterized empirically.

7. Best Practices for Data Visualization and Curation

7.1. Isobar Diagrams: Limitations and Alternatives

As demonstrated in the preceding section, isobar diagrams are a useful tool to visualize variations in volatile solubility for a specific melt composition. However, many suites of melt inclusions have considerable major element variability, which translates into differing solubilities of H_2O - CO_2 at a given pressure, and different isobar shapes at a given pressure (Iacovino et al., 2021; Roggensack, 2001; Wieser et al., 2021). We use two suites of melt inclusions to demonstrate this point.

First, we consider a suite of basaltic melt inclusions from Butajira volcano in the Main Ethiopian Rift from Iddon and Edmonds (2020). We calculate isobars for a representative inclusion composition (BJ08_7; Figure 19a), and then we compare these to the isobars calculated for each individual melt inclusion composition at 1 and 3 kbar (Figures 19a and 19b). The 3 kbar isobars calculated from the composition of each individual melt inclusion from Butajira (Figure 19b) cover the entire region of H_2O - CO_2 space that is bracketed by the 2 and 4 kbar isobars calculated in MagmaSat for the representative melt inclusion composition (Figure 19a vs. Figure 19b). In fact, saturation pressures calculated using any given melt inclusion composition versus the major element composition of the melt inclusion in question can affect the saturation pressure by almost a factor of 2. By extension, visual inspection of melt inclusion volatile concentrations plotted on isobar diagrams may be associated with an error of this magnitude).

Second, we calculate isobars at 300 and 700 bars for a representative subset of melt inclusions from the 2018 eruption of Kīlauea with PEC-corrected MgO contents between 6.4 and 13.5 wt% (Wieser et al., 2021). Although less extreme than the Butajira example, the spread of isobars calculated for a single sample at 700 bars for multiple melt inclusions is wider than the distance between isobars calculated 100 bar apart for a specific melt inclusion. Similar isobar spreads are seen for both Kīlauea and Butajira using IM-2012 (Figures S8 and S9 in Supporting Information S1).

VESical solves the problem of potentially misleading isobar diagrams by facilitating rapid calculations of saturation pressures for large suites of melt inclusions. For example, calculating saturation pressures for the 33 melt

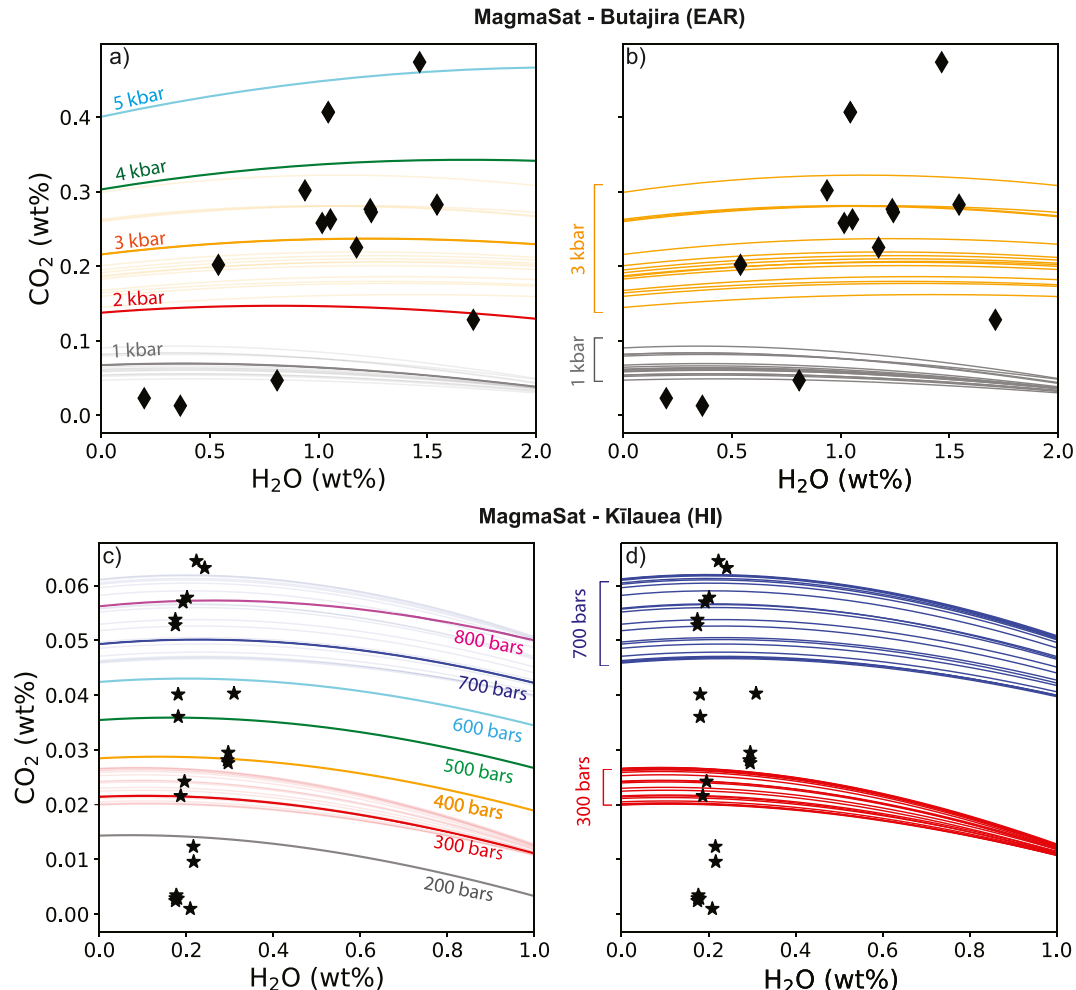


Figure 19. (a) and (b) Isobars for olivine-hosted melt inclusions from Iddon and Edmonds (2020) calculated at 1,170°C. (a) MagmaSat isobars for melt inclusion BJ08_7 from Butajira with melt inclusion volatile data overlain. (b) The 1 and 3 kbar isobars calculated for the major element composition of each individual melt inclusion from Butajira [underlain as light lines in (a)]. (c) and (d) As for (a) and (b), but using a representative subset of melt inclusions from Kilauea (Wieser et al., 2021). To save computation time as this study analyses >100 melt inclusions, PEC-corrected compositions were sorted by MgO content, and every fifth inclusion composition was used to calculate an isobar. Isobars are calculated for a temperature calculated from the melt inclusion MgO content using the thermometer of Helz and Thornber (1987).

inclusions in the dataset of Iddon and Edmonds (2020) using VolatileCalc-Basalt, S-2014, and IM-2012 takes only 4.2 s if VESIcal is run on the ENKI server. MagmaSat is slightly slower, taking 31.5 s (still <1 s per sample). MagmaSat calculations may run faster if ThermoEngine is installed locally (calculations take 26.3 s using a Dell Inspiron laptop with 16 GB RAM and an Intel-i7 processor, see <https://gitlab.com/ENKI-portal/ThermoEngine> for installation help).

Once users have calculated saturation pressures for each inclusion, a number of different *x*-*y* plots will provide more information than isobar diagrams. For example, Moore (2008) suggests that users could plot two graphs, one showing melt inclusion CO₂ content against saturation pressure and one showing melt inclusion H₂O contents against saturation pressure. This allows clustering of saturation pressures to be observed, and determination of the importance of each volatile species when calculating saturation pressure. Alternatively, saturation pressures could be plotted as histograms, cumulative density functions, or box/violin plots to assess clustering Wieser et al. (2022). Additionally, the ability to easily filter calculated saturation pressures by additional variables in python (e.g., host mineral content, amount of PEC, sample location, and stratigraphic height) will help to elucidate the record of the magmatic plumbing system preserved in different crystal populations. For example, Wieser

et al. (2021) show that melt inclusions hosted in low forsterite olivine crystals from Kilauea Volcano crystallized at ~1 to 2 km depth, while melt inclusions hosted within higher forsterite olivines crystallized at ~3 to 5 km depth.

7.2. Assessing Errors

The ability to calculate saturation pressures using a number of different models in VESIcal is advantageous, because it can provide assessment of the systematic errors associated with model choice. If different solubility models produce saturation pressures which are statistically distinguishable using tests such as ANOVA or the Kolmogorov-Smirnov test, or differences between models exceed 10%–20% (the approximate quoted error on most models), users need to evaluate their melt compositions, pressures and temperatures in the context of the calibration dataset of each solubility model. Several Jupyter Notebook aiding these comparisons are provided alongside VESIcal part I (Iacovino et al., 2021). Additionally, comparisons between any available experimental data for relevant melt compositions and different solubility models using a workflow similar to that used here for andesites (e.g., isobar diagrams as in Figure 16, plots of melt composition vs. calibration datasets) will help users select a suitable model. As well as examining melt compositions, users should also evaluate whether they are extrapolating temperature-sensitive models beyond the calibration range (as discussed here for VolatileCalc-Rhyolite).

In general, if a natural silicate melt composition is poorly represented by experimental data, MagmaSat is probably the best model to use, as its thermodynamic nature is more suitable to extrapolation to melt compositions not represented in the calibration dataset than empirical models, such as IM-2012, S-2014, or VolatileCalc-Basalt. However, the comprehensive nature of MagmaSat means that the fit to experimental data from any specific region of major element space is compromised by the fact the model is optimizing the overall fit to many different major element compositions. Thus, where present, models developed for specific volcanic centers, or highly weighted toward specific melt compositions (e.g., A-2019 for the six centers they investigate, or IM-2012 for alkaline compositions) may return a better fit. While these composition-specific models may be well calibrated in terms of melt composition, users must also check that they are applying the model within the recommended pressure and temperature range.

VESIcal also opens up the capability to handle errors arising from volatile solubility modeling using the advanced functionality of Python3 packages, such as NumPy, SciPy, and PyMC to perform Bayesian statistical techniques (e.g., Markov Chain Monte Carlo methods). This means the uncertainty in all input parameters (e.g., temperature, analytical uncertainties in volatile and major element contents, and uncertainty arising from PEC corrections) can be propagated into a resulting error distribution for each melt inclusion. These techniques are increasingly being utilized by igneous petrologists, with recent applications including calculating error distributions for diffusion timescales (Mutch et al., 2019), the contribution of melts from distinct mantle sources (Gleeson et al., 2020), and propagating uncertainties in vapor bubble growth models (Rasmussen et al., 2020).

7.3. Data Curation

Now that VESIcal makes it possible to calculate saturation pressures for large melt inclusion datasets in short amounts of time, it is vital that data is published in a way that allows such calculations to be performed retrospectively (e.g., recalculating literature saturation pressures from a given volcanic center/region to use a single solubility model). The concentration of major elements and volatile elements should be provided within a single spreadsheet or database, ideally alongside the composition of the mineral host. Additionally, if melt inclusions are corrected for PEC, both raw and corrected major and volatile element concentrations should be published. Particularly for more chemically complex host minerals like pyroxene and plagioclase, it is highly likely that community standards on the best PEC procedure will change with time. Finally, given that numerous recent studies have shown that bubble CO₂ contents can change calculated saturation pressures by up to an order of magnitude (Section 5), even if authors were unable to perform Raman analyses, it should be noted whether each melt inclusion contained a vapor bubble (and ideally an estimate of the volume proportion of the vapor bubble). This information may allow the CO₂ contents in vapor bubbles to be reconstructed theoretically by future studies, given the recent proliferation of vapor bubble growth models (e.g., Aster et al., 2016; MacLennan, 2017; Rasmussen et al., 2020).

Proper data curation is particularly vital in the world of volatile solubility modeling because it is very likely that many more experiments will be published over the next decade, allowing the creation of new solubility models that are calibrated over an even wider region of P – T and compositional space. Many publications could not be used for comparisons in this study, because there was simply no way to combine volatile element concentrations and major element concentrations (which were often reported in different tables with non-unique or non-matching sample names, or not reported at all). It would be a great shame if published melt inclusion datasets could not be input into these new models to recalculate saturation pressures, and gain a greater understanding of magma storage in the Earth's crust.

8. Future Work

The comparisons drawn in this review highlight several research areas where further experimental work is required to be able to distinguish which model behaviors are accurate. First, significantly more experiments are needed on andesitic-dacitic melt compositions. Figure 16 shows that it is currently impossible to differentiate a potential failure in any given solubility model from anomalies in any given set of experiments (e.g., the differential effect of addition of H_2O on CO_2 solubility in different experiments; Figure 16b vs. Figure 16f).

One of the challenges when assessing CO_2 solubility in andesitic-dacitic melts is the fact that CO_2 is present as both carbonate and molecular CO_2 . Carbon species do appear separately in FTIR spectra, but the accuracy of FTIR-derived volatile concentrations can be affected by peak overlap (e.g., Brooker et al., 2001b), as well as uncertainty in peak baseline and absorption coefficients (Botcharnikov et al., 2006; Mangan et al., 2021). SIMS cannot distinguish different carbon species (only yields total carbon), but may help to resolve issues with FTIR as a result of increased understanding of the optimal analysis conditions for volatiles in silicate glasses of the last few decades. However, in addition to its substantial cost relative to FTIR, accurate SIMS measurements are reliant on having a suite of standards with similar major element compositions and a range of volatile contents (and these standards are often characterized by FTIR, so are subject to the caveats mentioned above).

Second, the effect of redox on volatile solubility across the range encountered in terrestrial magmas is still poorly constrained (Section 5). This discrepancy largely reflects the fact that the redox conditions at which many experiments in the literature were conducted are uncertain and/or highly variable (e.g., Botcharnikov et al., 2006). Because of this uncertainty, many calibration datasets are built without being able to constrain the quantities of Fe_2O_3 and FeO for each experimental run. While our investigation of intermediate melts indicates that the strong sensitivity of CO_2 solubility to melt redox shown by P-2006 is likely anomalous because of the presence of experiments with extremely high calculated Fe^{3+}/Fe_T ratios in the calibration dataset, further experiments where Fe_2O_3 and FeO proportions are accurately measured are needed to be certain that this behavior is not real. It is also noteworthy that almost all the andesitic experiments were performed at higher oxygen fugacities than lavas erupted at volcanic arcs. When the calibration dataset for a given set of compositions is so small, this makes it difficult to deconvolve changes in volatile solubility with melt composition compared to redox. Recent advances in measurements of Fe^{3+}/Fe_T using Fe K-edge micro-X-ray absorption near-edge structure (XANES) spectroscopy in hydrous glasses (Cottrell et al., 2018) could provide an avenue to better constrain this parameter in future (and past) experimental products.

It is also worth noting that all the models discussed here only consider the effect of redox through terms for Fe^{2+} and Fe^{3+} in the melt, constraining their applicability to melts more oxidising than the IW buffer. In more reducing conditions, the co-existing CO_2 -rich phase may be graphite or diamond rather than a CO_2 -rich vapor phase (Eguchi & Dasgupta, 2018), and the dissolved volatile species may be CO , CH_4 , and H_2 (Mysen et al., 2009). This means that extreme caution is required when applying these solubility models to highly reducing conditions, such as those found on other planetary bodies (e.g., the Moon, Mars, and Mercury; Li et al., 2017).

Third, there is still significant uncertainty regarding the specifics of mixing between H_2O and CO_2 (i.e., non-ideality) at higher pressures. This reflects the difficulty in measuring mixed H_2O - CO_2 fluids that were in equilibrium with the melt during the experiment. If measured at all, methods in the literature span from puncture and weight loss of frozen capsules (i.e., when frozen the CO_2 is released, but not the H_2O ; Shishkina et al., 2010) to more sophisticated and accurate vacuum line manometry (Allison et al., 2019; Iacovino et al., 2013; Moore et al., 2008). New infinite path laser spectrometry technology may offer potential improvement of this critical

measurement, but challenges associated with small sample sizes remain. More work determining the pure CO₂ solubility as a function of pressure and temperature would also be of great benefit in constraining the behavior of H₂O-poor fluids.

Fourth, we show that the sensitivity of dissolved volatile contents to temperature is highly model-specific. Given the difficulties with constraining temperature sensitivity experimentally (Iacono-Marziano et al., 2012), we suggest that it may be best to parametrize future empirical models at a single temperature (e.g., A-2019 and S-2014), or incorporate the temperature sensitivity predicted by thermodynamical models, rather than introduce a spurious temperature dependency which is not founded in experimental data, nor consistent with the relative entropy of melt and fluid terms.

Finally, it is worth noting that all of the solubility models discussed only consider H₂O-CO₂ in the vapor phase, while in reality, natural fluids in volcanic systems may contain relatively large proportions of F, Cl, and S, as well as a separate brine phase (Botcharnikov et al., 2007). Additionally, at higher pressures and temperatures, significant quantities of major element species will dissolve into a H₂O-rich fluid (e.g., Si, Na, and K), with silicate melt and hydrous fluids becoming completely miscible above a critical temperature (Bureau & Keppler, 1999). This causes a pure H₂O model to underestimate the true solubility of H₂O at these conditions. Combined with the fact that it is near-impossible to quench silicate melts with $> 9\pm 1$ wt% H₂O to a glass phase which can be analyzed by SIMS or FTIR (Gavrilenko et al., 2019; Mitchell et al., 2017), quantifying the solubility of H₂O at condition relevant to lower crustal magma storage will require experimental innovations (e.g., Makhluf et al., 2020; Mitchell et al., 2017). Models will also need to be developed which are capable of calculating equilibria between a silicic melt phase and a complex aqueous fluid (Ghiorso & Sverjensky, 2016; Huang & Sverjensky, 2019; Sverjensky et al., 2014). Recently, a new equation of state for estimating the dielectric constant of water and new equation of state parameters for major solute species has enabled thermodynamic mass transfer calculations for fluid-rock systems up to 6 GPa and 1,000°C (Debret & Sverjensky, 2017; Facq et al., 2014; Huang & Sverjensky, 2019; Sverjensky et al., 2014), significantly advancing our ability to model fluid behavior in volcanically relevant systems (e.g., Iacovino et al., 2020).

9. Conclusion

This review uses the new open-source Python3 tool VESIcal (Iacovino et al., 2021), in addition to VolatileCalc (Newman & Lowenstern, 2002) and Solwcad (Papale et al., 2006) to draw extensive comparisons between the behavior of nine different solubility models for a range of melt compositions. We show that these models predict surprisingly different volatile solubilities, particularly for pure CO₂ or mixed CO₂-H₂O fluids. Even for melt compositions that are well represented in the calibration datasets of multiple models (e.g., MORBs), calculated solubilities for pure CO₂ can deviate from one another by factors of ~ 2 . Differential treatment of H₂O-CO₂ mixing enhances these differences when calculating volatile solubility for melts containing both volatile species. The solubility of CO₂ predicted by different rhyolitic models also differs substantially, overwhelming other sources of uncertainty such as analytical errors on measurements of volatile contents or uncertainties in crustal density profiles. Differences are most pronounced for peralkaline rhyolites where there are fewer experimental constraints.

Overall, these comparisons demonstrate that it is vital to pick a model which is calibrated for the pressure, temperature, and melt composition of interest. Choice of a poorly calibrated model could introduce a systematic error of a factor of 2 or more in estimates of saturation pressures. This has widespread implications for published estimates of magma storage depths within volcanic systems, and indicates that re-evaluation of published magma storage depths calculated using older models may be warranted.

We also investigate the sensitivity of different models to variation in parameters such as H₂O content (with relevance to diffusive re-equilibration), CO₂ content (with relevance to melt inclusion vapor bubble growth), temperature, and oxygen fugacity. We suggest that by performing similar sensitivity tests in the future, the uncertainties affecting calculations of volatile solubility in magmatic systems (and therefore the limitations of each study) can be quantified. We also demonstrate that isobar diagrams are a poor visualization method for determining magma storage depths in systems where melt inclusions possess diverse major element chemistry, so encourage users to take advantage of the ease and speed of calculations in VESIcal to determine the saturation pressure for each melt inclusion of interest. Saturation pressures can then be visualized as various cumulative frequency distributions,

histograms, or violin plots, and plotted against melt inclusion H_2O and CO_2 contents, or parameters relating to host crystal chemistry, to gain greater insight into the factors controlling magma storage depths within volcanic systems.

Finally, we identify that further experimental constraints are required to accurately estimate volatile solubility in andesitic-dacitic melts, and that further work is needed to understand the effect of temperature, redox, and non-ideal mixing between H_2O - CO_2 on volatile solubility.

Data Availability Statement

The Jupyter Notebook and associated Excel spreadsheets are hosted at https://github.com/PennyWieser/VESIcal_II, and are archived with Zenodo (10.5281/zenodo.5798833, <https://zenodo.org/record/5798833>). Videos showing how to use VESIcal are hosted on YouTube https://www.youtube.com/channel/UCpvCCs5KM_XzOxXWm0seF8Qw.

Acknowledgments

Penny E. Wieser acknowledges funding from a NERC DTP studentship (NE/L002507/1) and a National Science Foundation grant (1948862). Kayla Iacovino and Gordon Moore were supported by the NASA Jacobs JETS Contract (NN-J13HA01C). We acknowledge support from the National Science Foundation, ICER-20-26904, granted to OFM Research (PI: Ghiorso) for maintaining the ENKI server used to perform VESIcal calculations. We thank Jackie Dixon, Giada Iacono-Marziano, Paolo Papale, and Mark Ghiorso for help tracking down and using existing calculation tools, and for help constructing model calibration datasets. We also thank Mark Ghiorso and Paolo Papale for helpful reviews which improved the clarity and robustness of the first version and David Neave on the second version. We greatly appreciate the late Peter Fox for his editorial handling of the first draft of this manuscript and his overall support for the VESIcal project. We thank everyone involved in the development and maintenance of open-source python libraries (NumPy, Pandas, Matplotlib), and tools like Zenodo, GitHub, and Binder, without whom this project would not have been possible.

References

Allan, J. F., Batiza, R., Perfit, M. R., Fornari, D. J., & Sack, R. O. (1989). Petrology of lavas from the Lamont seamount chain and adjacent East Pacific Rise, 10 n. *Journal of Petrology*, 30(5), 1245–1298.

Allison, C. M., Roggensack, K., & Clarke, A. B. (2019). H_2O - CO_2 solubility in alkali-rich mafic magmas: New experiments at mid-crustal pressures. *Contributions to Mineralogy and Petrology*, 174(7), 58.

Allison, C. M., Roggensack, K., & Clarke, A. B. (2021). Highly explosive basaltic eruptions driven by CO_2 exsolution. *Nature Communications*, 12, 217.

Anderson, A. T. (1974). Evidence for a picritic, volatile-rich magma beneath Mt. Shasta, California. *Journal of Petrology*, 15(2), 243–267.

Aster, E. M., Wallace, P. J., Moore, L. R., Watkins, J., Gazel, E., & Bodnar, R. J. (2016). Reconstructing CO_2 concentrations in basaltic melt inclusions using Raman analysis of vapor bubbles. *Journal of Volcanology and Geothermal Research*, 323, 148–162.

Atlas, Z. D., Dixon, J. E., Sen, G., Finny, M., & Martin-Del Pozzo, A. L. (2006). Melt inclusions from Volcán Popocatépetl and Volcán de Colima, Mexico: Melt evolution due to vapor-saturated crystallization during ascent. *Journal of Volcanology and Geothermal Research*, 153(3–4), 221–240.

Behrens, H., Ohlhorst, S., Holtz, F., & Champenois, M. (2004). CO_2 solubility in dacitic melts equilibrated with H_2O - CO_2 fluids: Implications for modeling the solubility of CO_2 in silicic melts. *Geochimica et Cosmochimica Acta*, 68(22), 4687–4703.

Blank, J., Stolper, E., & Carroll, M. (1993). Solubilities of carbon dioxide and water in rhyolitic melt at 850°C and 750 bars. *Earth and Planetary Science Letters*, 119(1–2), 27–36.

Blundy, J., & Cashman, K. (2005). Rapid decompression-driven crystallization recorded by melt inclusions from Mount St. Helens Volcano. *Geology*, 33(10), 793–796.

Blundy, J., Cashman, K., & Humphreys, M. (2006). Magma heating by decompression-driven crystallization beneath andesite volcanoes. *Nature*, 443(7107), 76–80.

Botcharnikov, R. E., Behrens, H., & Holtz, F. (2006). Solubility and speciation of C–O–H fluids in andesitic melt at T=1100–1300°C and P=200 and 500 MPa. *Chemical Geology*, 229(1–3), 125–143.

Botcharnikov, R. E., Holtz, F., & Behrens, H. (2007). The effect of CO_2 on the solubility of H_2O -Cl fluids in andesitic melt. *European Journal of Mineralogy*, 19(5), 671–680.

Bowen, N. (1928). *The evolution of the igneous rocks*. Oxford University Press.

Brooker, R., Kohn, S., Holloway, J., & McMillan, P. (2001a). Structural controls on the solubility of CO_2 in silicate melts: Part I: Bulk solubility data. *Chemical Geology*, 174(1–3), 225–239.

Brooker, R., Kohn, S., Holloway, J., & McMillan, P. (2001b). Structural controls on the solubility of CO_2 in silicate melts: Part II: IR characteristics of carbonate groups in silicate glasses. *Chemical Geology*, 174(1–3), 241–254.

Bucholz, C. E., Gaetani, G. A., Behn, M. D., & Shimizu, N. (2013). Post-entrapment modification of volatiles and oxygen fugacity in olivine-hosted melt inclusions. *Earth and Planetary Science Letters*, 374, 145–155.

Bureau, H., & Keppler, H. (1999). Complete miscibility between silicate melts and hydrous fluids in the upper mantle: Experimental evidence and geochemical implications. *Earth and Planetary Science Letters*, 165(2), 187–196.

Burgisser, A., Alléti, M., & Scaillet, B. (2015). Simulating the behavior of volatiles belonging to the C–O–H–S system in silicate melts under magmatic conditions with the software d-compress. *Computers & Geosciences*, 79, 1–14.

Burnham, C. W. (1979). The importance of volatile constituents. In H. S. Yoder, (Ed.), *The evolution of the igneous rocks* (pp. 439–482). Princeton University Press.

Burnham, C. W., & Davis, N. (1971). The role of H_2O in silicate melts: I. P-V-T relations in the system $NaAlSi_3O_8$ - H_2O to 10 kilobars and 1000°C. *American Journal of Science*, 270(1), 54–79.

Burnham, C. W., & Davis, N. (1974). The role of H_2O in silicate melts; II, Thermodynamic and phase relations in the system $NaAlSi_3O_8$ - H_2O to 10 kilobars, 700 degrees to 1100 degrees C. *American Journal of Science*, 274(8), 902–940.

Cassidy, M., Edmonds, M., Watt, S. F., Palmer, M. R., & Germon, T. M. (2015). Origin of basalts by hybridization in andesite-dominated arcs. *Journal of Petrology*, 56(2), 325–346.

Cocheo, P., & Holloway, J. (1993). *The solubility of H_2O in basanitic melts at low pressure* (Vol. 74). EOS Transactions of the American Geophysical Union.

Cottrell, E., Lanzirotti, A., Mysen, B., Birner, S., Kelley, K. A., Botcharnikov, R., & Newville, M. (2018). A Mössbauer-based XANES calibration for hydrous basalt glasses reveals radiation-induced oxidation of Fe. *American Mineralogist*, 103(4), 489–501.

Debret, B., & Sverjensky, D. (2017). Highly oxidising fluids generated during serpentinite breakdown in subduction zones. *Scientific Reports*, 7(1), 1–6.

Dingwell, D. B. (1986). Volatile solubilities in silicate melts. In C. M. Scarfe, (Ed.), *Silicate melts. Mineralogical Association of Canada Short course handbook* (Vol. 12, pp. 93–129). Mineralogical Association of Canada.

Dixon, J. E. (1997). Degassing of alkalic basalts. *American Mineralogist*, 82(3–4), 368–378.

Dixon, J. E., Stolper, E. M., & Holloway, J. R. (1995). An experimental study of water and carbon dioxide solubilities in mid-ocean ridge basaltic liquids. Part I: Calibration and solubility models. *Journal of Petrology*, 36(6), 1607–1631.

Duan, X. (2014). A general model for predicting the solubility behavior of H_2O – CO_2 fluids in silicate melts over a wide range of pressure, temperature and compositions. *Geochimica et Cosmochimica Acta*, 125, 582–609.

Duan, Z., & Zhang, Z. (2006). Equation of state of the H_2O , CO_2 , and H_2O – CO_2 systems up to 10 GPa and 2573.15 K: Molecular dynamics simulations with ab initio potential surface. *Geochimica et cosmochimica acta*, 70(9), 2311–2324.

Eggler, D. (1973). Role of CO_2 in melting processes in the mantle. *Carnegie Institute of Washington Yearbook*, 72, 457–467.

Eguchi, J., & Dasgupta, R. (2018). A CO_2 solubility model for silicate melts from fluid saturation to graphite or diamond saturation. *Chemical Geology*, 487, 23–38.

Facq, S., Daniel, I., Montagnac, G., Cardon, H., & Sverjensky, D. A. (2014). In situ Raman study and thermodynamic model of aqueous carbonate speciation in equilibrium with aragonite under subduction zone conditions. *Geochimica et Cosmochimica Acta*, 132, 375–390.

Fine, G., & Stolper, E. (1986). Dissolved carbon dioxide in basaltic glasses: Concentrations and speciation. *Earth and Planetary Science Letters*, 76(3–4), 263–278.

Flowers, G. C. (1979). Correction of Holloway's (1977) adaptation of the modified Redlich-Kwong equation of state for calculation of the fugacities of molecular species in supercritical fluids of geologic interest. *Contributions to Mineralogy and Petrology*, 69(3), 315–318.

Fogel, R. A., & Rutherford, M. J. (1990). The solubility of carbon dioxide in rhyolitic melts: a quantitative FTIR study. *American Mineralogist*, 75(11–12), 1311–1326.

Freise, M. (2004). *Differenzierung von basalten einer "large igneous province" am Beispiel des Kerguelen Plateaus. Eine experimentelle Studie* (Unpublished doctoral dissertation, PhD thesis). University of Hannover.

Gaborieau, M., Laubier, M., Bolfan-Casanova, N., Mccammon, C., Vantelon, D., Chumakov, A., & Venugopal, S. (2020). Determination of Fe^{3+} – Fe of olivine-hosted melt inclusions using Mössbauer and XANES spectroscopy. *Chemical Geology*, 547(7215), 119646.

Gaetani, G. A., O'Leary, J. A., Shimizu, N., Bucholz, C. E., & Newville, M. (2012). Rapid reequilibration of H_2O and oxygen fugacity in olivine-hosted melt inclusions. *Geology*, 40(10), 915–918.

Gavrilenko, M., Krawczynski, M., Ruprecht, P., Li, W., & Catalano, J. G. (2019). The quench control of water estimates in convergent margin magmas. *American Mineralogist*, 104(7), 936–948.

Gerlach, T. M. (1986). Exsolution of H_2O , CO_2 , and S during eruptive episodes at Kilauea Volcano, Hawaii. *Journal of Geophysical Research: Solid Earth*, 91(B12), 12177–12185.

Ghiorso, M. S., Carmichael, I. S., Rivers, M. L., & Sack, R. O. (1983). The Gibbs free energy of mixing of natural silicate liquids; an expanded regular solution approximation for the calculation of magmatic intensive variables. *Contributions to Mineralogy and Petrology*, 84(2), 107–145.

Ghiorso, M. S., & Gualda, G. A. (2015). An H_2O – CO_2 mixed fluid saturation model compatible with rhyolite-melts. *Contributions to Mineralogy and Petrology*, 169(6), 1–30.

Ghiorso, M. S., & Sack, R. O. (1995). Chemical mass transfer in magmatic processes IV. A revised and internally consistent thermodynamic model for the interpolation and extrapolation of liquid-solid equilibria in magmatic systems at elevated temperatures and pressures. *Contributions to Mineralogy and Petrology*, 119(2–3), 197–212.

Ghiorso, M. S., & Sverjensky, D. A. (2016). The melts-dew connection: Integration of thermodynamic models for magmatic systems and aqueous fluids at elevated temperatures and pressures. *AGU Fall Meeting Abstracts*, 2016, V33H–04.

Gleeson, M. L., Gibson, S. A., & Williams, H. M. (2020). Novel insights from Fe-isotopes into the lithological heterogeneity of ocean island basalts and plume-influenced MORBs. *Earth and Planetary Science Letters*, 535, 116114.

Gleeson, M. L., Stock, M. J., Pyle, D. M., Mather, T. A., Hutchison, W., Yirgu, G., & Wade, J. (2017). Constraining magma storage conditions at a restless volcano in the main Ethiopian rift using phase equilibrium models. *Journal of Volcanology and Geothermal Research*, 337, 44–61.

Goltz, A. E., Krawczynski, M. J., Gavrilenko, M., Gorbach, N. V., & Ruprecht, P. (2020). Evidence for superhydrous primitive arc magmas from mafic enclaves at Shiveluch Volcano, Kamchatka. *Contributions to Mineralogy and Petrology*, 175(12), 1–26.

Goranson, R. W. (1931). Solubility of water in granite magmas. *Eos*, 12(1), 183.

Gualda, G. A., & Ghiorso, M. S. (2015). MELTS_Excel: An Microsoft Excel-based melts interface for research and teaching of magma properties and evolution. *Geochemistry, Geophysics, Geosystems*, 16(1), 315–324.

Gualda, G. A., Ghiorso, M. S., Lemons, R. V., & Carley, T. L. (2012). Rhyolite-melts: A modified calibration of melts optimized for silica-rich, fluid-bearing magmatic systems. *Journal of Petrology*, 53(5), 875–890.

Hamilton, D., Burnham, C. W., & Osborn, E. (1964). The solubility of water and effects of oxygen fugacity and water content on crystallization in mafic magmas. *Journal of Petrology*, 5(1), 21–39.

Hartley, M. E., MacLennan, J., Edmonds, M., & Thordarson, T. (2014). Reconstructing the deep CO_2 degassing behaviour of large basaltic fissure eruptions. *Earth and Planetary Science Letters*, 393, 120–131.

Hartley, M. E., Neave, D. A., MacLennan, J., Edmonds, M., & Thordarson, T. (2015). Diffusive over-hydration of olivine-hosted melt inclusions. *Earth and Planetary Science Letters*, 425, 168–178.

Hauri, E. (2002). Sims analysis of volatiles in silicate glasses, 2: Isotopes and abundances in Hawaiian melt inclusions. *Chemical Geology*, 183(1–4), 115–141.

Hauri, E., Kent, A. J., & Arndt, N. (2002). Melt inclusions at the millennium: Toward a deeper understanding of magmatic processes. *Chemical Geology*, 183(1–4), 1–3.

Helz, R., & Thornber, C. R. (1987). Geothermometry of Kilauea Iki Lava Lake, Hawaii. *Bulletin of Volcanology*, 49(5), 651–668.

Hervig, R., Dunbar, N., Westrich, H. R., & Kyle, P. R. (1989). Pre-eruptive water content of rhyolitic magmas as determined by ion microprobe analyses of melt inclusions in phenocrysts. *Journal of Volcanology and Geothermal Research*, 36(4), 293–302.

Hervig, R., & Williams, P. (1988). SIMS microanalysis of minerals and glasses for H and D. In A. Benninghoven, A. M. Huber, & H. W. Werne, (Eds.), *Secondary ion mass spectrometry, SIMS VI Proceedings* (pp. 961–964). John Wiley & Sons.

Hess, K., & Dingwell, D. (1996). Viscosities of hydrous leucogranitic melts: A non-Arrhenian model. *American Mineralogist*, 81(9–10), 1297–1300.

Holloway, J. R. (1977). Fugacity and activity of molecular species in supercritical fluids. In D. G. Fraser, (Ed.), *Thermodynamics in geology* (pp. 161–181). Springer.

Holloway, J. R., & Blank, J. G. (1994). Application of experimental results to C–O–H species in natural melts. *Reviews in mineralogy*, 30, 187.

Huang, F., & Sverjensky, D. A. (2019). Extended deep earth water model for predicting major element mantle metasomatism. *Geochimica et Cosmochimica Acta*, 254, 192–230.

Huber, C., Townsend, M., Degruyter, W., & Bachmann, O. (2019). Optimal depth of subvolcanic magma chamber growth controlled by volatiles and crust rheology. *Nature Geoscience*, 12(9), 762–768.

Huppert, H. E., & Woods, A. W. (2002). The role of volatiles in magma chamber dynamics. *Nature*, 420(6915), 493–495.

Husen, A., Almeev, R. R., & Holtz, F. (2016). The effect of H_2O and pressure on multiple saturation and liquid lines of descent in basalt from the Shatsky Rise. *Journal of Petrology*, 57(2), 309–344.

Iacono-Marziano, G., Morizet, Y., Le Trong, E., & Gaillard, F. (2012). New experimental data and semi-empirical parameterization of H_2O – CO_2 solubility in mafic melts. *Geochimica et Cosmochimica Acta*, 97, 1–23.

Iacobino, K., Guild, M. R., & Till, C. B. (2020). Aqueous fluids are effective oxidizing agents of the mantle in subduction zones. *Contributions to Mineralogy and Petrology*, 175(4), 1–21.

Iacobino, K., Matthews, S., Wieser, P. E., Moore, G., & Begue, F. (2021). VESical part I: An open source thermodynamic model engine for mixed volatile (H_2O – CO_2) solubility in silicate melts. *Earth and Space Science*. <https://doi.org/10.31223/X5D606>

Iacobino, K., Moore, G., Roggensack, K., Oppenheimer, C., & Kyle, P. (2013). H_2O – CO_2 solubility in mafic alkaline magma: Applications to volatile sources and degassing behavior at Erebus Volcano, Antarctica. *Contributions to Mineralogy and Petrology*, 166(3), 845–860.

Iddon, F., & Edmonds, M. (2020). Volatile-rich magmas distributed through the upper crust in the main Ethiopian rift. *Geochemistry, Geophysics, Geosystems*, 21(6), e2019GC008904.

Jakobsson, S. (1997). Solubility of water and carbon dioxide in an icelandite at 1400°C and 10 kilobars. *Contributions to Mineralogy and Petrology*, 127(1–2), 129–135.

Kerrick, D., & Jacobs, G. (1981). A modified Redlich-Kwong equation for H_2O , CO_2 , and H_2O – CO_2 mixtures at elevated pressures and temperatures. *American Journal of Science*, 281(6), 735–767.

King, P., & Holloway, J. (2002). CO_2 solubility and speciation in intermediate (andesitic) melts: The role of H_2O and composition. *Geochimica et Cosmochimica Acta*, 66(9), 1627–1640.

Koleszar, A., Kent, A. J., Wallace, P. J., & Scott, W. E. (2012). Controls on long-term low explosivity at andesitic arc volcanoes: Insights from Mount Hood, Oregon. *Journal of Volcanology and Geothermal Research*, 219, 1–14.

Koleszar, A., Saal, A., Hauri, E., Nagle, A., Liang, Y., & Kurz, M. (2009). The volatile contents of the galapagos plume; evidence for H_2O and f open system behavior in melt inclusions. *Earth and Planetary Science Letters*, 287(3–4), 442–452.

La Spina, G., Arzilli, F., Llewellyn, E., Burton, M., Clarke, A. B., Vitturi, M. D., & Mader, H. (2021). Explosivity of basaltic lava fountains is controlled by magma rheology, ascent rate and outgassing. *Earth and Planetary Science Letters*, 553, 116658.

Le Voyer, M., Hauri, E., Cottrell, E., Kelley, K. A., Salters, V. J., Langmuir, C. H., & Füri, E. (2019). Carbon fluxes and primary magma CO_2 contents along the global mid-ocean ridge system. *Geochemistry, Geophysics, Geosystems*, 20(3), 1387–1424.

Lesne, P., Scaillet, B., Pichavant, M., & Beny, J.-M. (2011). The carbon dioxide solubility in alkali basalts: An experimental study. *Contributions to Mineralogy and Petrology*, 162(1), 153–168.

Lesne, P., Scaillet, B., Pichavant, M., Iacono-Marziano, G., & Beny, J.-M. (2011). The H_2O solubility of alkali basaltic melts: An experimental study. *Contributions to Mineralogy and Petrology*, 162(1), 133–151.

Li, Y., Dasgupta, R., & Tsuno, K. (2017). Carbon contents in reduced basalts at graphite saturation: Implications for the degassing of Mars, Mercury, and the Moon. *Journal of Geophysical Research: Planets*, 122(6), 1300–1320.

Liu, Y., Zhang, Y., & Behrens, H. (2005). Solubility of H_2O in rhyolitic melts at low pressures and a new empirical model for mixed H_2O – CO_2 solubility in rhyolitic melts. *Journal of Volcanology and Geothermal Research*, 143(1–3), 219–235.

Lloyd, A. S., Plank, T., Ruprecht, P., Hauri, E., & Rose, W. (2013). Volatile loss from melt inclusions in pyroclasts of differing sizes. *Contributions to Mineralogy and Petrology*, 165(1), 129–153.

Lowenstern, J. B. (1995). Applications of silicate-melt inclusions to the study of magmatic volatiles. *Magmas, fluids and ore deposits*, 23, 71–99.

Lowenstern, J. B. (2001). Carbon dioxide in magmas and implications for hydrothermal systems. *Mineralium Deposita*, 36(6), 490–502.

Lowenstern, J. B. (2003). Melt inclusions come of age: Volatiles, volcanoes, and Sorby's legacy. In B. De Vivo, & R. J. Bodnar, (Eds.), *Melt inclusions in volcanic systems: Methods, applications and problems: Developments in volcanology* (Vol. 5, pp. 1–21). Elsevier.

Lucic, G., Berg, A.-S., & Stix, J. (2016). Water-rich and volatile-undersaturated magmas at Hekla Volcano, Iceland. *Geochemistry, Geophysics, Geosystems*, 17(8), 3111–3130.

MacLennan, J. (2017). Bubble formation and decrepitation control the CO_2 content of olivine-hosted melt inclusions. *Geochemistry, Geophysics, Geosystems*, 18(2), 597–616.

Makhfuf, A. R., Newton, R., & Manning, C. (2020). Experimental investigation of phase relations in the system $NaAlSi_3O_8$ – H_2O at high temperatures and pressures: Liquidus relations, liquid–vapor mixing, and critical phenomena at deep crust–upper mantle conditions. *Contributions to Mineralogy and Petrology*, 175(8), 1–20.

Mangan, M. T., Sisson, T. W., Hankins, W. B., Shimizu, N., & Vennemann, T. (2021). Constraints on deep, CO_2 -rich degassing at arc volcanoes from solubility experiments on hydrous basaltic andesite of Pavlof Volcano, Alaska Peninsula, at 300 to 1200 MPa. *American Mineralogist*, 106(5), 762–773.

Métrich, N., & Wallace, P. J. (2008). Volatile abundances in basaltic magmas and their degassing paths tracked by melt inclusions. *Reviews in mineralogy and geochemistry*, 69(1), 363–402.

Mironov, N., Tobelko, D., Smirnov, S., Portnyagin, M. V., & Krasheninnikov, S. (2020). Estimation of CO_2 content in the gas phase of melt inclusions using Raman spectroscopy: Case study of inclusions in olivine from the Karymsky Volcano (Kamchatka). *Russian Geology and Geophysics*, 61(5–6), 600–610.

Mitchell, A. L., Gaetani, G. A., O'leary, J. A., & Hauri, E. H. (2017). H_2O solubility in basalt at upper mantle conditions. *Contributions to Mineralogy and Petrology*, 172(10), 1–16.

Moore, G. (2008). Interpreting H_2O and CO_2 contents in melt inclusions: Constraints from solubility experiments and modeling. *Reviews in Mineralogy and Geochemistry*, 69(1), 333–362.

Moore, G., & Carmichael, I. (1998). The hydrous phase equilibria (to 3 kbar) of an andesite and basaltic andesite from western Mexico: Constraints on water content and conditions of phenocryst growth. *Contributions to Mineralogy and Petrology*, 130(3–4), 304–319.

Moore, G., Roggensack, K., & Klonowski, S. (2008). A low-pressure–high-temperature technique for the piston-cylinder. *American Mineralogist*, 93(1), 48–52.

Moore, G., Vennemann, T., & Carmichael, I. (1998). An empirical model for the solubility of H_2O in magmas to 3 kilobars. *American Mineralogist*, 83(1), 36–42.

Moore, L. R., Gazel, E., Tuohy, R., Lloyd, A. S., Esposito, R., Steele-MacInnis, M., & Bodnar, R. J. (2015). Bubbles matter: An assessment of the contribution of vapor bubbles to melt inclusion volatile budgets. *American Mineralogist*, 100(4), 806–823.

Mutch, E. J., MacLennan, J., Shorttle, O., Edmonds, M., & Rudge, J. F. (2019). Rapid transcrustal magma movement under Iceland. *Nature Geoscience*, 12(7), 569–574.

Mysen, B. O. (1976). The role of volatiles in silicate melts; solubility of carbon dioxide and water in feldspar, pyroxene, and feldspathoid melts to 30 kb and 1625 degrees C. *American Journal of Science*, 276(8), 969–996.

Mysen, B. O., Eggler, D. H., Seitz, M., & Holloway, J. R. (1976). Carbon dioxide in silicate melts and crystals; part I, solubility measurements. *American Journal of Science*, 276(4), 455–479.

Mysen, B. O., Fogel, M. L., Morrill, P. L., & Cody, G. D. (2009). Solution behavior of reduced C-O-H volatiles in silicate melts at high pressure and temperature. *Geochimica et Cosmochimica Acta*, 73(6), 1696–1710.

Newman, S., & Lowenstern, J. B. (2002). Volatilecalc: A silicate melt–H₂O–CO₂ solution model written in visual basic for excel. *Computers & Geosciences*, 28(5), 597–604.

Ochs, F. A., & Lange, R. A. (1999). The density of hydrous magmatic liquids. *Science*, 283(5406), 1314–1317.

Papale, P. (1997). Modeling of the solubility of a one-component H₂O or CO₂ fluid in silicate liquids. *Contributions to Mineralogy and Petrology*, 126(3), 237–251.

Papale, P. (1999). Modeling of the solubility of a two-component H₂O+CO₂ fluid in silicate liquids. *American Mineralogist*, 84(4), 477–492.

Papale, P., Moretti, R., & Barbato, D. (2006). The compositional dependence of the saturation surface of H₂O+CO₂ fluids in silicate melts. *Chemical Geology*, 229(1–3), 78–95.

Papale, P., Neri, A., & Macedonio, G. (1999). The role of water content and magma composition on explosive eruption dynamics. *Physics and Chemistry of the Earth, Part A: Solid Earth and Geodesy*, 24(11–12), 969–975.

Plank, T., Kelley, K. A., Zimmer, M. M., Hauri, E., & Wallace, P. J. (2013). Why do mafic arc magmas contain 4 wt% water on average? *Earth and Planetary Science Letters*, 364, 168–179.

Portnyagin, M., Almeev, R., Matveev, S., & Holtz, F. (2008). Experimental evidence for rapid water exchange between melt inclusions in olivine and host magma. *Earth and Planetary Science Letters*, 272(3–4), 541–552.

Putirka, K. D. (2008). Thermometers and barometers for volcanic systems. *Reviews in Mineralogy and Geochemistry*, 69(1), 61–120.

Rasmussen, D. J., Plank, T. A., Wallace, P. J., Newcombe, M. E., & Lowenstern, J. B. (2020). Vapor-bubble growth in olivine-hosted melt inclusions. *American Mineralogist*, 105(12), 1898–1919.

Reubi, O., & Blundy, J. (2009). A dearth of intermediate melts at subduction zone volcanoes and the petrogenesis of arc andesites. *Nature*, 461(7268), 1269–1273.

Roedder, E. (1979). Origin and significance of magmatic inclusions. *Bulletin de Mineralogie*, 102(5), 487–510.

Roggensack, K. (2001). Unraveling the 1974 eruption of Fuego Volcano (Guatemala) with small crystals and their young melt inclusions. *Geology*, 29(10), 911–914.

Rohatgi, A. (2017). *WebPlotDigitizer*. Retrieved from <https://automeris.io/WebPlotDigitizer>

Saal, A. E., Hauri, E., Langmuir, C. H., & Perfit, M. R. (2002). Vapour undersaturation in primitive mid-ocean-ridge basalt and the volatile content of Earth's upper mantle. *Nature*, 419(6906), 451–455.

Shishkina, T., Botcharnikov, R. E., Holtz, F., Almeev, R. R., Jazwa, A. M., & Jakubiak, A. A. (2014). Compositional and pressure effects on the solubility of H₂O and CO₂ in mafic melts. *Chemical Geology*, 388, 112–129.

Shishkina, T., Botcharnikov, R. E., Holtz, F., Almeev, R., & Portnyagin, M. V. (2010). Solubility of H₂O- and CO₂-bearing fluids in tholeiitic basalts at pressures up to 500 MPa. *Chemical geology*, 277(1–2), 115–125.

Sides, I., Edmonds, M., MacLennan, J., Swanson, D., & Houghton, B. (2014a). Eruption style at Kīlauea Volcano in Hawai'i linked to primary melt composition. *Nature Geoscience*, 7(6), 464.

Sides, I., Edmonds, M., MacLennan, J., Swanson, D., & Houghton, B. (2014b). Magma mixing and high fountaining during the 1959 kīlauea iki eruption, Hawai'i. *Earth and Planetary Science Letters*, 400, 102–112.

Silver, L. A. (1988). *Water in silicate glasses* (Unpublished doctoral dissertation). California Institute of Technology.

Silver, L. A., Ihinger, P. D., & Stolper, E. (1990). The influence of bulk composition on the speciation of water in silicate glasses. *Contributions to Mineralogy and Petrology*, 104(2), 142–162.

Silver, L. A., & Stolper, E. (1989). Water in albitic glasses. *Journal of petrology*, 30(3), 667–709.

Steele-MacInnis, M., Esposito, R., & Bodnar, R. J. (2011). Thermodynamic model for the effect of post-entrapment crystallization on the H₂O–CO₂ systematics of vapor-saturated, silicate melt inclusions. *Journal of Petrology*, 52(12), 2461–2482.

Stevenson, J. A. (2015). *TASplot*. Retrieved from <https://bitbucket.org/jsteven5/tasplot/src/master/>

Stolper, E. (1982). Water in silicate glasses: An infrared spectroscopic study. *Contributions to Mineralogy and Petrology*, 81(1), 1–17.

Stolper, E., Fine, G., Johnson, T., & Newman, S. (1987). Solubility of carbon dioxide in albitic melt. *American Mineralogist*, 72(11–12), 1071–1085.

Sverjensky, D. A., Harrison, B., & Azzolini, D. (2014). Water in the deep earth: The dielectric constant and the solubilities of quartz and corundum to 60 kb and 1200 C. *Geochemistry et Cosmochimica Acta*, 129, 125–145.

Tamura, Y., & Tatsumi, Y. (2002). Remelting of an andesitic crust as a possible origin for rhyolitic magma in oceanic arcs: An example from the izu–bonin arc. *Journal of Petrology*, 43(6), 1029–1047.

Tucker, J. M., Hauri, E., Pietruszka, A. J., Garcia, M. O., Marske, J. P., & Truskell, F. A. (2019). A high carbon content of the Hawaiian mantle from olivine-hosted melt inclusions. *Geochemistry et Cosmochimica Acta*, 254, 156–172.

Tuttle, O. F., & Bowen, N. L. (1958). *Origin of granite in the light of experimental studies in the system NaAlSi₃O₈–KAlSi₃O₈–SiO₂–H₂O* (Vol. 74). Geological Society of America.

Venugopal, S., Schiavi, F., Mouna, S., Bolfan-Casanova, N., Druitt, T., & Williams-Jones, G. (2020). Melt inclusion vapour bubbles: The hidden reservoir for major and volatile elements. *Scientific Reports*, 10(1), 1–14.

Wallace, P. J., Anderson, A. T., & Davis, A. M. (1995). Quantification of pre-eruptive exsolved gas contents in silicic magmas. *Nature*, 377(6550), 612–616.

Waters, L. E., & Lange, R. A. (2013). Crystal-poor, multiply saturated rhyolites (obsidians) from the cascade and Mexican arcs: Evidence of degassing-induced crystallization of phenocrysts. *Contributions to Mineralogy and Petrology*, 166(3), 731–754.

Waters, L. E., & Lange, R. A. (2015). An updated calibration of the plagioclase-liquid hygrometer-thermometer applicable to basalts through rhyolites. *American Mineralogist*, 100(10), 2172–2184.

Wieser, P. E., Edmonds, M., Gansecki, C., MacLennan, J., Jenner, F., Antoshechkina, P., et al., & EIMF. (2022). Explosive activity on Kīlauea's Lower East Rift Zone fuelled by a volatile-rich, dacitic melt. *Geophysics, Geochemistry, Geophysics*. <https://doi.org/10.1029/2021GC001046>

Wieser, P. E., Lamadrid, H., MacLennan, J., Edmonds, M., Matthews, S., & Iacovino, K. (2021). Reconstructing magma storage depths for the 2018 kilaeuan eruption from melt inclusion CO₂ contents: The importance of vapor bubbles. *Geochemistry, Geophysics, Geosystems*, 22(2), e2020GC009364.